Nuclear Medicine Review 2021, Vol. 24, No. 1, pages 1–40

Nuclear Medicine
REVIEW

merged with Problems of Nuclear Medicine

MNiSW: 40 pkt.

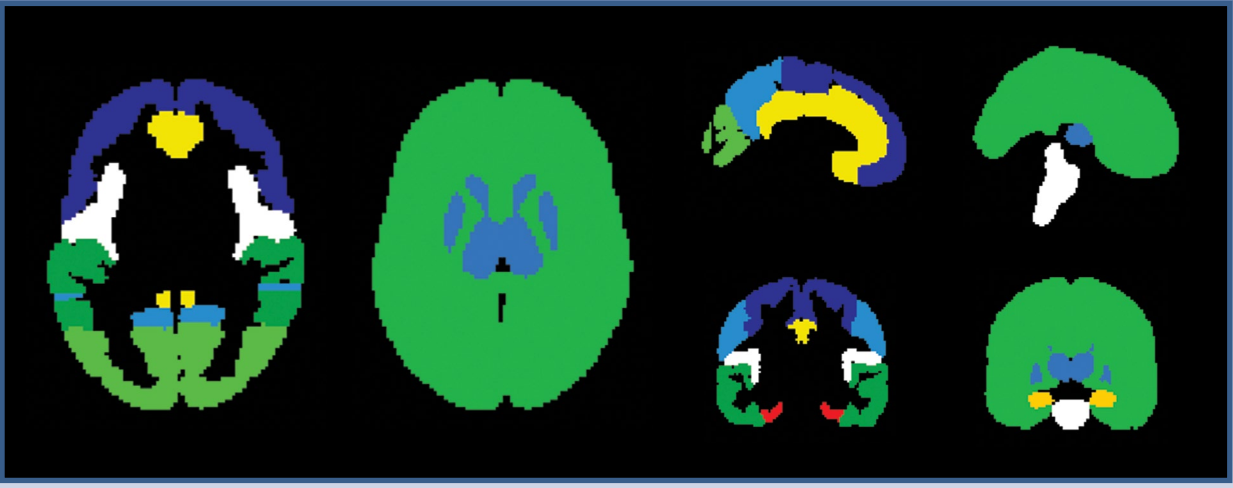

See page 13

ISSN 1506–9680

2021, Volume 24, Number 1

Journal of Polish, Serbian, Hungarian, Bulgarian
and Macedonian Societies of Nuclear Medicine

Bulgarian Nuclear Society

VIA MEDICA

www.journals.viamedica.pl/nuclear_medicine_review

Nuclear Medicine
REVIEW

merged with ***Problems of Nuclear Medicine****

Editor-in-Chief

G. Kamiński (Warszawa, Poland)

Deputy Editor-in-Chief

M. Dziuk (Warszawa, Poland)
J. Kunikowska (Warszawa, Poland)

National Editors

I. Garai (Debrecen, Hungary)
D. Huić (Zagreb, Croatia)
D. Sobic Saranovic (Belgrade, Serbia)

Board of Editors:

V. Artiko (Belgrade, Serbia)
R.P. Baum (Bad Berka, Germany)
O. Belohlavek (Prague, Czech Republic)
B. Birkenfeld (Szczecin, Poland)
K. Borbély (Budapest, Hungary)
J. Braziewicz (Kielce, Poland)
J. Buscombe (London, United Kingdom)
J.M. Carrill (Santander, Spain)
I. Carrio (Barcelona, Spain)
A. Celler (Vancouver, Canada)
A. Chiti (Rozzano, Italy)
B. Chrapko (Lublin, Poland)
A. Cuocolo (Naples, Italy)
C.S. Cutler (Columbia, United States)
G. De Vincentis (Rome, Italy)
E. Dziuk (Warszawa, Poland)
R. Howman-Giles (Sydney, Australia)
A. Hubalewska-Dydejczyk (Kraków, Poland)
B. Jarząb (Gliwice, Poland)
W. Kloc (Gdańsk, Poland)
W. Knapp (Hannover, Germany)
V.N. Korsunsky (Moscow, Russia)
M. Kostkiewicz (Kraków, Poland)
I. Kozłowicz-Gudzińska (Warszawa, Poland)
O. Kraft (Ostrava, Czech Republic)
L. Królicki (Warszawa, Poland)
J. Kuśmierek (Łódź, Poland)
J. Lepej (Banska Bystrica, Slovak Republic)
A. Lewiński (Łódź, Poland)
T. Maina (Athens, Greece)
B. Małkowski (Bydgoszcz, Poland)
R. Mikołajczak (Otwock–Świerk, Poland)
M. Myslivecek (Olomuc, Czech Republic)
V. Obradović (Belgrade, Serbia)
A.K. Padhy (Singapore)
E. Piperkova (Sofia, Bulgaria)
A. Płachcińska (Łódź, Poland)
Z. Rajkovaca (Banja Luka, Bosnia & Herzegovina)
F. Rogowski (Białystok, Poland)
D. Rubello (Rovigo, Italy)
M. Ruchała (Poznań, Poland)
M.M. Saw (Singapore)
A. Signore (Rome, Italy)
H. Sinzinger (Vienna, Austria)
A. Soricelli (Italy)
A. Sowa-Staszczak (Kraków, Poland)
D.A. Stanescu (Bucharest, Romania)
M. Studniarek (Gdańsk, Poland)
A. Syrenicz (Szczecin, Poland)
I. Szilvasi (Budapest, Hungary)
K. Toth (Warszawa, Poland)
J.H. Turner (Fremantle, Australia)
I. Velikyan (Uppsala, Sweden)
M. Vlajkovic (Nis, Serbia)
P. Vlcek (Praha, Czech Republic)

The Scientific Committee of the journal is being created and the list of the scientific council members contains the persons who have declared willingness to collaborate.

Secretary

A. Krajewska (Warszawa, Poland)

Editorial Office

Wojskowy Instytut Medyczny
ul. Szaserów 128, 04–141 Warszawa
e-mail: nmr@viamedica.pl

Managing Editor

K. Klimek (Gdańsk, Poland)

*Following the agreement concluded on 23 February 2011 between the Polish Society of Nuclear Medicine and Via Medica Sp. z o.o. the journal „Nuclear Medicine Review" has merged with „Problemy Medycyny Nuklearnej", a journal published since 1987.

Nuclear Medicine Review (ISSN 1506–9680) is published twice a year by VM Media sp. z o.o., VM Group sp. k., Grupa Via Medica
ul. Świętokrzyska 73, 80–180 Gdańsk, Poland
tel: (+48 58) 320 94 94, fax: (+48 58) 320 94 60; e-mail: redakcja@viamedica.pl, marketing@viamedica.pl
http://www.viamedica.pl

Advertising. For details on media opportunities within this journal please contact the advertising sales department, ul. Świętokrzyska 73, 80–180 Gdańsk, Poland
tel: (+48 58) 320 94 52, e-mail: marketing@viamedica.pl

The Editors accept no responsibility for the advertisement contents.

Single issues/advertising inquires should be addressed to VM Media sp. z o.o., VM Group sp. k., Grupa Via Medica, bank account:
Fortis Bank Polska SA o/Gdańsk 24 1600 1303 0004 1007 1035 9150 — PLN payment;
Fortis Bank Polska SA o/Gdańsk PL 15 1600 1303 0004 1007 1035 9021; SWIFT: PPABPLPK — EUR payment.

Single issues requests should be send to e-mail: prenumerata@viamedica.pl. Electronic orders option available at: www.nmr.viamedica.pl

20-0825.001.001

VIA MEDICA © Via Medica 2021

All rights reserved, including translation into foreign languages. No part of this periodical, either text or illustration, may be used in any form whatsoever. It is particularly forbidden for any part of this material to be copied or translated into a mechanical or electronic language and also to be recorded in whatever form, stored in any kind of retrieval system or transmitted, whether in an electronic or mechanical form or with the aid of photocopying, microfilm, recording, scanning or in any other form, without the prior written permission of the publisher. The rights of the publisher are protected by national copyright laws and by international conventions, and their violation will be punishable by penal sanctions.

Indexation: Crossref, DOAJ (Directory of Open Access Journals), EMBASE, ESCI (Emerging Sources Citation Index), Index Copernicus (100.00), MEDLINE, Polish Medical Bibliography, Ministry of Science and Higher Education (40), Scopus, Ulrich's Periodicals Directory.

Editorial policies and author guidelines are published on journal website: www.journals.viamedica.pl/nuclear_medicine_review

Nuclear Medicine
R · E · V · I · E · W

merged with ***Problems of Nuclear Medicine****

2021, Volume 24, Number 1

VIA MEDICA

Nuclear Medicine Review 2021, 24, 1: V
DOI: 10.5603/NMR.2021.0010

ISSN 1506–9680

Dear Sirs and Madams,

it's winter time 2021. One of the worst crises in the World seems it doesn't end: COVID-19 pandemia developing in the world, Capitol assault in the United States Brexit in Europe a few days ago. Heavy times… But there is the light seen in the end of the tunnel. The vaccination against COVID-19 has already started, democracy and peace won in U.S., what about U.K.? We will see. Good luck! Nevertheless, I am happy introducing the first issue of "Nuclear Medicine Review" in 2021. The Japanese authors open the chapter "Original articles" with paper Effect of position and volume of space-occupying liver lesions on liver function index in 99mTc-GSA scintigraphy. They conclude that, a three-dimensional quantitative index is a more accurate quantitative indicator of hepatic reserve than the dynamic planar image and is expected to facilitate future clinical research.

The second article by Hungarian investigators concluding that: Age and Body Mass Index proved to be general, and diabetes regional predictor of brain hypoperfusion. BMI appeared to be a novel factor affecting brain perfusion. In addition they found difference between the obese and the diabetic group in the insula.

The Review part consists of the general state of knowledge concerning Breast Cancer and PET Imaging by scientist Ismet Sarikaya from Kuwait.

In chapter Clinical vigniette there are discussed four interesting clinical cases from Kolumbia, Iran, India, Bosnia and Herzegovina and Poland.

At the end of my letter some feelings from the bottom of my heart. Polish poet and priest Jan Twardowski [1915–2006] said: let's hurry to love people, they leave so early… In memoriam on incredible Professor Anna Celler by her friends Prof. Bożena Birkenfeld and Prof. Renata Mikołajczak ends this issue.

Yours,
Grzegorz Kamiński
G. Kamiński
Editor-in-Chief
Nuclear Medicine Review

VIA MEDICA

Nuclear Medicine Review 2021, 24, 1: 1–10
DOI: 10.5603/NMR.2021.0001

ISSN 1506–9680

Original

Effect of position and volume of space-occupying liver lesions on liver function index in ^{99m}Tc-GSA scintigraphy

Ryotaro Tokorodani[1], Hiromitsu Daisaki[2], Yukinori Okada[3], Eisuke Yasuda[4]
[1]Department of Radiology, Kochi Medical School Hospital, Kochi, Japan
[2]Departments of Gunma Prefectural College of Health Sciences, Maebashi, Japan
[3]Departments of Radiological Technology, Graduate School of Health Science, Suzuka University of Medical Science, Suzuka, Japan
[4]Departments of Radiology, St. Marianna University School of Medicine, Kawasaki, Japan

[Received 29 VI 2020; Accepted 13 X 2020]

Abstract

Background: The authors aimed to elucidate the effect of liver space-occupying lesions (SOL) on the quantitative index of the hepatic reserve, calculated using the dynamic planar image (LHLplanar), and a three-dimensional quantitative index (LHLSPECT) calculated using quantitative combined modality single-photon emission computed tomography (SPECT/CT).

Material and methods: Water balloons of different volumes that simulated liver SOL were placed in various positions in the combined cardiac-liver phantom to examine the effects of liver SOL on visualization and quantitative indicators (LHLplanar and LHLSPECT). A 200 mL water balloon was placed in the anterior right, posterior right, left medial and left lateral lobes in the liver phantom to compare LHLplanar and LHLSPECT values with and without liver SOL at each position. Subsequently, volumes of those in the front of the right lobe were changed to 50 mL, 100 mL, 200 mL, and 400 mL, followed by statistically comparing LHLplanar and LHLSPECT values in the presence and absence of liver SOL.

Results: Despite the variation in the degree of defect accumulation with the location of the balloon when using frontal planar imaging, quantitative SPECT/CT imaging identified all defects. Multiple comparison analysis revealed that unlike LHLSPECT, the LHLplanar values changed according to liver SOL position and volume.

Conclusions: Liver SOL position and volume may affect the hepatic reserve assessments performed using LHLplanar values. In contrast, LHLSPECT is calculated using quantitative SPECT/CT and considers the effects of scattering and attenuation corrections. Therefore, LHLSPECT is a more accurate quantitative indicator of hepatic reserve than LHLplanar and is expected to facilitate future clinical research.

KEY words: galactosyl human serum albumin; LHL15; SPECT-CT; Liver SOL

Nucl Med Rev 2021; 24, 1: 1–10

Introduction

It is imperative to preserve liver function during hepatectomies, the indication of which is determined via the preoperative assessment of hepatic reserve [1–3]. ^{99m}Tc-galactosyl human serum albumin (^{99m}Tc-GSA) specifically accumulates in the asialoglycoprotein receptor and is typically used to evaluate hepatic functional reserve [4–7]. Several analytical methods have currently been reported to evaluate hepatic functional reserve using preoperative ^{99m}Tc-GSA receptor scintigraphy [8–11]. However, two of the most commonly used indices that are easy to calculate and less device-dependent are LHL15 and HH15. The former can be calculated as a count ratio [L15/(H15+L15)] of the liver activity (L) to the heart activity [H] + liver activity [L] at 15 minutes after injection, while the latter can be calculated as a count ratio (H15/H3) of the heart activity (H) at 15 minutes (H15) to that at 3 minutes (H3) after injection. Typically, these indices are calculated using only the frontal planar images, which are acquired by using a gamma camera. However, the application of attenuation and scatter correction is difficult, considering the lack of depth or anatomical information in a frontal planar image. Also, a dynamic planar image cannot get enough counts due to time constraints. Therefore, scatter correction is not generally used in the dynamic planar image because it can cause increased statistical errors due to decreased counts. Additionally, it may demonstrate poorer accuracy in assessing liver functional reserve, because counts emitted from the liver are attenuated or scattered by the liver space-occupying lesions (SOLs). Moreover,

Correspondence to: Ryotaro Tokorodani
Department of Radiology,
Kochi Medical School Hospital, Kochi, Japan
185-1 Kohasu, Oko-cho, Nankoku-shi,Kochi, Japan
phone: +81-88-866-5811; fax: 088-886-2260
e-mail: jm-ryotaro_tokorodani@kochi-u.ac.jp

the degree of the effect of attenuation depends on the location of the liver SOL [12, 13].

It has been reported that the diagnostic ability to occupy lesions can be improved by using SPECT [14, 15]. Furthermore, recent studies have reported that attenuation and scatter can be accurately corrected by using a correction algorithm for single-photon emission computed tomography in combination with computed tomography (SPECT/CT) [16–18]. In addition, Hasegawa et al. [19] reported a method to calculate an accurate index (LHL_{SPECT}) of liver function reserve, which includes information about the reserve by using an attenuation and scatter corrected SPECT image for ^{99m}Tc-GSA receptor scintigraphy. However, there have been no reports on the clinical accuracy concerning the influence of liver SOL on the liver function reserve evaluation via LHL15.

We aimed to elucidate the effect of liver SOLs on the LHL15-based index of the liver functional reserve and to evaluate and compare the usefulness of SPECT-CT imaging with planar imaging.

Material and methods

Equipment and acquisition conditions

The unique phantom configuration, which included the heart and the liver, was devised to simulate a human model of ^{99m}Tc-GSA distribution. First, the phantom heart was constructed by combining the cardiac phantom (model: RH-2, Kyoto Science Co., Ltd, Kyoto, Japan) and the outer cylinder of the National Electrical Manufacturers Association (NEMA) body phantom (Data Spectrum Co., Ltd. North Carolina, USA). Fixing components made with a three-dimensional (3D) printer were used to fix the phantom heart to the outer cylinder of the NEMA body phantom. Therefore, the position of the heart did not change across multiple acquisitions. Furthermore, two bubble wraps that simulated the lung field approximately -980 Hounsfield Unit were inserted and fixed on both sides of the phantom heart within the NEMA body phantom. A plastic tube of diameter 3 cm injected with dipotassium hydrogen phosphate was used to simulate the spine and was subsequently fixed with an adhesive tape [20]. Finally, the inside of the outer cylinder was filled with water. Figure 1 shows the components of the cardiac phantom and the appearance after assembly.

The outer cylinder of Flanged Jaszczak ECT Phantom ((Data Spectrum Co., Ltd. North Carolina, USA) was used for the trunk of the phantom liver. The liver portion of the liver/renal phantom (model: LKS, Kyoto Science Co., Ltd.) was fixed to the outer cylinder using a fixing component made with a 3D printer. Similar to the phantom heart, a plastic tube of 3 cm diameter injected with dipotassium hydrogen phosphate was placed on the dorsal side of the trunk and

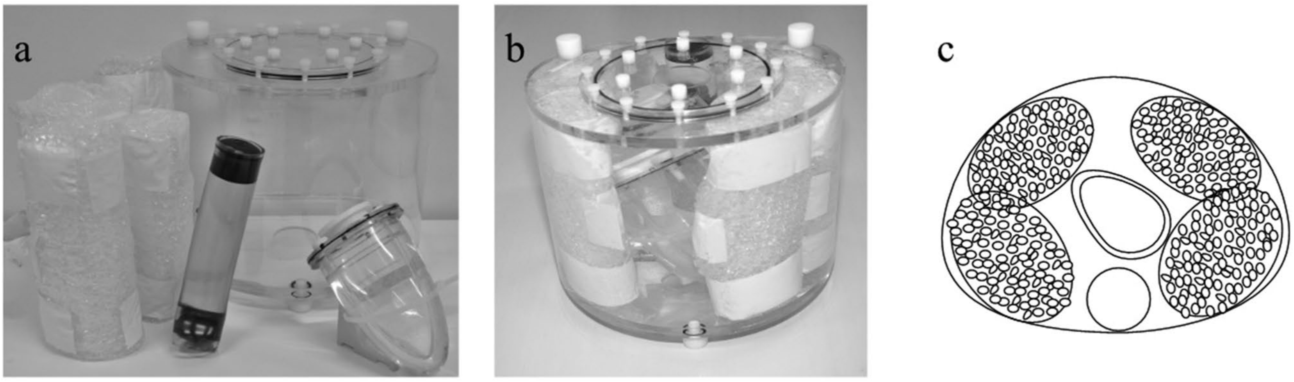

Figure 1. Appearance of cardiac phantom before (a) and after (b) assembly (c) schemas layout

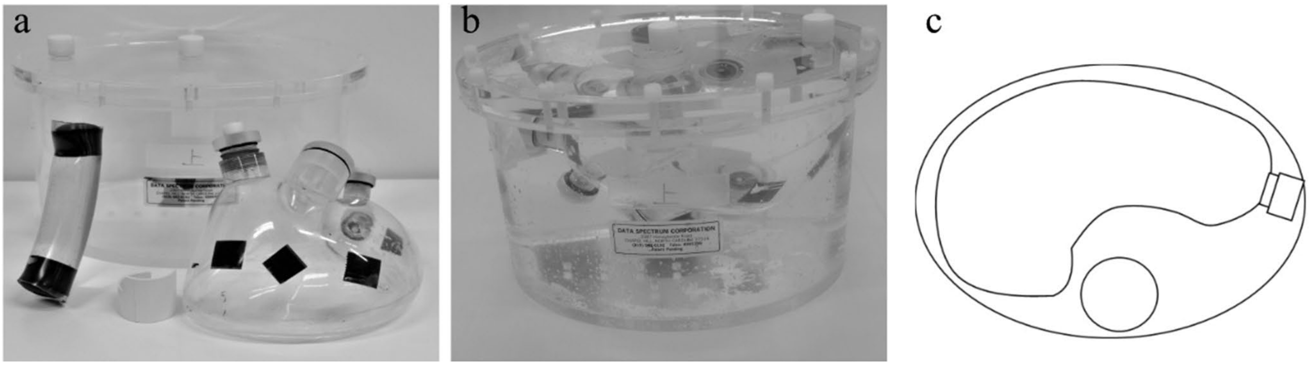

Figure 2. Appearance of liver phantom before (a) and after (b) assembly (c) schemas layout

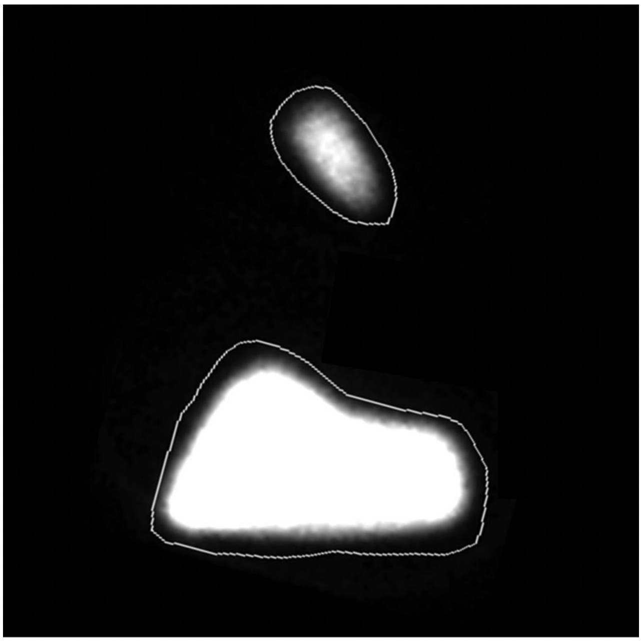

Figure 3. Regions of interest (ROI) setting in liver phantom

fixed with an adhesive tape. Figure 2 shows the components of the phantom liver and the appearance after assembly.

A ^{99m}Tc solution of 100 kBq/mL corresponding to the clinical liver radioactivity concentration was filled in the liver phantom (1600 mL) based on the study by Toritsuka et al. [21] as the reference for All data acquisition. Since the normal value of LHL15 is approximately 0.900, the cardiac phantom (133 mL) was filled with 16.0 MBq of ^{99m}Tc solution, and the theoretical value of LHL15 was adjusted to 0.909.

All data acquisition was performed using a SPECT/CT scanner named Symbia T6 (Siemens Healthcare Co., Ltd, Munich, Germany) equipped with a low-energy high-resolution collimator Hole length 24.1 mm, Septal thickness 0.16 mm, Hole diameter across the flats 1.11 mm. Data acquisition in planar imaging was performed using parameters of matrix size 128 × 128, zoom 1.0, and pixel size 4.8 mm. Dynamic planar imaging was performed for 18 minutes at 10 seconds/frame × 108 frames under conditions identical to the authors' clinical protocol. Following this, SPECT imaging was performed at 128 × 128 matrix, zoom 1.0, pixel size 4.8 mm, 360-degree acquisition (60 directions, 6-degree steps), and 12 seconds/step. Even though scatter correction was not performed in the dynamic planar imaging, the triple energy window (TEW) method was used for the same in SPECT imaging. In this method, the main window was set at 140 keV ± 10%, along with a 7% energy width of two sub-windows located on both sides of the main window. CT-based attenuation correction method was used for attenuation correction. Furthermore, CT scanning was performed at 130 kV for the tube voltage, Quality Reference was set at 120 mA with auto exposure control for the tube current, 1.0 s/rot for the scan time, and 4 mm for the image slice thickness. Image reconstruction and count analysis were performed using the Syngo MI Apps version VA60C (Siemens Healthcare Co., Ltd, Munich, Germany). The SPECT images were reconstructed using a 3D ordered subset expectation-maximization algorithm with collimator aperture correction called Flash-3D. The SPECT image reconstruction parameters of Flash-3D were set to 10 subsets and 6 iterations, and then image filtering for noise reduction was performed using a 3D Gaussian post-filtering function with 9.6 mm full width at half maximum.

Calculation of LHL_{planar} and LHL_{SPECT}

LHL_{planar} was calculated using regional counts of planar imaging of the heart (H_{planar}) and liver (L_{planar}) at 15 minutes, as follows:

$$LHL_{Planar} = L_{Planar}/(L_{Planar}+H_{Planar}) \tag{1}$$

Here, L_{planar} and H_{planar} were obtained by regions of interest (ROI) that were manually drawn on both the liver and the heart, respectively, on the two-dimensional planar image. All measurements were performed by three radiological technologists). Figure 3 shows an example of the ROI placed on the planar image.

LHL_{SPECT} was calculated using regional counts of SPECT-CT imaging of the heart (H_{SPECT}) and liver (L_{SPECT}) as follows:

$$LHL_{SPECT} = L_{SPECT}/(L_{SPECT}+H_{SPECT}) \tag{2}$$

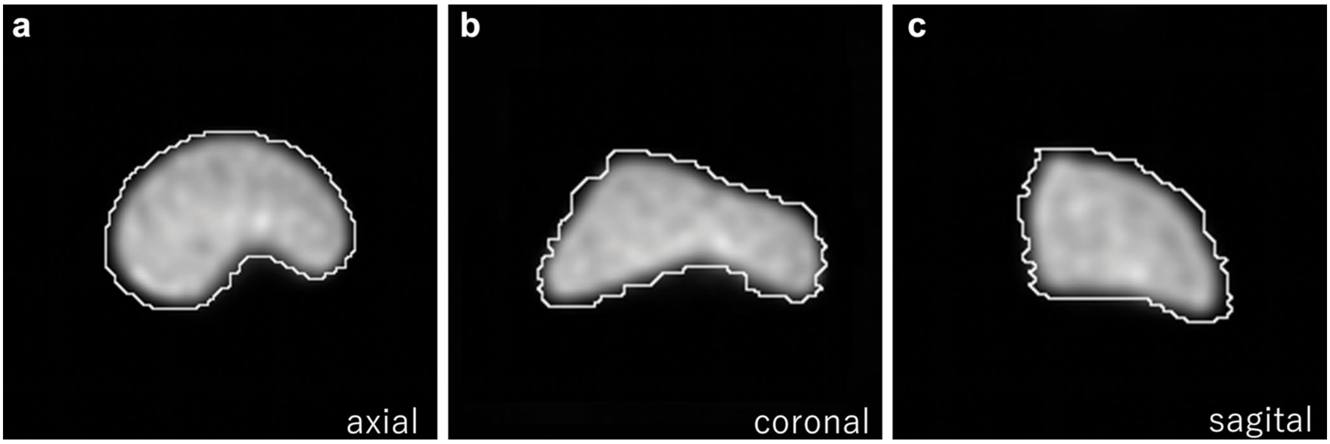

Figure 4. Volume of interest (VOI) setting at the center slice of the liver phantom

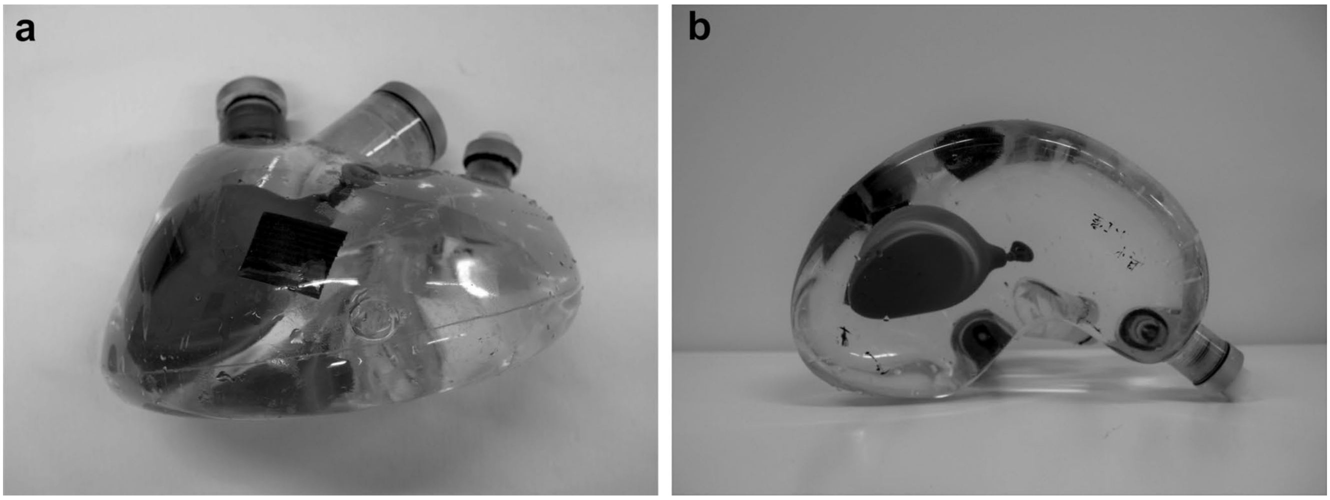

Figure 5. Liver phantom with water balloons

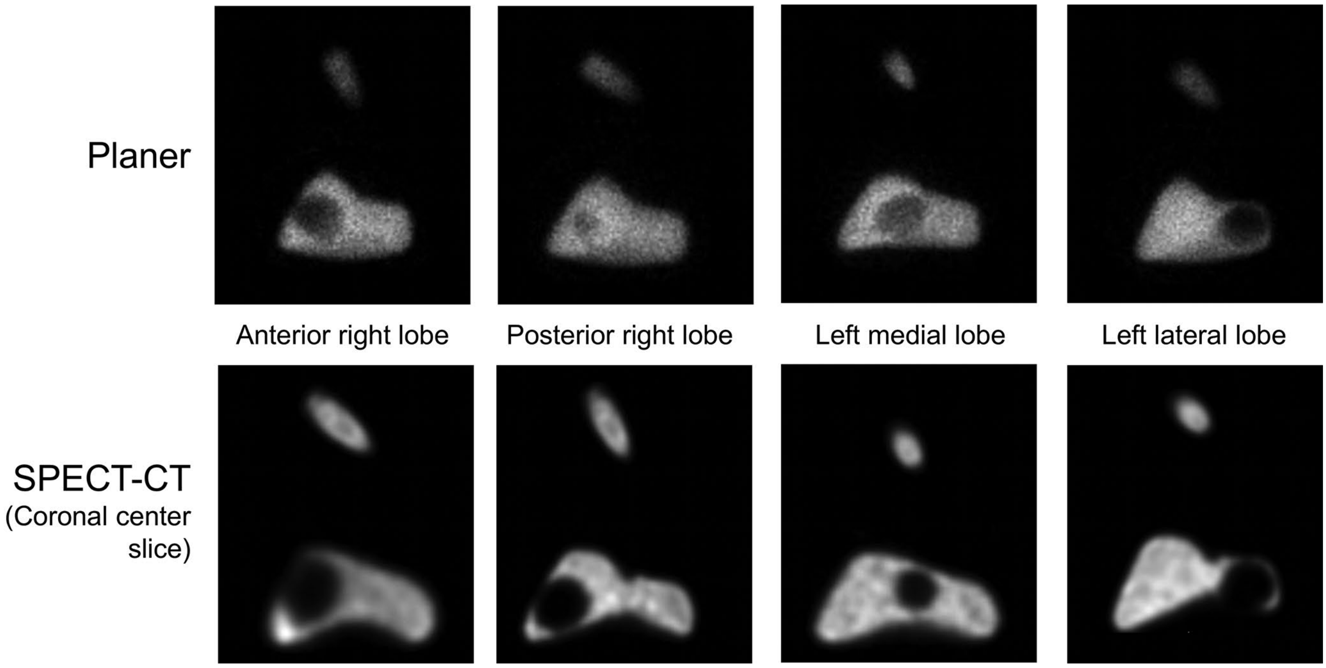

Figure 6. planar imaging (a) and SPECT-CT imaging (b) obtained using phantoms with liver space-occupying lesion (SOL) placed at different positions

Here, L_{SPECT} and H_{SPECT} are obtained by volume of interest (VOI) that was manually drawn on both the liver and the heart, respectively, on the SPECT-CT image. Both LHL_{planar} and LHL_{SPECT} were measured 10 times by three radiological technologists, following which each median value was calculated. Figure. 4 shows an example of the VOI placed on the SPECT-CT image.

Evaluation of position dependency

A balloon containing 200 mL of water simulating liver SOL was placed at different positions in the anterior right, posterior right, left medial and left lateral lobes in the liver phantom to change the distribution of radioactivity within the liver. When the water balloon was inserted, a certain amount of water was withdrawn from the liver phantom and the theoretical value of LHL15 was always adjusted to 0.909 by injecting 160 MBq of ^{99m}Tc solution. The water balloon was secured to the liver phantom using a hook and loop fastener to ensure repeatability. Figure 5 shows the appearance of a liver phantom with a secured water balloon.

After changing the position of the water balloon, both frontal planar and SPECT-CT imaging were performed, and LHL15 calculated using each imaging method was compared. Bland-Altman plots were constructed to assess measurement agreement between equivalent measurements [22]. When the confidence interval does not include 0, it is determined that there is a fixed error if the

Table 1. LHL_{planar} and LHL_{SPECT} calculated by phantom with space occupying lesions of liver located in different positions

Water balloon position	None	Posterior right lobe	Anerior right lobe	Left medial lobe	Left lateral lobe
LHL_{planar}	0.911	0.909	0.902	0.907	0.909
Heart counts	822233	814951	811176	813525	81286
Liver counts	8411452	8150716	7428690	7918294	8151403
LHL_{SPECT}	0.912	0.911	0.911	0.911	0.911
Heart counts	1311653	1304817	1299157	1288636	1335552
Liver counts	13567975	13401944	13231695	13292786	13668551

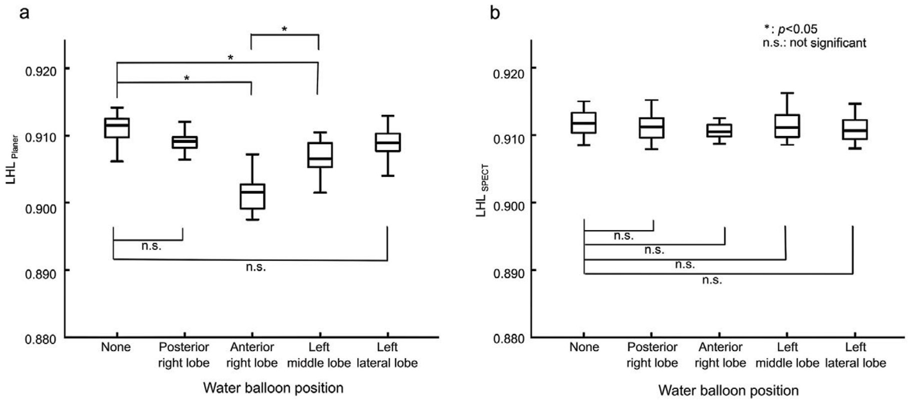

Figure 7. Effect of liver space-occupying lesion (SOL) position on LHL_{planar} (a) and LHL_{SPECT} (b)

measured value exists in either the positive direction or the negative direction. The software used to create the Bland-Altman plot was Microsoft Excel version 2016 (Microsoft Corporation Co., Ltd, Redmond, State of Washington).

Evaluation of volume dependency

The water balloon was fixed at the front of the right lobe and its volume was changed to 50, 100, 200 and 400 mL. Planar imaging and SPECT-CT imaging were performed for each volume. Bland-Altman plots were constructed to assess measurement agreement between equivalent measurements.

Statistical Analysis

LHL_{planar} and LHL_{SPECT} values with the water balloon placed at each position in the liver phantom were independently compared with those without SOLs as the standard reference. The Kruskal-Wallis test was used for the comparison, and the Mann-Whitney U test was performed for the multiple comparison test, which was corrected using the Bonferroni method. The significance level was set at $p < 0.05$. Statistical analysis software used was EZR version 1.37 (Jichi Medical School Saitama Medical Center, Saitama, Japan) [23].

Results

Position dependency evaluation

Figure.6 shows the images obtained with each imaging technique, changing the position of the water balloon.

Changes in the degree of defect accumulation associated with the location of the balloon are depicted via frontal planar imaging (Fig. 6a). A visual assessment revealed that defects were clearly visible when the water balloons were placed in the right upper, left medial, and left lateral lobes, even though the defect was only identified as a low accumulation region in cases where the water balloon was placed in the posterior right lobe. However, since both attenuation and scatter correction were applied to SPECT-CT imaging, it was able to clearly identify all defects regardless of the position of the water balloon.

Table 1 shows the average of total ROI counts of the heart and the liver, LHL_{planar}, and LHL_{SPECT} for each water balloon position.

The position dependency effect of each LHL15 is shown by a box and whisker plot in Figure 7.

The median LHL_{planar} values calculated by planar imaging were: 0.911, 0.909, 0.902, 0.906, and 0.909 in the absence of a water balloon, water balloon at the anterior right lobe, posterior right lobe, left medial lobe, and left lateral lobe, respectively. The Kruskal-Wallis test demonstrated a significant difference ($p < 0.001$), and LHL_{planar} showed a significant difference in the anterior right lobe ($p < 0.001$) and the left medial lobe ($p = 0.012$) compared to without water balloon. Additionally, the anterior right lobe showed a significant difference compared to the left medial lobe ($p < 0.001$). However, no significant difference in the posterior right lobe ($p = 0.262$) and the left lateral lobe ($p = 0.618$) was observed.

The median values of LHL_{SPECT} calculated by SPECT/CT imaging were: 0.912, 0.911,0.910, 0.911, and 0.911 in the absence of a water balloon, water balloon at the anterior right lobe, the posterior right lobe, the left medial lobe, and the left lateral lobe, respectively. There was no significant difference according to the Kruskal-Wallis test ($p = 0.266$).

Table 2. LHL_{planar} and LHL_{SPECT} calculated by phantom with different volume of space occupying lesions of liver

Water balloon volume	None	50 mL	100 mL	200 mL	400 mL
LHL_{planar}	0.911	0.912	0.910	0.901	0.891
Heart counts	822233	819828	834696	810514	819583
Liver counts	8411452	8511024	8462878	7411870	6725406
LHL_{SPECT}	0.912	0.911	0.910	0.911	0.911
Heart counts	1311653	1361975	1389435	1340746	1342052
Liver counts	13567975	13950857	14072066	13658601	13670859

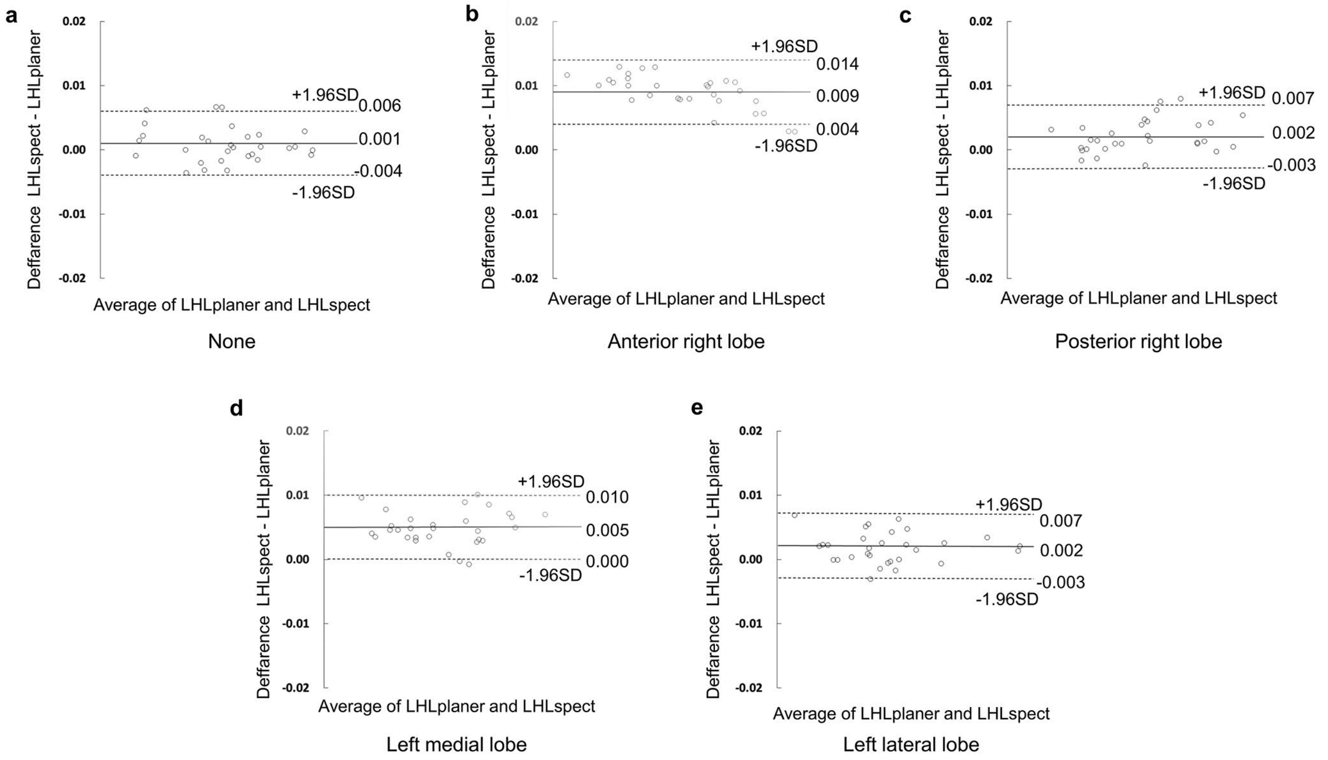

None

Anterior right lobe

Posterior right lobe

Left medial lobe

Left lateral lobe

Figure 8. Bland-Altman plots for regions of interest (ROI) comparisons from LHL_{planar} and LHL_{SPECT} for each water balloon position

Figure 8 shows Bland–Altman plots for ROI comparisons from LHL_{planar} and LHL_{SPECT} for each water balloon position.

According to Bland-Altman analysis, there was a fixed bias in the anterior right lobe and left medial lobe.

Volume dependency evaluation

Figure 9 shows the images obtained by each imaging method with different water balloon volumes.

In the planar phantom images, the degree of defect changed according to the changes in the water balloon volumes, whereas the degree of the defect was equivalent in the SPECT/CT phantom images, and the area was accurately depicted. Furthermore, SPECT/CT imaging was able to depict the liver uniformly.

Table 2 shows the average of total ROI counts of the heart and liver, LHL_{planar}, and LHL_{SPECT} for each water balloon volume.

The volume dependency effect of each LHL15 is shown by a box and whisker plot in Figure 10.

Median LHL plane values calculated by frontal planar imaging were 0.911 in the absence of a water balloon and 0.912, 0.910, 0.901 and 0.892 for 50, 100, 200 and 400 mL water balloons, respectively. The Kruskal-Wallis test showed a significant difference ($p < 0.001$), and LHL_{planar} showed a significant difference in 200 mL ($p < 0.001$) and 400 mL ($p < 0.001$) water balloons compared with the one without the water balloon. However, no significant difference was found with the 50 mL ($p = 1.000$) and 100 mL ($p = 1.000$) water balloons.

In contrast, median LHL_{SPECT} values obtained with SPECT-CT imaging were 0.912 without the water balloon and 0.911, 0.910, 0.911 and 0.910 for the 50, 100, 200 and 400 mL water balloons, respectively. The Kruskal-Wallis test showed no significant difference ($p = 0.157$).

Figure 11 shows Bland–Altman plots for ROI comparisons from LHL_{planar} and LHL_{SPECT} for different water balloon volumes.

According to Bland-Altman analysis, there was a fixed bias in the 200 mL and 400 mL water balloons.

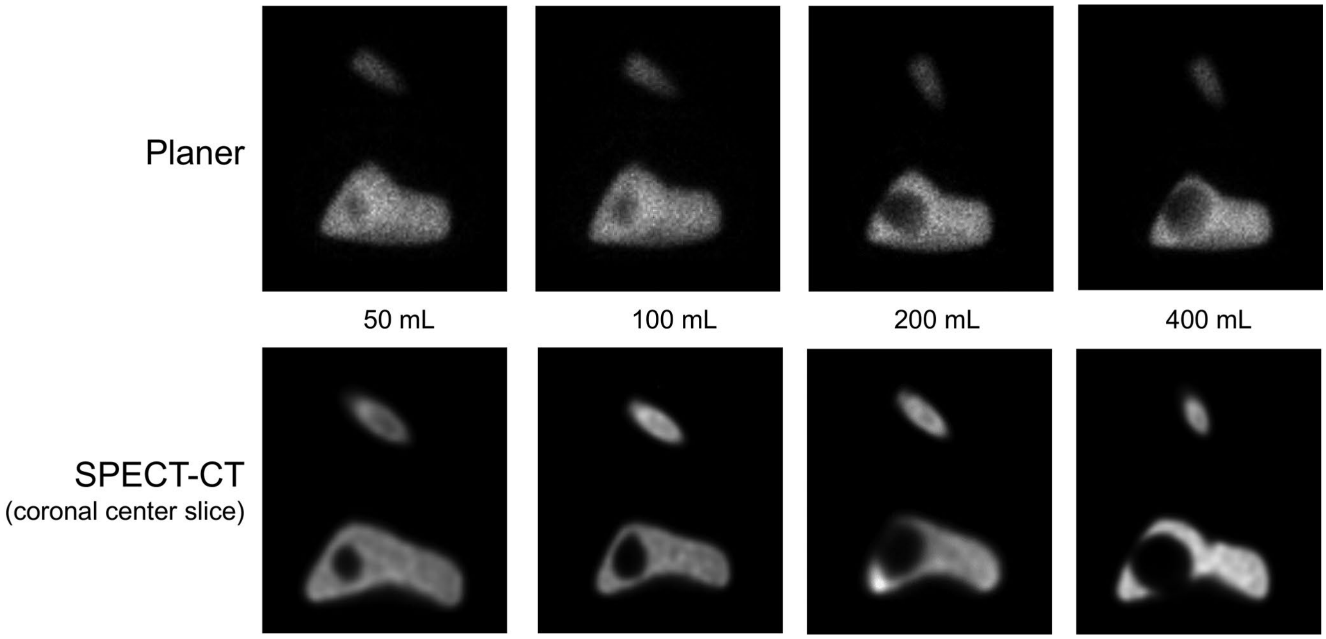

Figure 9. planar imaging (a) and SPECT-CT imaging (b) obtained using phantoms with liver space-occupying lesion (SOL) with different volumes

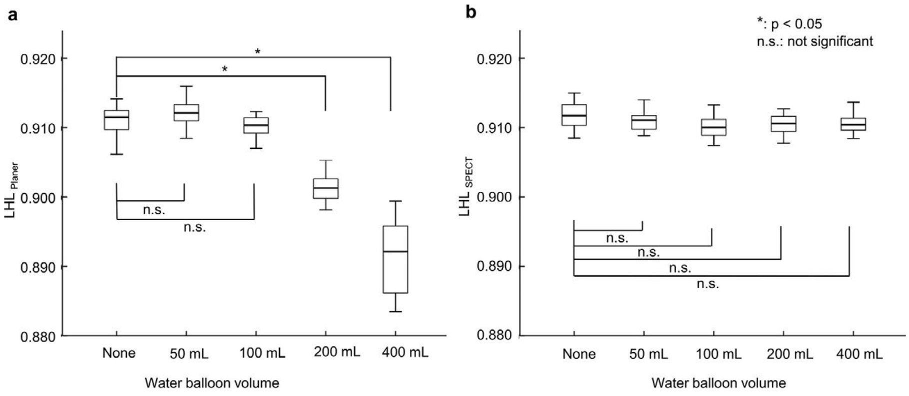

Figure 10. Effect of liver space-occupying lesion (SOL) volume on LHL_{planar} (a) and LHL_{SPECT} (b)

Discussion

^{99m}Tc-GSA specifically accumulates in asialoglycoprotein receptors on the surface of hepatocytes, and the accumulation reflects liver function. It is also known that ^{99m}Tc-GSA does not accumulate in tumours without the asialoglycoprotein receptor or in highly fibrotic hepatocytes. The hepatic clearance of ^{99m}Tc-GSA receptor scintigraphy performed preoperatively has been reported as a useful index to predict postoperative liver function [7]. Several centres currently evaluate hepatic reserve by LHL_{planar} imaging. However, hepatic reserve assessment using the frontal planar image cannot take depth or anatomical information into account. Furthermore, the position and volume of the liver SOL influence the result of the assessment. In this study, the authors evaluated the effect of the position and volume of liver SOL on LHL_{planar} and examined how these effects were improved by SPECT-CT imaging with various corrections.

In the position dependency evaluation using the frontal planar image, the water balloon was visualized as a defect when it was present in the right anterior lobe in the liver phantom. However, the visibility of the defect changed with a change in the position of the water balloon. This suggests that it is not possible to detect the counts from the normal liver present behind the liver SOL (simulated with a water balloon) causing attenuation or scattering at the frontal detector. This is also apparent from the fact that LHL_{planar} showed no significant decrease from the theoretical value of 0.909 when the water balloon was placed in the right anterior and left medial lobe, whereas LHL_{planar} was significantly reduced when the water balloon was placed in the right posterior and left lateral lobes. Furthermore, LHL_{planar} decreased when the balloon was placed in the right anterior rather than left medial lobe, suggesting that a larger normal liver volume in the presence of a liver SOL was associated with a greater possibility of attenuation or scattering. Similarly, in the Bland-Altman

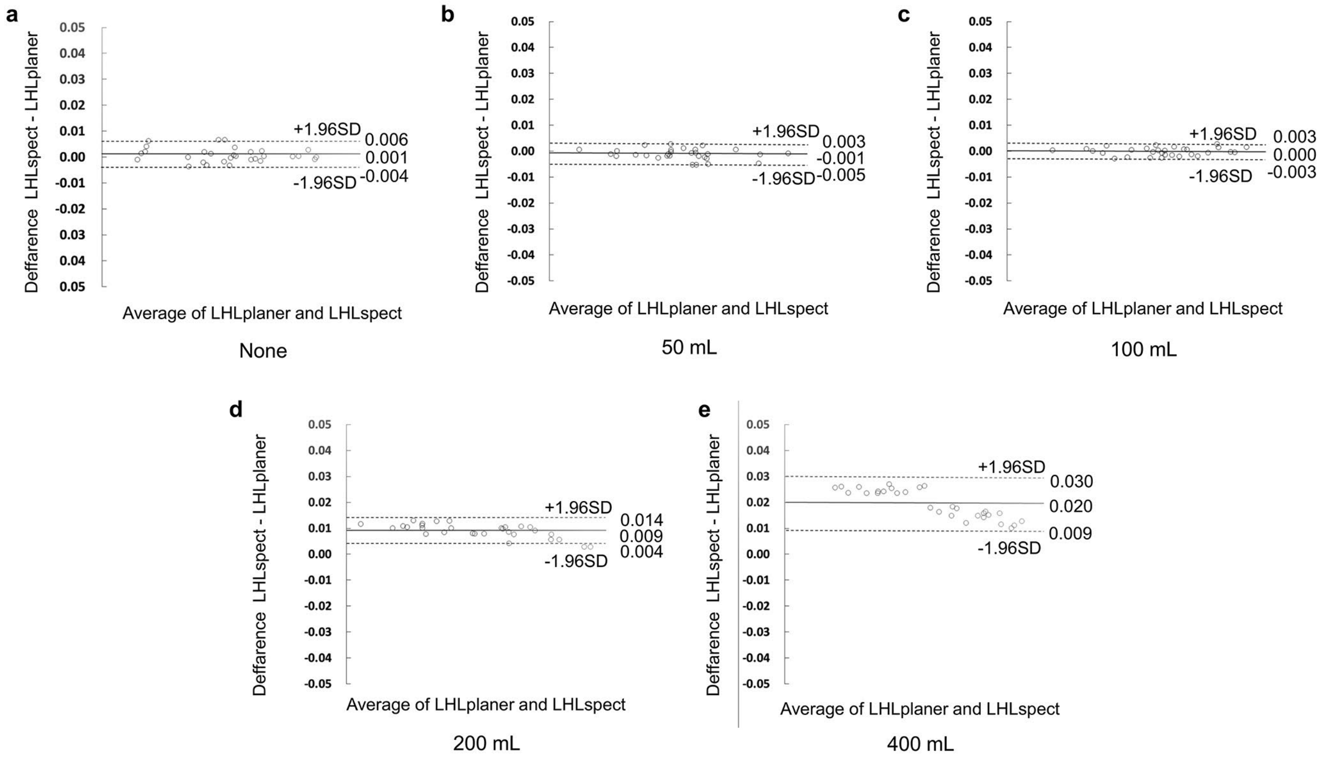

None

50 mL

100 mL

200 mL

400 mL

Figure 11. Bland-Altman plots for regions of interest (ROI) comparisons from LHL_{planar} and LHL_{SPECT} for different water balloon volumes

analysis, was observed a fixed bias only in the right posterior and left lateral lobes.

Alternatively, in the phantom images obtained by SPECT/CT imaging, all of the liver and defect parts were correctly imaged by a certain degree of correction, regardless of the attenuation or scattering associated with the position of the water balloon. Additionally, LHL_{SPECT} demonstrated nearly theoretical values regardless of the attenuation or scattering associated with the position of the water balloon. Furthermore, there was no statistically significant difference among different water balloon positions. This could be attributed to the fact that position dependency was eliminated by imaging from 360 degrees and photon attenuation or scatter caused by the water balloon placed within the liver region was corrected by attenuation correction using CT images and scatter correction. Additionally, since the liver is located to the right of the trunk, the resolution recovery effect may have contributed to the improvement of dependency.

considering the evaluation of volume dependency, the phantom images obtained by frontal planar imaging demonstrated an increase in the defect area with an increase in the water balloon volume. Similarly, Bland-Altman analysis reported the presence of a fixed bias only in 200 mL and 400 mL water balloons. This implied an increase in the uncounted area of normal hepatocytes present behind the liver SOL, suggesting that the attenuation or scattering effect was volume dependent. However, the phantom image obtained through SPECT/CT imaging was able to correctly image both the liver and the defect region as in the position-dependent evaluation regardless of the volume of a water balloon, and LHL_{SPECT} reported nearly the same outcomes as the theoretical value. This result revealed that the effects of attenuation and scattering were accurately corrected by the CT attenuation correction and scatter correction method (TEW method) applied by the SPECT-CT scanner used in this study.

LHL_{planar} with dynamic planar imaging has been widely used to assess hepatic reserve. However, this study suggests that in the case of hepatic reserve evaluation using only planar imaging, the measurement results changed depending on the position and volume of the liver SOL. This may be a technical limitation of accurate clinical evaluation of hepatic reserve using planar imaging. However, LHL_{SPECT} values that were calculated using SPECT/CT imaging in this study were not affected by the position and volume of liver SOL, suggesting that SPECT/CT imaging is preferable to ^{99m}Tc-GSA receptor scintigraphy to assess hepatic reserve. Considering this approach can further improve the clinical significance of SPECT/CT imaging in indexing the liver functional reserve. A statistically significant decrease in LHL15 may affect the indications for surgery in patients with decreased liver function. In the future, high-precision indicators calculated by SPECT/CT should be considered as a method to replace or compensate traditional planar imaging methods with position and volume dependency as elucidated by the presented study. However, dynamic imaging using SPECT/CT was inferior to dynamic imaging via a frontal planar image in time resolution. Furthermore, it is imperative to carefully monitor the patient to ensure safety during the examination because the detector rotates multiple times around the patient when using dynamic SPECT/CT imaging.

This study is only a phantom experiment and does not consider actual pharmacokinetics. The first limitation of this study is the LHLplanar reported in this study may be different from the existing indicators (e.g. LHL15) used in clinical practice. Further studies comparing the two approaches using clinical data would be required. SPECT-CT has reportedly been considered an indicator of regional accumulation in the liver [8, 24–25]. Although these studies used SPECT alone, which may include position and volume dependencies, it is possible to reduce these dependencies by using SPECT-CT imaging similar to this study. The second limitation of this study is the position and size of the water balloon in the right lobe. The phantom volume was not large enough to precisely move the water balloon, contrary to what is observed in actual clinical practice, SOL may exist in the middle of the right lobe. Also, in clinical practice, the effect of SOL size depends on liver activity. The third limitation is the calculation method of LHL15. LHL15 is usually calculated using only the frontal planar images, but additional views from the posterior planar images may improve the position- and volume-dependent dependence and should be considered.

Conclusions

Accuracy of the quantitative indicator was limited because LHL_{planar}, which is an index to evaluate hepatic functional reserve using planar imaging, demonstrated position and volume-based dependencies due to the presence of liver SOL. However, LHL_{SPECT} obtained by SPECT-CT imaging with some corrections did not show the position or volume dependencies by liver SOL, highlighting the high degree of accuracy of LHL_{SPECT} as a quantitative indicator to assess hepatic functional reserve in clinical practice.

Conflict of interest

Author Hiromitsu Daisaki has received research grants from Nihon Medi-Physics Co., Ltd.

Human and animal rights

This article does not contain any studies performed with human participants and animals.

Informed consent

Informed consent for this study was not required because it involved no research involving human participants.

References

1. Farges O, Malassagne B, Flejou JF, et al. Risk of major liver resection in patients with underlying chronic liver disease: a reappraisal. Ann Surg. 1999; 229(2): 210–215, doi: 10.1097/00000658-199902000-00008, indexed in Pubmed: 10024102.
2. Nagasue N, Kohno H, Chang YC, et al. Liver resection for hepatocellular carcinoma. Results of 229 consecutive patients during 11 years. Ann Surg. 1993; 217(4): 375–384, doi: 10.1097/00000658-199304000-00009, indexed in Pubmed: 8385442.
3. Scheele J, Stangl R, Altendorf-Hofmann A, et al. Indicators of prognosis after hepatic resection for colorectal secondaries. Surgery. 1991; 110(1): 13–29, indexed in Pubmed: 1866690.
4. Morell AG, Gregoriadis G, Scheinberg IH, et al. The role of sialic acid in determining the survival of glycoproteins in the circulation. J Biol Chem. 1971; 246(5): 1461–1467, indexed in Pubmed: 5545089.
5. Orita Y, Onodera A, Natsume T. Devised a New Preoperative Simulation Using ^{99m}Tc-GSA SPECT Quantitative Method for Liver Resection. Japanese Journal of Radiological Technology. 2016; 72(1): 50–57, doi: 10.6009/jjrt.2016_jsrt_72.1.50.
6. Okabe H, Beppu T, Hayashi H, et al. Rank classification based on the combination of indocyanine green retention rate at 15 min and (99m) Tc-DTPA-galactosyl human serum albumin scintigraphy predicts the safety of hepatic resection. Nucl Med Commun. 2014; 35(5): 478–483, doi: 10.1097/MNM.0000000000000075, indexed in Pubmed: 24686196.
7. Iimuro Y, Kashiwagi T, Yamanaka J, et al. Preoperative estimation of asialoglycoprotein receptor expression in the remnant liver from CT/99mTc-GSA SPECT fusion images correlates well with postoperative liver function parameters. J Hepatobiliary Pancreat Sci. 2010; 17(5): 673–681, doi: 10.1007/s00534-010-0264-6, indexed in Pubmed: 20703846.
8. Yoshida M, Shiraishi S, Sakaguchi F, et al. A quantitative index measured on 99mTc GSA SPECT/CT 3D fused images to evaluate severe fibrosis in patients with chronic liver disease. Japanese Journal of Radiology. 2012; 30(5): 435–441, doi: 10.1007/s11604-012-0072-9.
9. Shuke N, Okizaki A, Kino S, et al. Functional mapping of regional liver asialoglycoprotein receptor amount from single blood sample and SPECT. J Nucl Med. 2003; 44(3): 475–482, indexed in Pubmed: 12621017.
10. Kaibori M, Ha-Kawa SK, Ishizaki M, et al. HA/GSA-Rmax ratio as a predictor of postoperative liver failure. World J Surg. 2008; 32(11): 2410–2418, doi: 10.1007/s00268-008-9725-3, indexed in Pubmed: 18758848.
11. Miki K, Kubota K, Kokudo N, et al. Asialoglycoprotein receptor and hepatic blood flow using technetium-99m-DTPA-galactosyl human serum albumin. J Nucl Med. 1997; 38(11): 1798–1807, indexed in Pubmed: 9374359.
12. Morikatsu Y, Toru B, Shinya S, et al. Noriko, 99mTc-GSA SPECT/CT fused images for assessment of hepatic function and hepatectomy planning. Ann Transl Med. 2015; 3: 17.
13. Tokorodani R, Sumiyoshi T, Okabayashi T, et al. Liver fibrosis assessment using 99mTc-GSA SPECT/CT fusion imaging. Jpn J Radiol. 2019; 37(4): 315–320, doi: 10.1007/s11604-019-00810-w, indexed in Pubmed: 30656542.
14. Matumoto T, Iinuma TA, Ishikawa T, et al. [SOL-detectability of liver SPECT--analysis of the structure of ROC-curve]. Radioisotopes. 1985; 34(9): 486–492, doi: 10.3769/radioisotopes.34.9_486, indexed in Pubmed: 3878978.
15. Mori Y, Kawakami K, Machida K, et al. A cooperative group study of clinical efficacy of the liver SPECT. Radioisotopes. 1987; 36(9): 457–464, doi: 10.3769/radioisotopes.36.9_457.
16. Zeintl J, Vija AH, Yahil A, et al. Quantitative accuracy of clinical 99mTc SPECT/CT using ordered-subset expectation maximization with 3-dimensional resolution recovery, attenuation, and scatter correction. J Nucl Med. 2010; 51(6): 921–928, doi: 10.2967/jnumed.109.071571, indexed in Pubmed: 20484423.
17. Nakahara T, Daisaki H, Yamamoto Y, et al. Use of a digital phantom developed by QIBA for harmonizing SUVs obtained from the state-of-the-art SPECT/CT systems: a multicenter study. EJNMMI Res. 2017; 7(1): 53, doi: 10.1186/s13550-017-0300-5, indexed in Pubmed: 28639254.
18. Tokorodani R, Ueta K, Kume T, et al. Evaluation of Normal Bone Standardized Uptake Values Using Quantitative SPECT with Improved Spatial Resolution. Kakuigaku gijyutu. 2017(3): 201–210.
19. Hasegawa D, Onishi H. Evaluation of Accuracy for Quantitative Predictor of Hepatic Functional Reserve Using Planar and SPECT Images in the Tc-GSA Scintigraphy. Nihon Hoshasen Gijutsu Gakkai Zasshi. 2017; 73(10): 1055–1060, doi: 10.6009/jjrt.2017_JSRT_73.10.1055, indexed in Pubmed: 29057777.
20. de Dr, Strijckmans V, Almeida P, et al. Boneequivalent liquid solution to asses accuracy of transmission measurements in SPECT and PET. IEEE Trans Nucl Sci. 1997; 44: 1186–90.
21. Torizuka K, Ha-Kawa SK, Kudo M, et al. Phase III multi-center clinical study on 99mTc-GSA, a new agent for functional imaging of the liver. Kaku Igaku. 1992(29): 159–181.

22. Bland JM, Altman DG. Statistical methods for assessing agreement between two methods of clinical measurement. Lancet. 1986; 1(8476): 307–310, indexed in Pubmed: 2868172.
23. Kanda Y. Investigation of the freely available easy-to-use software ‘EZR’ for medical statistics. Bone Marrow Transplant. 2013; 48(3): 452–458, doi: 10.1038/bmt.2012.244, indexed in Pubmed: 23208313.
24. Imaeda T, Kanematsu M, Asada S, et al. Utility of Tc-99m GSA SPECT imaging in estimation of functional volume of liver segments in health and liver diseases. Clin Nucl Med. 1995; 20(4): 322–328, doi: 10.1097/00003072-199504000-00008, indexed in Pubmed: 7788989.
25. Kotani K, Kawabe J, Higashiyama S, et al. Heterogeneous liver uptake of Tc-99m-GSA as quantified through SPECT/CT helps to evaluate the degree of liver fibrosis: A retrospective observational study. Medicine (Baltimore). 2018; 97(31): e11765, doi: 10.1097/MD.0000000000011765, indexed in Pubmed: 30075603.

VIA MEDICA

Nuclear Medicine Review 2021, 24, 1: 11–15
DOI: 10.5603/NMR.2021.0002

ISSN 1506–9680

Original

Age, BMI and diabetes as independent predictors of brain hypoperfusion

Zita Képes[1], Ferenc Nagy[2], Ádám Budai[2], Sándor Barna[2], Regina Esze[3], Sándor Somodi[3], Miklós Káplár[3], Ildikó Garai[1,2], József Varga[1]

[1]University of Debrecen, Faculty of Medicine, Department of Medical Imaging, Division of Nuclear Medicine and Translational Imaging, Hungary
[2]Scanomed Ltd. Nuclear Medicine Centers, Hungary
[3]University of Debrecen, Faculty of Medicine, Department of Internal Medicine, Hungary

[Received 6 VII 2020; Accepted 6 X 2020]

Abstract

Background: Cerebral blood flow abnormalities are supposed to be potential risk factors for developing cognitive dysfunction in the general population. Aging, obesity and type 2 diabetes mellitus are associated with perfusion abnormalities leading to cognitive impairment, neurodegeneration and future development of dementia. In our study, we aimed at identifying independent factors that contribute to the appearance of regional brain perfusion changes besides those that are already known.

Material and methods: Forty-three type 2 diabetic and twenty-six obese patients were enrolled. After the intravenous administration of 740 MBq ^{99m}Tc-hexamethylpropylene amine oxime (HMPAO), all subjects underwent brain perfusion SPECT imaging applying AnyScan S Flex dual-head gamma camera (Mediso, Hungary). Using Philips Achieva 3T scanner brain resting-state functional MRI was also performed. The SPECT and MRI images were co-registered and transformed to the MNI152 atlas space so that data of the following standard volumes of interest (VOIs) could be obtained: frontal lobe, parietal lobe, temporal lobe, occipital lobe, limbic region, cingulate, insula, basal ganglia, cerebrum, limbic system and brain stem. Using the SPSS 25 statistical software package, general linear regression analysis, Student's t-test, and Mann-Whitney U-test were applied for statistical analyses.

Results: Multivariate linear analysis identified that BMI and age are significantly ($p < 0.0001$) associated with perfusion, and patient group was slightly above threshold ($p = 0.0524$). We also found that the presence of diabetes was an independent significant predictor of normalized regional brain perfusion only in the insula ($p < 0.001$). Other independent predictors of normalized regional brain perfusion were: age in the insula ($p < 0.001$) and in the limbic region ($p < 0.01$), and BMI in the brain stem ($p < 0.01$).

Conclusions: Age and BMI proved to be general, and diabetes regional predictor of brain hypoperfusion. BMI appeared to be a novel factor affecting brain perfusion. In one specific region, the insula, we detected a difference between the obese and the diabetic group. These findings may be significant in the understanding of the development of cognitive impairment in metabolic diseases.

KEY words: brain perfusion; SPECT; type 2 diabetes mellitus; obesity; insula; limbic region; brain stem

Nucl Med Rev 2021; 24, 1: 11–15

Introduction

Cerebral blood flow alteration is supposed to be a potential risk factor for developing cognitive dysfunction in the general population [1, 2]. Aging, obesity, and type 2 diabetes mellitus (T2DM) are associated with perfusion abnormalities leading to cognitive impairment, neurodegeneration and future development of dementia.

Recent data pointed out particular brain areas with perfusion deficit related to aging. Aanerud et al. [3] detected the magnitudes of regional cerebral blood flow (rCBF) and cerebral metabolic rate of oxygen (CMRO2), two significant parameters characterizing brain aging, in areas of cerebral cortex in a PET study with sixty-six healthy volunteers enrolled aged between twenty-one and eighty-one [4]. The inferior parietal lobules showed perfusion deficit in cognitively normal aging subjects by Okonkwo et al. [5]. In a ^{99m}Tc-HMPAO study with forty healthy young and twenty-eight aged subjects involved, Catafau et al. [6] found significantly lower rCBF ratios in aged subjects than in the young in the left frontal

Correspondence to: Zita Képes, University of Debrecen, Faculty of Medicine, Department of Medical Imaging, Division of Nuclear Medicine and Translational Imaging, Hungary
e-mail: zitakepes@gmail.com

lobe and the posterior region of the left temporal lobe. Aging is associated with vascular pathology such as cortical microinfarcts, grey matter lacunae and irreversible endothelial dysfunction [7–13]. These vascular alterations contribute to the appearance of age-related brain hypoperfusion that probably leads to the development of neurodegenerative diseases.

Metabolic conditions such as obesity and T2DM that frequently appear and progress together with aging are also linked to brain perfusion abnormalities that may lead to future neurodegeneration.

According to Bissels et al. [14] the risk of dementia is 73% higher in type two diabetic patients than in patients without T2DM. The Italian Longitudinal Study on Aging in which patients with mild cognitive impairment and metabolic syndrome were studied supports the connection between obesity and dementia [15]. Birdsill et al. [16] detected a 15 per cent lower mean grey matter cerebral blood flow in subjects with metabolic syndrome that could be associated with decreased memory function. Cui Y. et al. [17] found decreased CBF in T2DM in the posterior cingulate cortex, precuneus and bilateral occipital lobe. Willeumier K. et al. [18] indicated that higher body mass index (BMI) in healthy individuals is associated with decreased rCBF in the following Brodmann areas: 8, 9, 10, 11, 32, and 44 that are brain regions involved in attention, reasoning, and executive function. They also pointed out that an elevated BMI is connected to decreased rCBF in the prefrontal cortex in a group of healthy subjects.

In our study, we aimed at identifying independent factors that contribute to the appearance of regional brain perfusion alterations besides those factors that are already known.

Material and methods

A total of forty-three type 2 diabetic and twenty-six obese patients were enrolled. The main anthropometric characteristics of the subjects are shown in Table 1. Among the diabetics there were seventeen female and twenty-six male, while in the obese group eighteen female and eight male subjects were involved.

Patients were all recruited from the Department of Internal Medicine of the University of Debrecen as well as a Private General Practice from the city of Miskolc.

Patients were selected based on the following inclusion criteria: age between 18 and 70, manifest obesity (BMI > 30) or controlled type 2 diabetes, and no history of mental or brain disorders. Exclusion criteria included: gravidity, breastfeeding, acute or chronic inflammatory disease, severe liver disease, ongoing steroid treatment, hyperthyroidism, retinoid intake, history of malignant diseases with the exception of basal cell carcinoma, crural ulcer, change in the therapy in the previous 6 months and anticoagulant treatment.

All procedures followed were in accordance with the ethical standards of the responsible national committee on human experimentation (OGYEI/2829-4/2017). Before enrolment, subjects were given detailed information concerning the aims of the study as well as the examinations. Informed consent was collected from all patients involved.

Single-photon emission-computed tomography (SPECT) image acquisition

AnyScan S Flex (Mediso, Hungary) dual-head gamma-camera equipped with low-energy high resolution parallel hole collimators was used to image brain perfusion. Patients were not prone to stress or heavy emotional burden before the actual examination. Half an hour before the injection of the radiopharmaceutical subjects were given one perchlorate capsule *per os* to block thyroid uptake. 740 MBq ^{99m}Tc-hexamethylpropylene amine oxime (HMPAO) was administered into the right cubital vein after a ten-minute rest in the dimly-lit examination room.

The main characteristics of SPECT examinations were the following: 120 views, 128 x 128 matrix with 2.36 mm pixel size, 30 sec projection time, with auto body contour.

Brain magnetic resonance imaging (MRI)

Brain resting-state functional MRI was carried by a Philips Achieva 3T scanner. T1-weighted 3D images (voxel size: 0.5 x 0.5 x 1 mm, matrix size: 480 x 480 x 175) were obtained. The T1-weighted 3D turbo field echo protocol was applied for image acquisition with 8 ms repetition time (TR) and 3.7 ms echo time (TE).

Image processing

First, the ^{99m}Tc-HMPAO SPECT image of each subject was registered to his/her T1-weighted MRI image by rigid transformation, using the FMRIB's Linear Image Registration Tool (FLIRT) linear registration software. Then we transformed T1 weighted MRI images of the patients by elastic transformation to the MNI152-space (2 x 2 x 2 mm voxel size) using the advanced normalization tools (ANTS)

Table 1. Most important anthropometric parameters of patients involved

	Obes		Diabetes			
	median	SD	median	SD	test	P
Age	53.5	± 9.89	50	± 8.59	t	> 0.1
Height (cm)	168	± 11.70	170	± 8.77	t	> 0.1
Body weight (kg)	103	± 18.10	95	± 21.48	t	0.045
BMI	35.68	± 5.58	32.41	± 5.28	M-W	< 0.01
Blood glucose level (mmol/L)	5.8	± 0.58	7.2	± 1.72	M-W	< 0.0001
(Tests: M-W: Mann-Whitney; t: Student's t)						

BMI — body mass index; SD — standard deviation

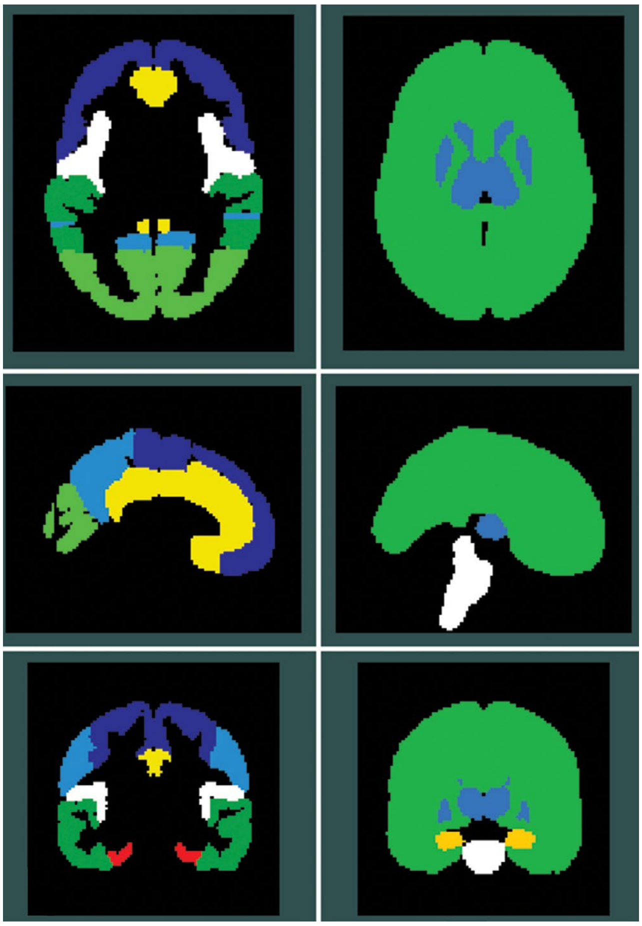

Figure 1. Showing aggregated brain regions created on the basis of Harvard-Oxford atlas

linear and non-linear image registration [19]. The combination of both transformations was applied to the SPECT image to transfer it to the MNI space, so that data of the following standard volumes of interest (VOIs) could be obtained: frontal lobe, parietal lobe, temporal lobe, occipital lobe, limbic region, cingulate, insula, basal ganglia, cerebrum, limbic system and brain stem. The aggregated brain regions that were used for VOIs are demonstrated in Figure 1.

Statistical analyses

The SPSS 25 statistical software package (SPSS Inc.) was used for data analysis. To identify influencing factors, general linear regression analysis was performed with Hochberg's correction for multiple regions. Student's t-test was used to compare parameters with normal distribution while Mann-Whitney U test was applied for the comparison of parameters with non-Gaussian distribution.

Results

We investigated factors that may be associated with cerebral perfusion (normalized to the occipital region) by the general linear model. First, we included the patient group (DM or obese) and gender as factors and age, blood glucose and BMI as covariates. BMI (Mann-Whitney: $p = 0.004$) and glucose level (Mann-Whitney: $p < 0.0001$) were integrated in the model since these parameters were significantly different in the two observed groups as seen in Figure 2. However, based on Student's t-test there was no statistically significant difference between the two groups regarding age (Fig. 2), because of previous findings in the literature, we also included age in the analysis. Since the effect of blood glucose level on brain perfusion was far from significant both in the multivariate model and in all regions ($p > 0.1$), we eliminated it from the model.

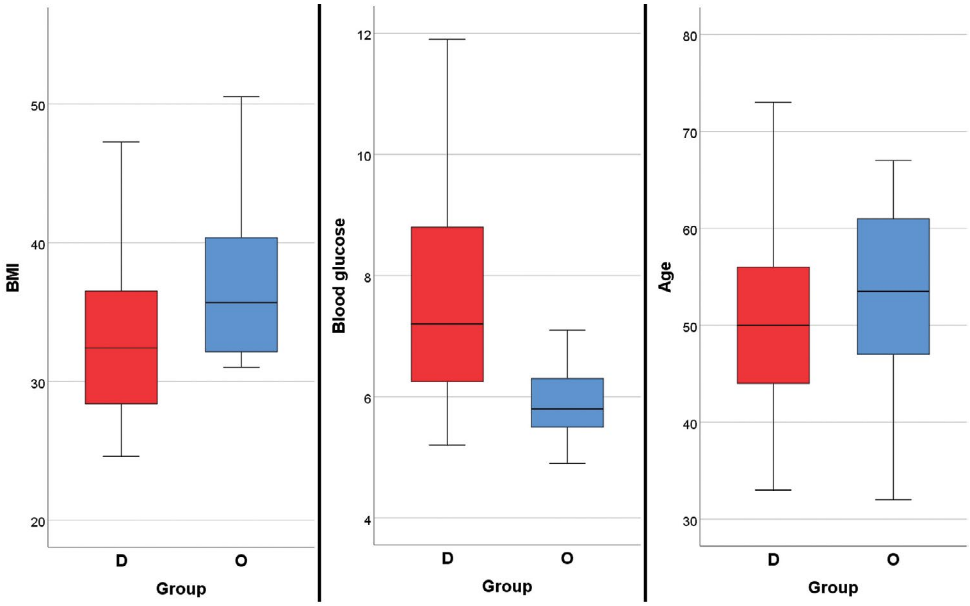

Figure 2. Box-and whiskers plots showing the most important continuous parameters in both groups: BMI, serum blood glucose level and age. BMI — body mass index

From the remaining variables, multivariate analysis with all brain regions as dependent variables identified that BMI and age are significantly ($p < 0.0001$) associated with perfusion; and patient group was slightly above threshold ($p = 0.0524$).

Univariate contrast of the group in all but one brain region was negative (normalized perfusion was lower in DM), but after applying Hochberg's correction for multiple comparisons, we found that the presence of DM was an independent significant predictor of normalized regional brain perfusion only in the insula ($p < 0.001$).

Other independent predictors of normalized regional brain perfusion were:

age in the insula ($p < 0.001$) and in the limbic region ($p < 0.01$)

BMI in the brain stem ($p < 0.01$)

Discussion

We detected age-dependent hypoperfusion specifically in the region of the insula and in the limbic region. The direct connection between aging and the involvement of these two specific brain regions is not exactly known.

Age is considered to be an important predictor of hypoperfusion [20]. In the long run cerebral hypoperfusion results in cognitive dysfunction. Bonthius D. J. et al. [21] stated that the limbic region is much more burdened with neurofibrillary tangles than other brain regions. This finding supports the connection between cognitive dysfunction and limbic perfusion abnormality. Since we examined patients with normal cognition we speculate that the early involvement of the limbic region could be characteristic in patients who might be at risk for Alzheimer's disease (AD) even without manifest clinical signs actually present. Since both the insula and the limbic region are related to AD pathology, the involvement of these brain areas in the process of brain aging may predict the appearance of future dementia.

Cerebral perfusion defects induced by aging could be triggered by both obesity and T2DM. We suppose that these metabolic disorders could enhance vascularly triggered age-related cognitive deficit. Our finding is in coherence with the findings of Leanne et al. [22] who detected lower cerebral blood flow in type 2 diabetic patients with mild cognitive impairment in the insula, medial temporal lobes and in the frontal lobes compared to type 2 diabetic patients without mild cognitive impairment and healthy controls. Further, they also reported association between regional cerebral blood flow measurements and Addenbrooke's Cognitive Assessment (ACE-R) score in the insula, thalamus and medial temporal lobes.

Our second finding was BMI-associated hypoperfusion specifically in the brain stem. To our knowledge, there is no similar finding in the literature. The reason behind this result is unclear yet. We presume that an excessive amount of adipose tissue in that brain area possibly has a compressive effect on the vasculature of the brain stem. This may induce and accelerate brain stem hypoperfusion together with high BMI-induced altered insulin regulation, leptin-resistance, inflammatory processes, and vascular abnormalities. Further, obesity-related endothelial dysfunction and disrupted smooth muscle function could be other causes of cerebral hypoperfusion in obesity. All these factors are strongly connected to neurodegeneration. We speculate that BMI-related hypoperfusion in the brain stem may contribute to the development of future dementia. Obesity-induced cerebral blood flow reduction promotes amyloid-beta production that causes endothelial dysfunction leading to cognitive impairment [22, 23]. This could be in line with the findings of Gunstad J. et al. [25] who detected that people with elevated BMI have reduced executive function. The outcomes of Gustafson et al. [26] also support this hypothesis. They evaluated the connection between BMI and brain atrophy, the main marker of neurodegeneration. They showed that the risk of temporal atrophy increased by 3% per 1.0 kg/m^2 increase in BMI that could predict the development of cognitive decline.

Finally, we found that the presence of diabetes was an independent significant predictor of normalized regional brain perfusion only in the region of the insula. We speculate that insular perfusion may be affected much earlier by diabetes, and insula is much more vulnerable to metabolic changes than other brain regions. This could be one reason for the unique involvement of disease-related insular perfusion alteration. Although, the fact that we examined well-controlled diabetic patients might also explain why we only detected perfusion difference in the insula. Insula is involved in the pathophysiology of AD [21]. Consequently, our finding puts the emphasis on the elevated risk for dementia in diabetics. Additionally, hyperglycemia characterizing diabetes causes altered endothelial dependent cerebral vasodilation, oversecretion of vasoconstrictor endothelin-1 and blood-brain barrier impairment [27]. These factors could also strengthen the link between hyperglycemia, diabetes and chronic cerebral hypoperfusion which is an important element of vascular cognitive impairment [27].

However, the discrepancy can be detected in the literature concerning the association between diabetes and brain hypoperfusion. Recent research has pointed out that studies involving a small number of patients with severe symptoms tend to detect hypoperfusion in T2DM [28]. In addition, these researchers do not take atrophy into account that could possibly explain hypoperfusion.

There are important limitations to our study worth noting. First, we did not include a healthy control group due to ethical reasons. Second, we involved well-treated diabetic patients taking different types of medications (antidiabetics with different mechanisms of action, antihypertensive and lipid-lowering drugs, and antidiuretics).

Conclusions

We managed to detect three factors that influence brain perfusion. Age, - and BMI proved to be general, and diabetes regional predictor of brain hypoperfusion. Our result regarding the effect of age on cerebral perfusion that is well known from the literature is in line with previous studies. Based on multiparametric linear analysis BMI appeared to be a relatively new factor influencing brain perfusion. Further, in one specific region, in the insula, we detected difference between the obese and the diabetic group.

Our findings put the emphasis on the multi-aetiological nature of cerebral hypoperfusion. We emphasize that it is important to identify independent factors affecting brain perfusion. This could be essential to help understand the pathological mechanisms that occur behind the elevated risk of developing cognitive impairment in metabolic diseases.

Acknowledgement

This research was supported by the National Grant No. GINOP-2.1.1-15-2015-00609.

Disclosure

The authors report no biomedical financial interests or potential conflicts of interest.

References

1. 1Ishiwata A, Sakayori O, Minoshima S, et al. Preclinical evidence of Alzheimer changes in progressive mild cognitive impairment: a qualitative and quantitative SPECT study. Acta Neurologica Scandinavica. 2006; 114(2): 91–96, doi: 10.1111/j.1600-0404.2006.00661.x.
2. Jagust WJ, Eberling JL, Reed BR, et al. Clinical studies of cerebral blood flow in Alzheimer's disease. Ann N Y Acad Sci. 1997; 826: 254–262, doi: 10.1111/j.1749-6632.1997.tb48477.x, indexed in Pubmed: 9329697.
3. Aanerud J, Borghammer P, Chakravarty M, et al. Brain Energy Metabolism and Blood Flow Differences in Healthy Aging. Journal of Cerebral Blood Flow & Metabolism. 2012; 32(7): 1177–1187, doi: 10.1038/jcbfm.2012.18.
4. Daulatzai MA. Cerebral hypoperfusion and glucose hypometabolism: Key pathophysiological modulators promote neurodegeneration, cognitive impairment, and Alzheimer's disease. J Neurosci Res. 2017; 95(4): 943–972, doi: 10.1002/jnr.23777, indexed in Pubmed: 27350397.
5. Okonkwo OC, Xu G, Oh JM, et al. Cerebral blood flow is diminished in asymptomatic middle-aged adults with maternal history of Alzheimer's disease. Cereb Cortex. 2014; 24(4): 978–988, doi: 10.1093/cercor/bhs381, indexed in Pubmed: 23236200.
6. Catafau A, Lome a F, Pavia J, et al. Regional cerebral blood flow pattern in normal young and aged volunteers: a99mTc-HMPAO SPET study. European Journal of Nuclear Medicine. 1996; 23(10): 1329–1337, doi: 10.1007/bf01367588.
7. Bouras C, Kövari E, Herrmann F, et al. Stereologic Analysis of Microvascular Morphology in the Elderly. Journal of Neuropathology and Experimental Neurology. 2006; 65(3): 235–244, doi: 10.1097/01.jnen.0000203077.53080.2c.
8. Jeynes B, Provias J. The possible role of capillary cerebral amyloid angiopathy in Alzheimer lesion development: a regional comparison. Acta Neuropathol. 2006; 112(4): 417–427, doi: 10.1007/s00401-006-0099-z, indexed in Pubmed: 16830133.
9. Kövari E, Gold G, Herrmann F, et al. Cortical Microinfarcts and Demyelination Significantly Affect Cognition in Brain Aging. Stroke. 2004; 35(2): 410–414, doi: 10.1161/01.str.0000110791.51378.4e.
10. Kövari E, Gold G, Herrmann FR, et al. Cortical microinfarcts and demyelination affect cognition in cases at high risk for dementia. Neurology. 2007; 68(12): 927–931, doi: 10.1212/01.wnl.0000257094.10655.9a.
11. Gold G, Kövari E, Herrmann F, et al. Cognitive Consequences of Thalamic, Basal Ganglia, and Deep White Matter Lacunes in Brain Aging and Dementia. Stroke. 2005; 36(6): 1184–1188, doi: 10.1161/01.str.0000166052.89772.b5.
12. Thal DR, Capetillo-Zarate E, Larionov S, et al. Capillary cerebral amyloid angiopathy is associated with vessel occlusion and cerebral blood flow disturbances. Neurobiol Aging. 2009; 30(12): 1936–1948, doi: 10.1016/j.neurobiolaging.2008.01.017, indexed in Pubmed: 18359131.
13. Hallam K, Li Q, Ananthakrishnan R, et al. Aldose Reductase and AGE-RAGE pathways: central roles in the pathogenesis of vascular dysfunction in aging rats. Aging Cell. 2010; 9(5): 776–784, doi: 10.1111/j.1474-9726.2010.00606.x.
14. Biessels G, Strachan M, Visseren F, et al. Dementia and cognitive decline in type 2 diabetes and prediabetic stages: towards targeted interventions. The Lancet Diabetes & Endocrinology. 2014; 2(3): 246–255, doi: 10.1016/s2213-8587(13)70088-3.
15. Solfrizzi V, Scafato E, Capurso C, et al. Italian Longitudinal Study on Aging Working Group. Metabolic syndrome, mild cognitive impairment, and progression to dementia. The Italian Longitudinal Study on Aging. Neurobiol Aging. 2011; 32(11): 1932–1941, doi: 10.1016/j.neurobiolaging.2009.12.012, indexed in Pubmed: 20045217.
16. Birdsill AC, Carlsson CM, Willette AA, et al. Low cerebral blood flow is associated with lower memory function in metabolic syndrome. Obesity (Silver Spring). 2013; 21(7): 1313–1320, doi: 10.1002/oby.20170, indexed in Pubmed: 23687103.
17. Cui Y, Liang X, Gu H, et al. Cerebral perfusion alterations in type 2 diabetes and its relation to insulin resistance and cognitive dysfunction. Brain Imaging Behav. 2017; 11(5): 1248–1257, doi: 10.1007/s11682-016-9583-9, indexed in Pubmed: 27714551.
18. Willeumier K, Taylor D, Amen D. Elevated BMI Is Associated With Decreased Blood Flow in the Prefrontal Cortex Using SPECT Imaging in Healthy Adults. Obesity. 2012; 19(5): 1095–1097, doi: 10.1038/oby.2011.16.
19. Avants BB, Tustison N, Song G. Advanced normalization tools (ANTS). Insight J. 2009; 2(365): 1–35.
20. Jansen JFA, van Bussel FCG, van de Haar HJ, et al. Cerebral blood flow, blood supply, and cognition in Type 2 Diabetes Mellitus. Sci Rep. 2016; 6(1): 10, doi: 10.1038/s41598-016-0003-6, indexed in Pubmed: 27920431.
21. Bonthius D, Solodkin A, Hoesen GV. Pathology of the Insular Cortex in Alzheimer Disease Depends on Cortical Architecture. Journal of Neuropathology and Experimental Neurology. 2005; 64(10): 910–922, doi: 10.1097/01.jnen.0000182983.87106.d1.
22. HUNT L, SELVARAJAH D, TESFAYE S, et al. Cerebral Blood Flow Abnormalities in Brain Regions Responsible for Cognitive Function in Type 2 Diabetes. Diabetes. 2018; 67(Supplement 1), doi: 10.2337/db18-1798-p.
23. Toda N, Ayajiki K, Okamura T. Obesity-induced cerebral hypoperfusion derived from endothelial dysfunction: one of the risk factors for Alzheimer's disease. Curr Alzheimer Res. 2014; 11(8): 733–744, doi: 10.2174/156720501108140910120456, indexed in Pubmed: 25212912.
24. Torre JCd, Pappas BA, Prevot V, et al. Hippocampal nitric oxide upregulation precedes memory loss and A 1-40accumulation after chronic brain hypoperfusion in rats. Neurological Research. 2013; 25(6): 635–641, doi: 10.1179/016164103101201931.
25. Gunstad J, Paul RH, Cohen RA, et al. Elevated body mass index is associated with executive dysfunction in otherwise healthy adults. Compr Psychiatry. 2007; 48(1): 57–61, doi: 10.1016/j.comppsych.2006.05.001, indexed in Pubmed: 17145283.
26. Gustafson D, Lissner L, Bengtsson C, et al. A 24-year follow-up of body mass index and cerebral atrophy. Neurology. 2004; 63(10): 1876–1881, doi: 10.1212/01.wnl.0000141850.47773.5f.
27. Livingston JM, McDonald MW, Gagnon T, et al. Influence of metabolic syndrome on cerebral perfusion and cognition. Neurobiol Dis. 2020; 137: 104756, doi: 10.1016/j.nbd.2020.104756, indexed in Pubmed: 31978604.
28. Sabri O, Hellwig D, Schreckenberger M, et al. Influence of diabetes mellitus on regional cerebral glucose metabolism and regional cerebral blood flow. Nucl Med Commun. 2000; 21(1): 19–29, doi: 10.1097/00006231-200001000-00005, indexed in Pubmed: 10717898.

Review

Nuclear Medicine Review 2021, 24, 1: 16–26
DOI: 10.5603/NMR.2021.0004
Copyright © 2021 Via Medica
ISSN 1506–9680

Breast Cancer and PET Imaging

Ismet Sarikaya
Kuwait University Faculty of Medicine, Department of Nuclear Medicine, Kuwait City, Kuwait

[Received 16 V 2020; Accepted 21 X 2020]

Abstract

Breast cancer is the most common malignancy in women and among the most common indications of oncologic positron emission tomography (PET) studies. In this review article, updated anatomical, pathological, and clinical information about breast cancer were provided for Nuclear Medicine physicians to better understand breast cancer and interpret PET images and a review of the literature on the use of PET imaging in breast cancer was summarized.

KEY words: Breast cancer; PET, FDG; NaF; FES

Nucl Med Rev 2021; 24, 1: 16–26

Introduction

Breast cancer is the most common malignancy in women worldwide (2.1 million women each year) [1]. Approximately 627,000 women died from breast cancer in 2018 [1]. Breast cancer rates are higher in western countries but also increasing in the rest of the world. Breast cancer incidence and death rates generally increase with age. Survival is affected by the stage of the disease as well as histological and molecular subtypes and genomic profile of the breast cancer and ranges from 99% to 27% [2].

Breast cancer is among the most common oncologic indications of clinical Positron emission tomography/computed tomography (PET/CT) studies. Among various PET radiotracers, ^{18}F-fluorodeoxyglucose (FDG) and ^{18}F-sodium fluoride (NaF) are the main radiotracers used in clinical PET studies for initial staging of locally advanced invasive and inflammatory breast cancers, to assess response to treatments and to detect and localize the recurrent disease. More specific PET radiotracers, such as ^{18}F-fluoroestradiol (FES/oestrogen receptor binding), ^{18}F-fluorothymidine (FLT/cell proliferation), ^{89}Zr-trastuzumab (human epidermal growth factor receptor 2 (HER2) binding) ^{18}F-galacto-RGD (angiogenesis), ^{18}F-annexin-V (apoptosis), ^{89}Zr-anti-gH2AX-TAT (cell death), ^{18}F-FMISO (hypoxia) are mainly used for investigational purpose.

This review article aims to provide practically useful information about breast cancer and the role of PET/CT in the management of breast cancer.

Anatomy and Histology of the Breast

Breasts overly the pectoralis major muscles with a fascia in between them. The mammary gland is an exocrine *gland* composed of mammary lobules and network of ducts. Each mammary lobule consists of small glandular structures (acini) which open into the terminal duct (terminal duct lobular unit, TDLU). Ducts and mammary lobules are surrounded by connective tissue which is composed of blood and lymphatic vessels, nerves, adipose and fibrous tissue [3].

Breasts have 2 superficial (cutaneous and subcutaneous) and 2 deep (mammary-glandular and fascial) intercommunicating lymphatic plexi. Superficial lymphatics drain the skin, whereas deep lymphatics drain the breast parenchyma, areola and the nipple. The density of the lymphatic plexus is higher in the subareolar region (Sappey's plexus). In 1874, Sappey suggested that axillary nodes receive lymphatic drainage from the entire breast via the subareolar plexus. However, the role of the subareolar plexus in the lymphatic drainage of the breast is still controversial [4]. Approximately 75% of breast lymphatic drainage is directed to the axilla and 25% to the internal mammary nodes [5]. However, internal mammary node drainage was seen in 28–44% of all patients with breast carcinomas on lymphoscintigraphy studies [6]. There are three levels of lymph nodes in the axilla. Level I nodes are inferolateral to the pectoralis minor, level II nodes are behind the pectoralis minor, and level 3 nodes are superomedial to the pectoralis minor. Axillary lymphatic drainage generally proceeds in a stepwise fashion from level I to level II, to level III and finally into the thoracic duct. When there is an obstruction in the axillary lymphatic flow or after the axillary dissection, alternative pathways may become important for the lymphatic drainage (altered lymphatic drainage) through various lymph nodes such as internal mammary, presternal, retrosternal, transpectoral, retro pectoral, posterior intercostal and subdiaphragmatic (Gerota's route) nodes. The lymph nodes between pectoralis minor and major muscles (interpectoral) are called rotter space nodes.

Diagnosis of Breast Cancer

For women at average breast cancer risk, American Cancer Society (ACS) recommends yearly screening mammogram for women 45 to 54-year-old [7]. Women 55 year and older can have a mammogram yearly or every other year [7]. For women at high

Correspondence to: Ismet Sarikaya
Department of Nuclear Medicine, Faculty of Medicine, Kuwait University, PO Box 24923 Safat, Kuwait 13110
phone: (965) 25319592 / 6414; fax: (965) 25338936
e-mail: isarikaya99@yahoo.com

breast cancer risk, ACS recommends yearly breast magnetic resonance imaging (MRI) and a mammogram, typically starting at age 30 [7]. High risk includes having a family history of breast cancer, history of radiation therapy to the chest between the ages of 10 and 30 years, and patient or 1st degree relative to have a BRCA1 or BRCA2 gene mutation, Li-Fraumeni syndrome, Cowden syndrome, or Bannayan-Riley-Ruvalcaba syndrome [7].

Screening mammograms mainly search for calcification and masses and also assess the density of the breast. Macro-calcifications are usually due to benign conditions. Micro-calcifications are more concerning than macro-calcifications. Thirty per cent of patients with breast micro-calcifications showed malignancy on histopathology [8]. Dense breasts are linked to a higher risk of breast cancer. Dense breast tissue can also prevent the detection of cancers on a mammogram. To describe mammogram findings, a standard system is used (Breast Imaging Reporting and Data System (BI-RADS)) [7]. BI-RADS scores range from 0 to 6; 0: Incomplete study, additional imaging and/or comparison to prior mammograms is needed, 1: Negative study, 2: Benign findings, 3: Probably benign findings with follow-up in 6 mos, 4: Suspicious findings, biopsy should be considered, 5: Highly suggestive of malignancy, biopsy should be considered, and 6: Known biopsy-proven malignancy.

Breast ultrasound helps to differentiate simple cysts from solid masses and guide biopsy. Breast MRI has a limited role in the screening of breast cancer, but it should be considered in women who have a high risk of breast cancer. After the diagnosis of breast cancer, MRI is useful to assess the primary tumour (tumour size, multifocal vs multicentre disease) and chest wall invasion.

Classification of Breast Cancers

Most breast cancers are adenocarcinoma and arise from the epithelial cells of the TDLU. A small number of breast cancers arise in the other tissues such as fat, muscle, and connective tissue. As the glandular tissue is more abundant in the upper outer quadrant of the breast, half of the breast cancers occur in this region [9].

Histological classification of breast cancers includes in-situ carcinoma (cancerous cells remain in the place and have not spread yet) and invasive or infiltrating carcinoma (cancer cells spread beyond the layer of tissue in which they developed).

In situ carcinomas are classified as ductal carcinoma in situ (DCIS or intraductal carcinoma) and Paget's disease. DCIS is a non-invasive, pre-invasive breast cancer where proliferations of malignant ductal epithelial cells remain confined within intact breast ducts. Paget's disease is a rare type of breast cancer involving the skin of the nipple. Paget's disease is usually linked to DCIS or invasive ductal carcinoma (IDC). Lobular carcinoma in-situ is treated as a benign entity and has been removed from TNM staging. It is considered as a proliferative disease with associated risk for developing breast cancer in the future [9].

The invasive breast carcinomas are classified as ductal, inflammatory, medullary, medullary with lymphoid stroma, mucinous, papillary (predominantly micropapillary pattern), tubular, lobular, infiltrating Paget's disease, undifferentiated, squamous cell, adenoid cystic, secretory, and cribriform [10]. If the tumour has no specific differentiating features, it is called invasive carcinoma not otherwise specified (NOS). Invasive mammary cancer has features of both ductal carcinoma and lobular carcinoma. IDC is the most common invasive tumour of the breast which comprises 72–80 % of all invasive breast cancers [11]. Invasive lobular carcinoma (ILC) accounts for 5–15 % and inflammatory breast cancer accounts for 1% to 2% of all invasive breast cancers [2, 11]. IDC is further sub-classified as well-differentiated (grade 1), moderately differentiated (grade 2) or poorly differentiated (grade 3) based on the levels of nuclear pleomorphism, glandular/tubule formation and mitotic index [12]. Inflammatory carcinoma is characterized by diffuse erythema and oedema (peau d'orange) in the skin of the breast with a rapid evolution [9]. Inflammatory carcinoma is a clinical-stage T4d cancer and the most aggressive presentation of breast cancer [13]. An underlying mass may or may not be palpable and there may be a detectable mass on the imaging [9]. Changes in the skin may be due to lymphedema caused by tumour emboli within dermal lymphatics [9,]. ILC of the breast shows low histological grade and low mitotic count [14].

Hormone receptor (oestrogen receptor (ER) and progesterone receptor (PR)) and human epidermal growth factor receptor 2 (HER2) expressions of breast cancer are assessed via qualitative and/or semi-quantitative immunohistochemistry technique on biopsied tissues.

Through molecular analysis and gene expression profiling, breast cancer is sub-classified into luminal A (ER+/PR+), luminal B (ER+/PR+/HER2 + or -, Ki67+), HER2 enriched (HER2+) and basal-like (triple-negative, ER-/PR-/HER2-).

ER+ tumours comprise up to 75% of all breast cancer patients. ER+ tumours largely well-differentiated and less aggressive [15]. PR+ tumours are mostly ER+ [16]. ER+PR- tumours are less responsive to endocrine treatment than ER+PR+ tumours [16]. HER2 positivity is associated with poor differentiation and aggressive tumour and seen in 13% to 20% of IDC [16]. HER2 positivity is very rarely seen in low-grade IDC or traditional ILC. ILC is generally positive for hormone receptor and negative for HER2, p53 and basal marker [14].

Ki67 is the most widely used proliferation marker in breast cancer which is predominantly present in cycling cells. It is associated with aggressive tumours, worse prognosis and survival.

P53 is a tumour suppressor gene. Mutation in p53 causes loss of control of cell proliferation. p53 is the most frequently mutated gene in invasive breast cancer which is seen in 30-35% of all cases, and approximately 80% of triple-negative tumours [17].

Genomic assays or tests analyse the tumour tissue to determine if there are certain genes which can affect the cancer growth, spread and recurrence. Genetic testing should not be mistaken for genomic testing. In genetic testing, blood, saliva or other tissues are analysed to determine if there is abnormal change or mutation in a gene which is linked to high risk of cancer development. There are several genomic assays for breast cancer such as OncotypeDx, Mammaprint, Endopredict, PAM50 (Prosigna) and Breast cancer Index [9]. OncotypeDx is the only multigene panel included to classify pathological prognostic staging of breast cancer. The OncotypeDx test analyses the activity of 21 genes and calculates a recurrence score.

Staging of Breast Cancer

Traditional staging (TNM, tumour: T, lymph nodes: N, and distant metastases: M) is still used in places where biomarker tests are not available (Tab. 1) [9]. TNM staging is classified as Clinical "c" and

Table 1. Summary of AJCC TNM staging (clinical T, pathological N)

Tis	DCIS or Paget
T1	Tm size $\leq$ 20
T2	Tm size $>$ 20 mm, $\leq$ 50 mm
T3	Tm size $>$ 50 mm
T4	T4a Extension to chest wall*
	T4b Ulceration or macroscopic nodules in the skin
	T4c T4a + T4b
	T4d Inflammatory carcinoma

*Chest wall: Ribs, intercostal muscles and serratus anterior muscle.
Adherence/invasion to the pectoralis muscle is NOT extension to the chest wall

N0	No regional lymph node metastasis or $\leq$ 0.2 mm
N1	Nmi: Micromet (approximately 200 cells, $>$ 0.2 mm, $<$ 2 mm)
	N1a: Met in 1–3 axillary nodes*
	N1b: Micromet or Macromet ($>$ 2mm) in ipsilateral IM nodes by SLN biopsy
	N1c: N1a + N1b
N2	N2a: Met in 4–9 axillary nodes*
	N2b: Met in ipsilateral IM nodes by imaging, axilla negative
N3	N3a: Met in $\geq$ 10 axillary nodes* or in level 3 (infraclavicular) axillary nodes
	N3b: Met in IM nodes by imaging with 1 or more level 1 and 2 axillary nodes
	N3c: Met in ipsilateral supraclavicular nodes

* at least one metastasis larger than 2.0 mm

M0	No clinical or radiographic evidence of distant metastases or $<$ 0.2 mm*
cM1	Clinical or radiographic evidence of distant metastases
pM1	Histologically proven metastases in distant organs ($>$ 0.2 mm)

*detected by microscopic or molecular techniques
Distant metastasis: Metastasis to distant organs and non-regional lymph nodes

pathological “p” staging. Clinical staging uses information such as patient history, physical examination, and any imaging performed before the surgery and neoadjuvant treatment. Clinical staging can use biopsy results such as fine-needle aspiration (FNA), core biopsy or sentinel lymph node (SLN) biopsy. Pathological staging uses information defined at the surgery. It does not apply to patients treated with systemic or radiation treatment before surgery. Following neoadjuvant systemic therapy, post-therapy pathological staging is defined as “yp”.

In prognostic staging (clinical and pathological), biomarker tests are integrated into TNM staging [9]. Biomarker tests include histological grade, ER, PR, HER2, proliferation markers (Ki-67 or mitotic count) and genomic assays.

Definition of Locally Advanced Disease

Per National Comprehensive Cancer Network (NCCN), locally advanced breast cancer describes a subset of invasive breast cancer where the initial clinical and radiologic evaluation documents advanced disease confined to the breast and regional lymph nodes [10]. Locally advanced breast cancer is also further classified as operable (Clinical stage T3, N1, M0) and inoperable (Clinical stage IIIA [except T3, N1 M0], IIIB, and IIIC). Definition of regional lymph nodes for staging purpose is ipsilateral axillary level 1 and 2, 3, internal mammary, intramammary and supraclavicular nodes [9]. NCCN and the American Joint Committee on Cancer (AJCC) considers level 3 axillary nodes as infraclavicular nodes. Lymph node metastases other than regional lymph nodes (including cervical or contralateral internal mammary or contralateral axillary lymph nodes) is considered as distant metastases.

Breast Cancer Metastases

A seed-and-soil hypothesis is believed to be the mechanism for metastases in breast cancer [18]. Disseminated cancer cells (seeds) reach a microenvironment (soil) and proliferate. Bone, lung, liver, and brain are the common sites for metastatic spread of breast cancer. Breast cancer subtypes are associated with different metastatic patterns. In triple-negative tumours, there is a higher rate of metastases to visceral organs, such as brain, lung and liver, and a lower rate of metastases to bone, whereas bone is a major site of metastasis in ER+ breast cancer and HER2+ subtypes are significantly associated with higher rates of liver, brain, and lung metastases [19–22]. The metastatic patterns of lobular and ductal carcinoma of the breast are also different. Gastrointestinal system, gynecologic organs such as ovary, and peritoneum-retroperitoneum metastases are markedly more prevalent in lobular carcinoma [23, 24].

The main treatments for breast cancer metastasis are standard chemotherapy and targeted therapy. Targeted therapies include hormone therapy, immunological therapy and antiangiogenic therapy. In bone metastases, bone-targeted antiosteoclast agents are also given with antitumor therapy.

Breast Cancer Survival Rates

Per Surveillance Epidemiology and End Results (SEER) database, 5-year relative survival rates for localized, regional and distant involvement are 99%, 86% and 27%, respectively [2]. In localized disease, there is no sign that cancer has spread outside of the breast. In regional disease, cancer has spread outside the breast to nearby structures or lymph nodes.

Per MD Anderson analysis, based on risk profile (tumour grade, ER, PR, HER2), 5-year overall survival ranges from 93.8 to 97% for stage 1, 88.2 to 97.1% for stage IIA, 91.5 to 100% for stage IIB, 68.6 to 100% for stage IIIA, and 33.3 to 84.4% for stage IIIC breast cancer [9]. There were insufficient numbers of cases with Stage IIIB cancer for analysis.

Hormone receptor (HR)+/HER2- subtype shows the best survival (92.5% at 4 years), followed by HR+/HER2+ (90.3%), HR-/HER2+ (82.7%), and finally worst survival for triple-negative subtype (77.0%) [25].

ILC is generally associated with a good prognosis and a good response to endocrine therapy.

Role of PET/CT Imaging in Breast Cancer

FDG PET and NaF PET

Initial Staging

Per NCCN, FDG PET/CT (FDG PET) is not indicated in the staging of early breast cancer [clinical stage I, II and operable stage III (T3 N1 M0)[cases [10]. FDG PET is most helpful in situations where

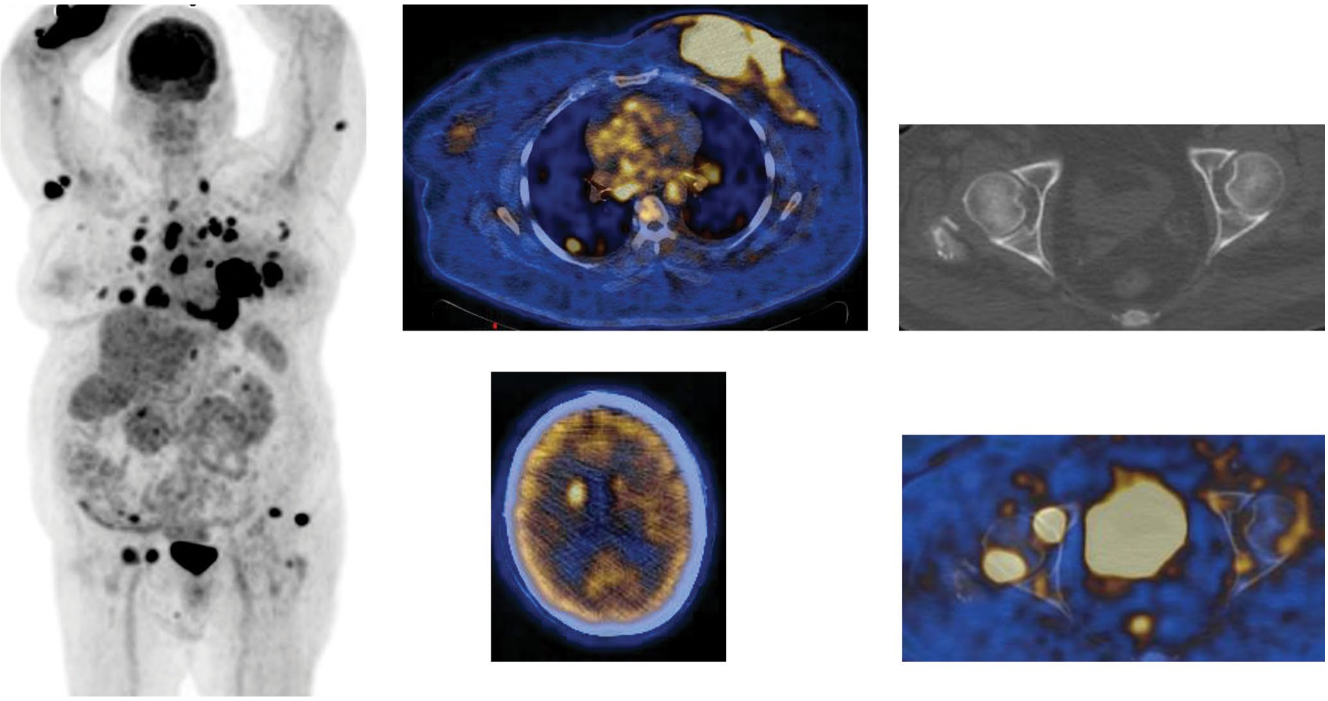

Figure 1. A 66-year-old female with newly diagnosed invasive ductal breast carcinoma. FDG PET/CT images show a large hypermetabolic (SUVmax 13.3) left breast mass invading the overlying skin and pectoralis muscle with multiple additional foci of activity within the breast and in the skin, multiple hypermetabolic lymph nodes in the left axilla, both side of the mediastinum, left supraclavicular and right retro-crural regions, multiple hypermetabolic lung nodules, multiple hypermetabolic bone lesions some with lytic changes and some without changes on CT, and a hypermetabolic focus adjacent to right caudate nucleus in the brain, all consistent with metastatic disease

standard staging studies are equivocal or suspicious for stage III and stage IV invasive breast cancer, and inflammatory breast cancer (Fig. 1) [10]. FDG PET may help identify the unsuspected regional nodal disease and/or distant metastasis in locally advanced breast cancer when used in addition to standard imaging studies [10]. FDG PET may be a useful adjunct to standard imaging of inflammatory breast cancer due to increased risk of lymph node and distant metastases [10]. Equivocal or suspicious sites identified on PET/CT should be biopsied. FDG PET/CT is not indicated in early breast cancer (Tl and T2 unifocal tumours with clinically negative lymph nodes). In early breast cancer, sentinel lymph node (SLN) biopsy with or without SLN scintigraphy is performed to determine the pN status. In the authors' recent study, a combined assessment of SLN SPECT/CT and FDG PET/CT images helped to determine FDG uptake particularly in the SLN [26]. However, due to the limited resolution of PET scanners in detecting small-sized tumours, this technique does not seem feasible currently but may be useful in the future with the improvement in PET resolution.

FDG uptake shows a correlation with the tumour grade, histological and molecular subtypes of breast cancer and various other factors. FDG uptake is higher in higher-grade tumours than lower grade tumours [27–29]. FDG uptake is higher in IDC than ILC histological subtype [27–29]. Inflammatory breast cancers show diffuse or focal high FDG uptake. Mean SUVmax of IDC was 7.7, which ranged from 2.1 to 18.8 [30]. FDG uptake is positively correlated with the tumour size, tumour cell proliferation (Ki67 expression), nuclear atypia, mitosis counts, tumour invasive size and lymph node metastasis [28, 29, 31–34]. FDG uptake is negatively correlated with the hormonal receptor status of the tumour [28, 31]. ER-, PR-, and triple-negative subtypes show higher FDG uptake than ER+, PR+, ER+PR+HER2+, or ER+PR+HER2- subtypes [28,29, 31, 35, 36]. FDG uptake was significantly higher in carcinomas with a high score of HER2 expression and high levels of p53 [27, 28].

DCIS usually show low FDG uptake but symptomatic and large DCIS (≥ 20 mm) are often visualized on FDG PET [37, 38]. Tumour cell density appears to be strongly correlated to the detection of DCIS by FDG PET [38]. FDG uptake is higher in DCIS with microinvasion than pure DCIS [36]. DCIS with micro invasions are larger, show poor prognostic factors (high grade, comedo necrosis and ER negativity), and have a worse outcome than pure DCIS [39, 40]. DCIS often coexists with IDC (IDC-DCIS) [41, 42]. DCIS is recognized as the non-obligate precursor of IDC when it coexists with IDC [43]. Studies have reported that IDC with coexisting DCIS shows lower metastatic potential and recurrence and better overall survival than pure IDC [44, 45]. In a recent study, FDG PET/CT findings of IDC-DCIS to pure IDC [30] were compared. Multifocal breast FDG uptake and the multifocal tumour was more common in IDC-DCIS than pure IDC but there was no significant difference in standardized uptake value (SUV) of the primary tumour in IDC-DCIS and pure IDC. However, axillary metastases appeared to be more common in pure IDC than IDC-DCIS cases. In an unpublished analysis of IDC-DCIS was found a positive correlation between primary tumour grade

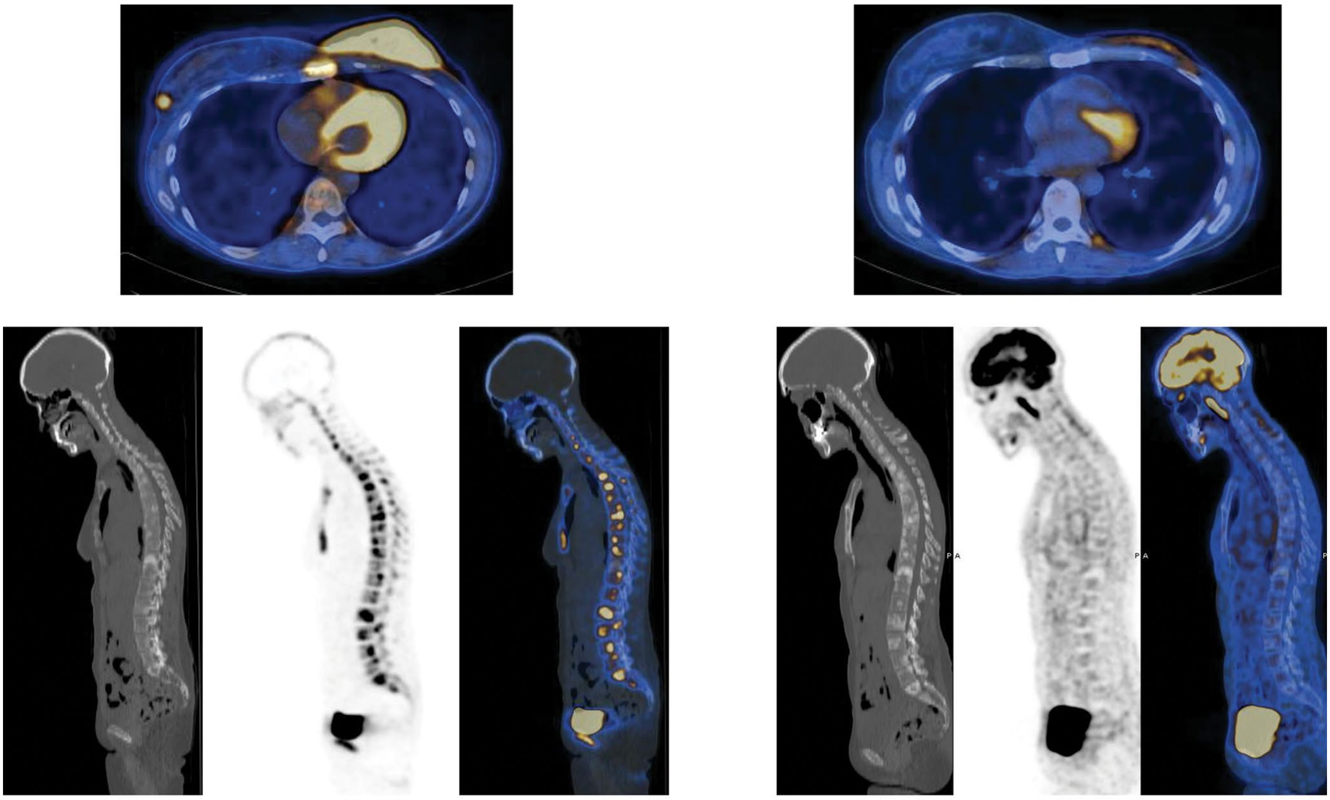

Before Chemotherapy

After Chemotherapy

Figure 2. FDG PET/CT images on hormone therapy with an aromatase inhibitor (before chemotherapy) and after treatment with a combination of aromatase inhibitor and chemotherapy (targeted therapy with an inhibitor of the cyclin-dependent kinases CDK4 and CDK6) (after chemotherapy) in a 41-year-old female with inflammatory breast cancer. PET images before chemotherapy show diffuse infiltration of the left breast with markedly increased metabolic activity and multiple lytic and hypermetabolic bone metastases. Note also a hypermetabolic focus in the right breast laterally. Following chemotherapy, there is a resolution of the primary tumour on both PET and CT images with only mild diffuse chest wall activity which is probably due to inflammatory changes although residual tumour cannot be excluded. There is also the resolution of hypermetabolic bone metastases and most of the lytic bone lesions become sclerotic after the treatment

and nuclear grade of the coexisting DCIS but no correlation between primary tumour SUV with the nuclear grade and the architectural subtype of the coexisting DCIS.

Bone-specific radiotracers are also known to accumulate in the breast tumours which may be due to hydroxyapatite deposition [46]. They have low sensitivity in detecting the primary tumour. In a recent study, the authors assessed NaF uptake in the primary breast tumours [47]. Fourteen of 31 IDC (45%) and 3 of 4 DCIS were visible on NaF PET and 5 ILC, 2 invasive mammary carcinomas, and 1 mucinous carcinoma were not visible. In the same study, there was no correlation between NaF SUV and FDG SUV of the primary tumours.

Bone is the most common site of distant metastasis in patients with breast cancer. Bone metastases of breast cancer are most often osteolytic but can be osteoblastic or mixed and sometimes may not show any changes in CT [48]. Radionuclide bone imaging has high sensitivity in detecting bone metastases and recommended in patients with bone pain or elevated alkaline phosphatase [10]. Radionuclide bone imaging can be omitted if FDG PET/CT is positive for bone metastases [10]. NaF PET/CT provides greater spatial resolution and better image quality, resulting in better sensitivity and specificity than bone scan. In a meta-analysis study, the pooled sensitivity, and specificity of NaF PET/CT for the detection of bone metastases were 0.98 and 0.90, respectively with a higher overall diagnostic performance over bone scan and bone SPECT [49]. Radionuclide bone imaging is more sensitive for the detection of sclerotic osseous metastases whereas FDG PET is more sensitive for the detection of lytic osseous metastases. In untreated patients, bone metastases of ILC were more commonly sclerotic and demonstrated low FDG uptake, whereas bone metastases of IDC were more commonly lytic and showed higher FDG uptake [50].

CT has higher sensitivity than PET and PET/MR in detecting pulmonary lesions, particularly subcentimetric lesions [51]. PET underestimates the metabolic activity of the subcentimetric lung nodules due to partial volume averaging. Small lung nodules located in the periphery of the lungs, particularly near the diaphragm, may also be affected by respiratory motion which causes misregistration of CT and PET images and sub-optimal attenuation correction with underestimation of metabolic activity of the nodules.

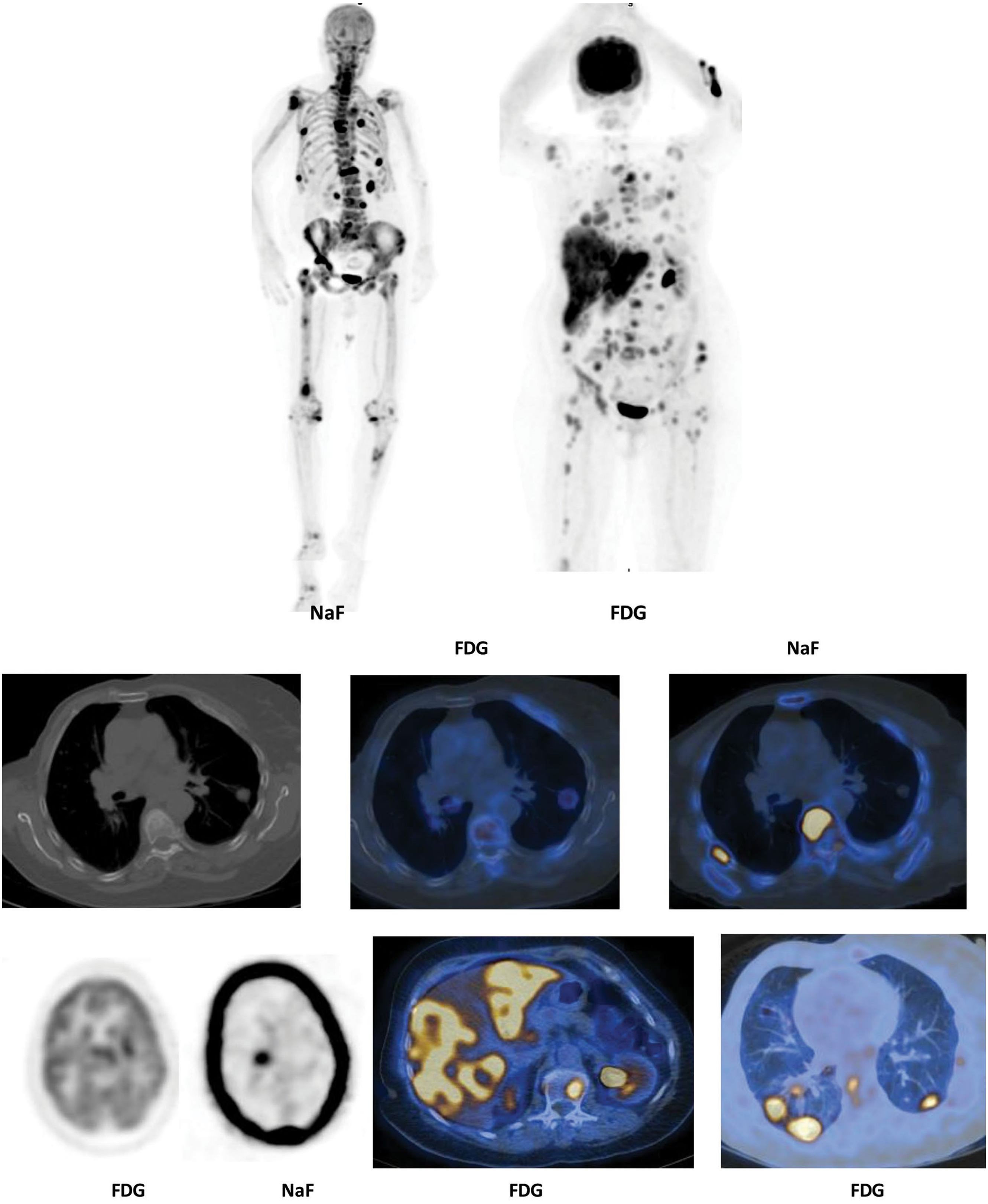

Figure 3. A 72-year-old female with a history of invasive ductal breast cancer operated and received chemotherapy 4 years before the PET scan. The patient has clinical symptoms and radiological findings highly suspicious for tumour recurrence. FDG PET/CT images show extensive metastatic disease in the liver and multiple foci of hypermetabolic bone metastases and multiple bilateral lung metastases. There is also reduced uptake in the right thalamus posteriorly and increased uptake adjacent to left caudate, highly suspicious for metastases. NaF PET images show multiple bone metastases and focal uptake corresponding to the area of reduced uptake in right thalamus on FDG PET. Uptake pattern in the bone metastases is different on FDG and NaF PET images with NaF PET showing uptake in sclerotic lesions (arrow) whereas FDG PET in lytic lesions (not shown in the figure)

In autopsy studies, brain metastases were present in 15% to 35% of patients with breast cancer, and some of them were asymptomatic before death [52]. Due to high FDG uptake in the grey matter of the brain and low metabolic activity of some of the brain metastases of breast cancer, the sensitivity of FDG PET is lower than diagnostic CT, MRI and PET/MR [53–55]. Cerebellum and frontal lobes are reported to be the most common sites of metastasis [56] Breast cancer metastasis in the brain could be hypermetabolic, ring-like or hypometabolic [54, 55].

Liver metastases develop in approximately 50% of patients with breast cancer [57]. MRI and PET/MR has higher sensitivity than diagnostic CT and FDG PET/CT in detecting small liver metastases [53, 58, 59]. Breast carcinoma metastases are generally hypo-vascular, but occasionally they can be hyper-vascular on contrast-enhanced MRI [60]. Background liver activity on FDG PET may reduce the detection of small metastatic foci. Dual time point FDG PET imaging may increase the detection of liver metastases of breast cancer [61].

Assessing Response to Treatment

PET/CT imaging is very useful for prediction of treatment response as early as after the first cycle of chemotherapy and after completion of chemotherapy (Fig. 2).

Studies have shown that FDG PET imaging early in the course of the chemotherapy helps to differentiate responders from non-responders [62–66]. A reduction in tumour FDG uptake supports the efficiency of the treatment whereas no change or further increase in tumour FDG uptake indicates that the treatment is ineffective.

To assess early treatment response, a period of 1 ± 2 weeks between completion of the chemotherapy cycle and FDG PET scan is recommended to avoid transient increases and decreases in tumour FDG uptake [67]. To assess the complete treatment response, International Harmonization Project (IHP) recommends waiting 6–8 weeks after the last cycle of chemotherapy [68].

Positron Emission Tomography (PET) Response Criteria in Solid Tumours (PERCIST) recommends a ≥ 30% decrease in tumour SUV as compared to baseline PET study as a cut-off value for partial metabolic response in solid tumours [69].

Definition of FDG tumour response in malignancies by European Organisation for Research and Treatment of Cancer (EORTC) [67]:

Progressive metabolic disease: Increase in tumour SUV greater than 25% and visible increase in the size of the tumour (> 20% in longest diameter) and appearance of new lesions as compared to baseline FDG PET scan.

Stable metabolic disease: Decrease in tumour SUV less than 15% or increase in tumour SUV less than 25% and no visible change in tumour size.

Partial Metabolic Response: A reduction of minimum 15–25% in tumour SUV after 1 cycle of treatment and greater than 25% after more cycles of treatment.

Complete response: Complete resolution of tumour FDG uptake so that it was indistinguishable from surrounding normal tissue.

Currently, there is not an effective study for accurate assessment of response to therapy of bone metastases of breast cancer. Lytic lesions usually become sclerotic after systemic treatment. Non-FDG avid sclerotic lesions may represent treated metastasis and healing response rather than the active tumour. Several studies have suggested that a change in SUV on FDG PET can predict disease response or progression. In a study of sequential FDG PET/CT imaging for monitoring bone metastasis of breast cancer during therapy, an increase in FDG uptake was correlated with lytic changes on the CT images and indicated progression of the disease [70]. However, early metabolic flare can also be seen with FDG PET. Increase in FDG uptake was observed 7–10 days after initiation of tamoxifen therapy in the majority of the metastatic bone lesions of the breast cancer responders [71]. Flare phenomenon is a significant problem in radionuclide bone imaging studies with temporary increases in activity and size of lesions or appearance of new lesions. To avoid misinterpretation of the flare reaction it is recommended to wait 6 months before evaluating the response, by MD Anderson criteria, or repeating the study [72]. Due to long waiting time, radionuclide bone imaging is not useful in early response assessment to treatments. It is also not useful in lytic or diffuse sclerotic (super scan) disease when assessing response to treatment [72]. Per EORTC, whole body or axial skeleton, MRI offers the best single modality of assessing response to therapy in bone metastases from breast cancer [72]. MRI is also not affected by flare response and has a potential for early response assessment to treatments [73]. As the changes in bone lesions are often difficult to assess on plain or cross-sectional radiology or radionuclide bone imaging, clinical symptoms and serum tumour markers (e.g., CEA, CA15-3, CA27.29) can help to determine if there is disease progression in bone-dominant metastatic disease [10].

Detecting Tumour Recurrence

Various factors affect breast cancer recurrence. Tumour size larger than 2 cm, axillary lymph node involvement, negative oestrogen and progesterone receptor status, and high tumour grade is associated with increased risk of loco-regional recurrence and metastases [74]. Breast cancer recurrence rate is approximately 30%, depending on the initial extent of the tumour and various other factors [75].

Studies have shown that FDG PET/CT imaging is superior to conventional imaging in detecting breast cancer recurrence (Figure 3). In breast cancer patients with rising Ca 15-3 tumour marker with negative conventional imaging, FDG PET/CT detected tumour deposits in 40 of 89 patients, in the chest wall, internal mammary nodes, lungs, liver and skeleton [76]. The sensitivity and specificity of FDG PET and conventional modalities were 84% and 78% versus 63% and 61%, respectively, in breast cancer patients with suspicion of recurrence [77]. In patients with confirmed breast cancer recurrence, conventional imaging was positive in 88% of the cases, whereas FDG PET/CT was positive in 95% [78]. FDG PET/CT had also a higher negative predictive value (86% versus 54%) and positive predictive value (95% versus 70%) than conventional imaging in the same study. In another study, FDG PET/CT was better than conventional imaging in detecting locoregional disease or distant metastases in breast cancer patients suspected of tumour recurrence [79]. In a study comparing FDG PET/CT to whole-body MRI, PET/CT detected more lymph node metastases (21 vs 16) whereas whole-body MRI was more precise in the detection of distant metastases (154 vs 147) [80].

However, a meta-analysis study showed that mediastinal and loco-regional lymph nodes represented the most common site for false-positive FDG PET/CT [81]. In 17 patients with breast cancer recurrence, FDG PET/MR and FDG PET/CT were positive in all patients with slightly more lesions detected by FDG PET/MR [82]. Per NCCN recommendation, FDG PET/CT can be performed at the same time as diagnostic CT and is most helpful in situations where standard studies are equivocal or suspicious [10].

Predicting Prognosis and Survival

Studies have shown that baseline FDG PET imaging has a prognostic value. Tumours with high SUV showed higher relapse and mortality rate compared to those with low SUV [28]. In ER+/HER2- M0 patients, tumour SUV and total lesion glycolysis were associated with shorter event-free survival [83]. Three-year event-free survival was 49% in patients with tumour SUV of 10 versus 92% in patients with tumour SUV $<$ 10 [83]. FDG-PET determined parameters (maximum SUV, peak SUV and total lesion glycolysis) appeared to provide prognostic survival information in patients with recurrent breast cancer [84]. In patients with low and high metabolic tumour volume, 5-year progression-free survival was 81.0 and 14.3%, and 5-year overall survival was 88.5% and 43.6%, respectively [85].

Other PET Tracers

ER expression is associated with a more favourable prognosis in breast cancer. ER status of the tumour predicts the likelihood of response to ER-targeted therapy [86]. ^{18}F-fluoroestradiol is an investigational PET tracer which binds to ER receptors. FES PET helps to determine the presence and amount of ER expression and predicts response to hormone therapy [87]. FES uptake is influenced by the site of metastasis. FES uptake in bone metastases was higher than in lymph node and lung metastases [88]. As the FES is highly extracted and metabolized by the liver, FES PET may have low sensitivity in detecting liver metastases. Studies suggest that up to 30% of patients may lose ER expression after undergoing endocrine therapy.

Approximately 20% of invasive ductal breast malignancies are classified as HER2-positive [89]. HER2+ breast cancer receives specific targeted HER2 therapies (humanized mAbs against HER2). ^{89}Zr-trastuzumab (radiolabelled herceptin) binds with high affinity to the extracellular domain of the HER2 receptor. In a clinical trial, ^{89}Zr-trastuzumab showed excellent tumour uptake and visualization of HER2-positive metastatic lesions [90].

18F-Fluorothymidine (FLT) is a biomarker reflecting cell proliferation. There is a good correlation between the FLT uptake and the Ki-67 labelling index in breast cancer [91]. FLT PET seems to be a good predictor of response to treatment, particularly early response [92].

There are various other potential PET radiotracers such as ^{18}F-galacto-RGD for angiogenesis, ^{18}F-annexin V for apoptosis, ^{89}Zr-anti-gH2AX-TAT for cell death, and ^{18}F-FMISO for hypoxia. RGD PET parameters were found to be significantly higher in HER2-positive patients [93]. RGD PET identified all invasive carcinomas, with SUVs ranging from 1.4 to 8.7 [94]. Lymph-node metastases were detected in 3 of 8 patients and SUVs in distant metastases were heterogeneous [94]. FMISO PET/CT was found to be useful for predicting primary endocrine resistance in ER+ breast cancer [95].

It was reported that 60% of breast cancer cases exhibited PSMA-positive endothelia with higher expression rates in the higher grade, NST subtype, HER2 +, and hormone receptor-negative tumours [96]. ^{68}Ga-PSMA ligand uptake was reported in primary breast tumour and its metastases [97]. In 19 patients with breast cancer, there was PSMA uptake in 84% of tumour lesions with higher uptake in distant metastases than primary or local recurrence [98].

Conclusion

Breast cancer is the most common cancer among women and also one of the most common indications of PET imaging. FDG and NaF are commonly used PET tracers in breast cancer mainly for initial staging, treatment response assessment and in detecting tumour recurrence. Various other more specific PET tracers targeting ER, HER2, cell proliferation, angiogenesis, cell death, apoptosis and hypoxia are at investigational level.

References

1. World Health Organization (2019). Breast cancer: Early diagnosis and screening. https://www.who.int/cancer/ prevention/diagnosis-screening/breast-cancer/en/ (18.04.2019).
2. American Cancer Society. Definitions. 2020, doi: 10.32388/w3jpuc.
3. Guinebretière JM, Menet E, Tardivon A, et al. Normal and pathological breast, the histological basis. Eur J Radiol. 2005; 54(1): 6–14, doi: 10.1016/j.ejrad.2004.11.020, indexed in Pubmed: 15797289.
4. Suami H, Pan WR, Mann GB, et al. The lymphatic anatomy of the breast and its implications for sentinel lymph node biopsy: a human cadaver study. Ann Surg Oncol. 2008; 15(3): 863–871, doi: 10.1245/s10434-007-9709-9, indexed in Pubmed: 18043970.
5. Urban JA. Management of operable breast cancer: the surgeon's view. Cancer. 1978; 42(4): 2066–2077, doi: 10.1002/1097-0142(197810)42:4<2066::aid-cncr2820420458>3.0.co;2-v, indexed in Pubmed: 101302.
6. Elmadahm AA, Gill PG, Bochner M, et al. Mammary lymphoscintigraphy in breast cancer. J Nucl Med. 1995; 36(10): 1775–1780, indexed in Pubmed: 7562041.
7. Oeffinger K, Fontham E, Etzioni R, et al. Breast Cancer Screening for Women at Average Risk. JAMA. 2015; 314(15): 1599, doi: 10.1001/jama.2015.12783.
8. Gülsün M, Demirkazik FB, Ariyürek M. Evaluation of breast microcalcifications according to Breast Imaging Reporting and Data System criteria and Le Gal's classification. Eur J Radiol. 2003; 47(3): 227–231, doi: 10.1016/s0720-048x(02)00181-x, indexed in Pubmed: 12927667.
9. AJCC Cancer Staging Manual, Eighth Edition © The American College of Surgeons (ACS), Chicago, Illinois. Last updated 01. ; 25: 2018.
10. NCCN Clinical Practice Guidelines in Oncology (NCCN Guidelines). National Comprehensive Cancer Network. Version 4 2017-February. ; 7: 2018.
11. Arps DP, Healy P, Zhao L, et al. Invasive ductal carcinoma with lobular features: a comparison study to invasive ductal and invasive lobular carcinomas of the breast. Breast Cancer Res Treat. 2013; 138(3): 719–726, doi: 10.1007/s10549-013-2493-2, indexed in Pubmed: 23535842.
12. Malhotra GK, Zhao X, Band H, et al. Histological, molecular and functional subtypes of breast cancers. Cancer Biol Ther. 2010; 10(10): 955–960, doi: 10.4161/cbt.10.10.13879, indexed in Pubmed: 21057215.
13. Dawood S, Merajver SD, Viens P, et al. International expert panel on inflammatory breast cancer: consensus statement for standardized diagnosis and treatment. Ann Oncol. 2011; 22(3): 515–523, doi: 10.1093/annonc/mdq345, indexed in Pubmed: 20603440.
14. McCart Reed AE, Kutasovic JR, Lakhani SR, et al. Invasive lobular carcinoma of the breast: morphology, biomarkers and 'omics. Breast Cancer Res. 2015; 17: 12, doi: 10.1186/s13058-015-0519-x, indexed in Pubmed: 25849106.

15. Dunnwald L, Rossing M, Li C. Hormone receptor status, tumor characteristics, and prognosis: a prospective cohort of breast cancer patients. Breast Cancer Research. 2007; 9(1), doi: 10.1186/bcr1639.
16. Dai X, Xiang L, Li T, et al. Cancer Hallmarks, Biomarkers and Breast Cancer Molecular Subtypes. J Cancer. 2016; 7(10): 1281–1294, doi: 10.7150/jca.13141, indexed in Pubmed: 27390604.
17. Duffy MJ, Synnott NC, Crown J. Mutant p53 in breast cancer: potential as a therapeutic target and biomarker. Breast Cancer Res Treat. 2018; 170(2): 213–219, doi: 10.1007/s10549-018-4753-7, indexed in Pubmed: 29564741.
18. Langley RR, Fidler IJ. The seed and soil hypothesis revisited--the role of tumor-stroma interactions in metastasis to different organs. Int J Cancer. 2011; 128(11): 2527–2535, doi: 10.1002/ijc.26031, indexed in Pubmed: 21365651.
19. Xiao W, Zheng S, Yang A, et al. Breast cancer subtypes and the risk of distant metastasis at initial diagnosis: a population-based study. Cancer Manag Res. 2018; 10: 5329–5338, doi: 10.2147/CMAR.S176763, indexed in Pubmed: 30464629.
20. Soni A, Ren Z, Hameed O, et al. Breast cancer subtypes predispose the site of distant metastases. Am J Clin Pathol. 2015; 143(4): 471–478, doi: 10.1309/AJCPYO5FSV3UPEXS, indexed in Pubmed: 25779997.
21. Smid M, Wang Y, Zhang Yi, et al. Subtypes of breast cancer show preferential site of relapse. Cancer Res. 2008; 68(9): 3108–3114, doi: 10.1158/0008-5472.CAN-07-5644, indexed in Pubmed: 18451135.
22. Gerratana L, Fanotto V, Bonotto M, et al. Pattern of metastasis and outcome in patients with breast cancer. Clin Exp Metastasis. 2015; 32(2): 125–133, doi: 10.1007/s10585-015-9697-2, indexed in Pubmed: 25630269.
23. Mathew A, Rajagopal PS, Villgran V, et al. Distinct Pattern of Metastases in Patients with Invasive Lobular Carcinoma of the Breast. Geburtshilfe Frauenheilkd. 2017; 77(6): 660–666, doi: 10.1055/s-0043-109374, indexed in Pubmed: 28757653.
24. Borst MJ, Ingold JA. Metastatic patterns of invasive lobular versus invasive ductal carcinoma of the breast. Surgery. 1993; 114(4): 637–41; discussion 641, indexed in Pubmed: 8211676.
25. Howlader N, Cronin KA, Kurian AW, et al. Differences in Breast Cancer Survival by Molecular Subtypes in the United States. Cancer Epidemiol Biomarkers Prev. 2018; 27(6): 619–626, doi: 10.1158/1055-9965.EPI-17-0627, indexed in Pubmed: 29593010.
26. Sarikaya I, Sarikaya A. Assessing F-FDG Uptake in the Sentinel Lymph Node in Breast Cancer. J Nucl Med Technol. 2019; 47(2): 149–153, doi: 10.2967/jnmt.118.219758, indexed in Pubmed: 30413593.
27. Crippa F, Seregni E, Agresti R, et al. Association between [18F]fluorodeoxyglucose uptake and postoperative histopathology, hormone receptor status, thymidine labelling index and p53 in primary breast cancer: a preliminary observation. Eur J Nucl Med. 1998; 25(10): 1429–1434, doi: 10.1007/s002590050319, indexed in Pubmed: 9818284.
28. Ueda S, Tsuda H, Asakawa H, et al. Clinicopathological and prognostic relevance of uptake level using 18F-fluorodeoxyglucose positron emission tomography/computed tomography fusion imaging (18F-FDG PET/CT) in primary breast cancer. Jpn J Clin Oncol. 2008; 38(4): 250–258, doi: 10.1093/jjco/hyn019, indexed in Pubmed: 18407934.
29. Wang CL, MacDonald LR, Rogers JV, et al. Positron emission mammography: correlation of estrogen receptor, progesterone receptor, and human epidermal growth factor receptor 2 status and 18F-FDG. AJR Am J Roentgenol. 2011; 197(2): W247–W255, doi: 10.2214/AJR.11.6478, indexed in Pubmed: 21785049.
30. Sarikaya I, Sarikaya A, Albatineh AN, et al. Is there a difference in FDG PET findings of invasive ductal carcinoma of the breast with and without coexisting DCIS? Asia Ocean J Nucl Med Biol. 2020; 8: 27–35.
31. Jo I, Zeon SK, Kim SH, et al. Correlation of Primary Tumor FDG Uptake with Clinicopathologic Prognostic Factors in Invasive Ductal Carcinoma of the Breast. Nucl Med Mol Imaging. 2015; 49(1): 19–25, doi: 10.1007/s13139-014-0296-y, indexed in Pubmed: 25774234.
32. Kim JY, Lee SH, Kim S, et al. Tumour 18 F-FDG Uptake on preoperative PET/CT may predict axillary lymph node metastasis in ER-positive/HER2-negative and HER2-positive breast cancer subtypes. Eur Radiol. 2015; 25(4): 1172–1181, doi: 10.1007/s00330-014-3452-y, indexed in Pubmed: 25298170.
33. Ege Aktas G, Taştekin E, Sarikaya A. Assessment of biological and clinical aggressiveness of invasive ductal breast cancer using baseline 18F-FDG PET/CT-derived volumetric parameters. Nucl Med Commun. 2018; 39(1): 83–93, doi: 10.1097/MNM.0000000000000779, indexed in Pubmed: 29135722.
34. Gil-Rendo A, Martínez-Regueira F, Zornoza G, et al. Association between [18F]fluorodeoxyglucose uptake and prognostic parameters in breast cancer. Br J Surg. 2009; 96(2): 166–170, doi: 10.1002/bjs.6459, indexed in Pubmed: 19160365.
35. Groheux D, Giacchetti S, Moretti JL, et al. Correlation of high 18F-FDG uptake to clinical, pathological and biological prognostic factors in breast cancer. Eur J Nucl Med Mol Imaging. 2011; 38(3): 426–435, doi: 10.1007/s00259-010-1640-9, indexed in Pubmed: 21057787.
36. Yoon HJ, Kim Y, Kim BS. Intratumoral metabolic heterogeneity predicts invasive components in breast ductal carcinoma in situ. Eur Radiol. 2015; 25(12): 3648–3658, doi: 10.1007/s00330-015-3761-9, indexed in Pubmed: 26063655.
37. Avril N, Menzel M, Dose J, et al. Glucose metabolism of breast cancer assessed by 18F-FDG PET: histologic and immunohistochemical tissue analysis. J Nucl Med. 2001; 42(1): 9–16, indexed in Pubmed: 11197987.
38. Fujioka T, Kubota K, Toriihara A, et al. Tumor characteristics of ductal carcinoma in situ of breast visualized on [F-18] fluorodeoxyglucose-positron emission tomography/computed tomography: Results from a retrospective study. World J Radiol. 2016; 8(8): 743–749, doi: 10.4329/wjr.v8.i8.743, indexed in Pubmed: 27648168.
39. de Mascarel I, MacGrogan G, Mathoulin-Pélissier S, et al. Breast ductal carcinoma in situ with microinvasion: a definition supported by a long-term study of 1248 serially sectioned ductal carcinomas. Cancer. 2002; 94(8): 2134–2142, doi: 10.1002/cncr.10451, indexed in Pubmed: 12001109.
40. Yu KD, Wu LM, Liu GY, et al. Different distribution of breast cancer subtypes in breast ductal carcinoma in situ (DCIS), DCIS with microinvasion, and DCIS with invasion component. Ann Surg Oncol. 2011; 18(5): 1342–1348, doi: 10.1245/s10434-010-1407-3, indexed in Pubmed: 21042943.
41. Jo BH, Chun YK. Heterogeneity of invasive ductal carcinoma: proposal for a hypothetical classification. J Korean Med Sci. 2006; 21(3): 460–468, doi: 10.3346/jkms.2006.21.3.460, indexed in Pubmed: 16778390.
42. Logullo AF, Godoy AB, Mourão-Neto M, et al. Presence of ductal carcinoma in situ confers an improved prognosis for patients with T1N0M0 invasive breast carcinoma. Braz J Med Biol Res. 2002; 35(8): 913–919, doi: 10.1590/s0100-879x2002000800008, indexed in Pubmed: 12185383.
43. Pinder SE, Ellis IO. The diagnosis and management of pre-invasive breast disease: ductal carcinoma in situ (DCIS) and atypical ductal hyperplasia (ADH)--current definitions and classification. Breast Cancer Res. 2003; 5(5): 254–257, doi: 10.1186/bcr623, indexed in Pubmed: 12927035.
44. Dieterich M, Hartwig F, Stubert J, et al. Accompanying DCIS in breast cancer patients with invasive ductal carcinoma is predictive of improved local recurrence-free survival. Breast. 2014; 23(4): 346–351, doi: 10.1016/j.breast.2014.01.015, indexed in Pubmed: 24559611.
45. Wong H, Lau S, Yau T, et al. Presence of an in situ component is associated with reduced biological aggressiveness of size-matched invasive breast cancer. Br J Cancer. 2010; 102: 1391–6.
46. Berg G, Kalisher L, Osmond J, et al. 99mTc-Diphosphonate Concentration in Primary Breast Carcinoma. Radiology. 1973; 109(2): 393–394, doi: 10.1148/109.2.393.
47. Sarikaya I, Sharma P, Sarikaya A. F-18 fluoride uptake in primary breast cancer. Ann Nucl Med. 2018; 32(10): 678–686, doi: 10.1007/s12149-018-1294-4, indexed in Pubmed: 30178199.
48. Kozlow W, Guise TA. Breast cancer metastasis to bone: mechanisms of osteolysis and implications for therapy. J Mammary Gland Biol Neoplasia.

2005; 10(2): 169–180, doi: 10.1007/s10911-005-5399-8, indexed in Pubmed: 16025223.

49. Sheikhbahaei S, Jones KM, Werner RA, et al. F-NaF-PET/CT for the detection of bone metastasis in prostate cancer: a meta-analysis of diagnostic accuracy studies. Ann Nucl Med. 2019; 33(5): 351–361, doi: 10.1007/s12149-019-01343-y, indexed in Pubmed: 30877561.
50. Dashevsky BZ, Goldman DA, Parsons M, et al. Appearance of untreated bone metastases from breast cancer on FDG PET/CT: importance of histologic subtype. Eur J Nucl Med Mol Imaging. 2015; 42(11): 1666–1673, doi: 10.1007/s00259-015-3080-z, indexed in Pubmed: 25971426.
51. Rauscher I, Eiber M, Fürst S, et al. PET/MR imaging in the detection and characterization of pulmonary lesions: technical and diagnostic evaluation in comparison to PET/CT. J Nucl Med. 2014; 55(5): 724–729, doi: 10.2967/jnumed.113.129247, indexed in Pubmed: 24652827.
52. Martin AM, Cagney DN, Catalano PJ, et al. Brain Metastases in Newly Diagnosed Breast Cancer: A Population-Based Study. JAMA Oncol. 2017; 3(8): 1069–1077, doi: 10.1001/jamaoncol.2017.0001, indexed in Pubmed: 28301662.
53. Gaeta CM, Vercher-Conejero JL, Sher AC, et al. Recurrent and metastatic breast cancer PET, PET/CT, PET/MRI: FDG and new biomarkers. Q J Nucl Med Mol Imaging. 2013; 57(4): 352–366, indexed in Pubmed: 24322792.
54. Bochev P, Klisarova A, Kaprelyan A, et al. Brain metastases detectability of routine whole body (18)F-FDG PET and low dose CT scanning in 2502 asymptomatic patients with solid extracranial tumors. Hell J Nucl Med. 2012; 15(2): 125–129, doi: 10.1967/s002449910030, indexed in Pubmed: 22741148.
55. Kitajima K, Nakamoto Y, Okizuka H, et al. Accuracy of whole-body FDG-PET/CT for detecting brain metastases from non-central nervous system tumors. Ann Nucl Med. 2008; 22(7): 595–602, doi: 10.1007/s12149-008-0145-0, indexed in Pubmed: 18756362.
56. Rostami R, Mittal S, Rostami P, et al. Brain metastasis in breast cancer: a comprehensive literature review. J Neurooncol. 2016; 127(3): 407–414, doi: 10.1007/s11060-016-2075-3, indexed in Pubmed: 26909695.
57. He ZY, Wu SG, Peng F, et al. Up-Regulation of RFC3 Promotes Triple Negative Breast Cancer Metastasis and is Associated With Poor Prognosis Via EMT. Transl Oncol. 2017; 10(1): 1–9, doi: 10.1016/j.tranon.2016.10.004, indexed in Pubmed: 27888707.
58. Patterson SA, Khalil HI, Panicek DM, et al. Hepatic lesions deemed too small to characterize at CT: prevalence and importance in women with breast cancer. Radiology. 2005; 235(3): 872–878, doi: 10.1148/radiol.2353041099, indexed in Pubmed: 15833992.
59. Melsaether AN, Raad RA, Pujara AC, et al. Comparison of Whole-Body (18)F FDG PET/MR Imaging and Whole-Body (18)F FDG PET/CT in Terms of Lesion Detection and Radiation Dose in Patients with Breast Cancer. Radiology. 2016; 281(1): 193–202, doi: 10.1148/radiol.2016151155, indexed in Pubmed: 27023002.
60. Namasivayam S, Martin DR, Saini S. Imaging of liver metastases: MRI. Cancer Imaging. 2007; 7: 2–9, doi: 10.1102/1470-7330.2007.0002, indexed in Pubmed: 17293303.
61. Annovazzi A, Rea S, Vici P, et al. Dual-time 18F-FDG PET/CT for the detection of liver metastases in breast cancer. Nucl Med Commun. 2018; 39(12): 1183–1189, doi: 10.1097/MNM.0000000000000918, indexed in Pubmed: 30216230.
62. Wahl RL, Zasadny K, Helvie M, et al. Metabolic monitoring of breast cancer chemohormonotherapy using positron emission tomography: initial evaluation. J Clin Oncol. 1993; 11(11): 2101–2111, doi: 10.1200/JCO.1993.11.11.2101, indexed in Pubmed: 8229124.
63. Schelling M, Avril N, Nährig J, et al. Positron emission tomography using [(18)F]Fluorodeoxyglucose for monitoring primary chemotherapy in breast cancer. J Clin Oncol. 2000; 18(8): 1689–1695, doi: 10.1200/JCO.2000.18.8.1689, indexed in Pubmed: 10764429.
64. Smith IC, Welch AE, Hutcheon AW, et al. Positron emission tomography using [(18)F]-fluorodeoxy-D-glucose to predict the pathologic response of breast cancer to primary chemotherapy. J Clin Oncol. 2000; 18(8): 1676–1688, doi: 10.1200/JCO.2000.18.8.1676, indexed in Pubmed: 10764428.
65. Rousseau C, Devillers A, Sagan C, et al. Monitoring of early response to neoadjuvant chemotherapy in stage II and III breast cancer by [18F]fluorodeoxyglucose positron emission tomography. J Clin Oncol. 2006; 24(34): 5366–5372, doi: 10.1200/JCO.2006.05.7406, indexed in Pubmed: 17088570.
66. Schwarz-Dose J, Untch M, Tiling R, et al. Monitoring primary systemic therapy of large and locally advanced breast cancer by using sequential positron emission tomography imaging with [18F]fluorodeoxyglucose. J Clin Oncol. 2009; 27(4): 535–541, doi: 10.1200/JCO.2008.17.2650, indexed in Pubmed: 19075273.
67. Young H, Baum R, Cremerius U, et al. Measurement of clinical and subclinical tumour response using [18F]-fluorodeoxyglucose and positron emission tomography: review and 1999 EORTC recommendations. European Journal of Cancer. 1999; 35(13): 1773–1782, doi: 10.1016/s0959-8049(99)00229-4.
68. Juweid ME, Stroobants S, Hoekstra OS, et al. Imaging Subcommittee of International Harmonization Project in Lymphoma. Use of positron emission tomography for response assessment of lymphoma: consensus of the Imaging Subcommittee of International Harmonization Project in Lymphoma. J Clin Oncol. 2007; 25(5): 571–578, doi: 10.1200/JCO.2006.08.2305, indexed in Pubmed: 17242397.
69. Wahl RL, Jacene H, Kasamon Y, et al. From RECIST to PERCIST: Evolving Considerations for PET Response Criteria in Solid Tumors. Journal of Nuclear Medicine. 2009; 50(Suppl_1), doi: 10.2967/jnumed.108.057307.
70. Katayama T, Kubota K, Machida Y, et al. Evaluation of sequential FDG-PET/CT for monitoring bone metastasis of breast cancer during therapy: correlation between morphological and metabolic changes with tumor markers. Ann Nucl Med. 2012; 26(5): 426–435, doi: 10.1007/s12149-012-0595-2, indexed in Pubmed: 22477261.
71. Mortimer JE, Dehdashti F, Siegel BA, et al. Metabolic flare: indicator of hormone responsiveness in advanced breast cancer. J Clin Oncol. 2001; 19(11): 2797–2803, doi: 10.1200/JCO.2001.19.11.2797, indexed in Pubmed: 11387350.
72. Lecouvet FE, Talbot JN, Messiou C, et al. EORTC Imaging Group. Monitoring the response of bone metastases to treatment with Magnetic Resonance Imaging and nuclear medicine techniques: a review and position statement by the European Organisation for Research and Treatment of Cancer imaging group. Eur J Cancer. 2014; 50(15): 2519–2531, doi: 10.1016/j.ejca.2014.07.002, indexed in Pubmed: 25139492.
73. Padhani AR, Gogbashian A. Bony metastases: assessing response to therapy with whole-body diffusion MRI. Cancer Imaging. 2011; 11(1A): S129–S154, doi: 10.1102/1470-7330.2011.9034.
74. Lafourcade A, His M, Baglietto L, et al. Factors associated with breast cancer recurrences or mortality and dynamic prediction of death using history of cancer recurrences: the French E3N cohort. BMC Cancer. 2018; 18(1): 171, doi: 10.1186/s12885-018-4076-4, indexed in Pubmed: 29426294.
75. van Dongen JA, Voogd AC, Fentiman IS, et al. Long-term results of a randomized trial comparing breast-conserving therapy with mastectomy: European Organization for Research and Treatment of Cancer 10801 trial. J Natl Cancer Inst. 2000; 92(14): 1143–1150, doi: 10.1093/jnci/92.14.1143, indexed in Pubmed: 10904087.
76. Grassetto G, Fornasiero A, Otello D, et al. 18F-FDG-PET/CT in patients with breast cancer and rising Ca 15-3 with negative conventional imaging: a multicentre study. Eur J Radiol. 2011; 80(3): 828–833, doi: 10.1016/j.ejrad.2010.04.029, indexed in Pubmed: 20547020.
77. Grahek D, Montravers F, Kerrou K, et al. [18F]FDG in recurrent breast cancer: diagnostic performances, clinical impact and relevance of induced changes in management. Eur J Nucl Med Mol Imaging. 2004; 31(2): 179–188, doi: 10.1007/s00259-003-1348-1, indexed in Pubmed: 15129699.
78. Cochet A, David S, Moodie K, et al. The utility of 18 F-FDG PET/CT for suspected recurrent breast cancer: impact and prognostic stratification. Cancer Imaging. 2014; 14: 13, doi: 10.1186/1470-7330-14-13, indexed in Pubmed: 25608599.

79. Aukema TS, Rutgers EJ, Vogel WV, et al. The role of FDG PET/CT in patients with locoregional breast cancer recurrence: a comparison to conventional imaging techniques. Eur J Surg Oncol. 2010; 36(4): 387–392, doi: 10.1016/j.ejso.2009.11.009, indexed in Pubmed: 19962268.
80. Schmidt GP, Baur-Melnyk A, Haug A, et al. Comprehensive imaging of tumor recurrence in breast cancer patients using whole-body MRI at 1.5 and 3 T compared to FDG-PET-CT. Eur J Radiol. 2008; 65(1): 47–58, doi: 10.1016/j.ejrad.2007.10.021, indexed in Pubmed: 18082989.
81. Evangelista L, Baretta Z, Vinante L, et al. Tumour markers and FDG PET/CT for prediction of disease relapse in patients with breast cancer. Eur J Nucl Med Mol Imaging. 2011; 38(2): 293–301, doi: 10.1007/s00259-010-1626-7, indexed in Pubmed: 20882280.
82. Sawicki LM, Grueneisen J, Schaarschmidt BM, et al. Evaluation of ^{1} F-FDG PET/MRI, ^{1} F-FDG PET/CT, MRI, and CT in whole-body staging of recurrent breast cancer. Eur J Radiol. 2016; 85(2): 459–465, doi: 10.1016/j.ejrad.2015.12.010, indexed in Pubmed: 26781152.
83. Groheux D, Sanna A, Majdoub M, et al. Baseline Tumor 18F-FDG Uptake and Modifications After 2 Cycles of Neoadjuvant Chemotherapy Are Prognostic of Outcome in ER+/HER2- Breast Cancer. J Nucl Med. 2015; 56(6): 824–831, doi: 10.2967/jnumed.115.154138, indexed in Pubmed: 25883123.
84. Taghipour M, Wray R, Sheikhbahaei S, et al. FDG Avidity and Tumor Burden: Survival Outcomes for Patients With Recurrent Breast Cancer. AJR Am J Roentgenol. 2016; 206(4): 846–855, doi: 10.2214/AJR.15.15106, indexed in Pubmed: 27003053.
85. Chang CC, Chen CJ, Hsu WL, et al. Prognostic Significance of Metabolic Parameters and Textural Features on F-FDG PET/CT in Invasive Ductal Carcinoma of Breast. Sci Rep. 2019; 9(1): 10946, doi: 10.1038/s41598-019-46813-5, indexed in Pubmed: 31358786.
86. Davies C, Godwin J, Gray R, et al. Early Breast Cancer Trialists' Collaborative Group (EBCTCG). Relevance of breast cancer hormone receptors and other factors to the efficacy of adjuvant tamoxifen: patient-level meta-analysis of randomised trials. Lancet. 2011; 378(9793): 771–784, doi: 10.1016/S0140-6736(11)60993-8, indexed in Pubmed: 21802721.
87. Linden HM, Stekhova SA, Link JM, et al. Quantitative fluoroestradiol positron emission tomography imaging predicts response to endocrine treatment in breast cancer. J Clin Oncol. 2006; 24(18): 2793–2799, doi: 10.1200/JCO.2005.04.3810, indexed in Pubmed: 16682724.
88. Nienhuis HH, van Kruchten M, Elias SG, et al. F-Fluoroestradiol Tumor Uptake Is Heterogeneous and Influenced by Site of Metastasis in Breast Cancer Patients. J Nucl Med. 2018; 59(8): 1212–1218, doi: 10.2967/jnumed.117.198846, indexed in Pubmed: 29602822.
89. Slamon DJ, Clark GM, Wong SG, et al. Human breast cancer: correlation of relapse and survival with amplification of the HER-2/neu oncogene. Science. 1987; 235(4785): 177–182, doi: 10.1126/science.3798106, indexed in Pubmed: 3798106.
90. Dijkers EC, Oude Munnink TH, Kosterink JG, et al. Biodistribution of 89Zr-trastuzumab and PET imaging of HER2-positive lesions in patients with metastatic breast cancer. Clin Pharmacol Ther. 2010; 87(5): 586–592, doi: 10.1038/clpt.2010.12, indexed in Pubmed: 20357763.
91. Smyczek-Gargya B, Fersis N, Dittmann H, et al. PET with [18F]fluorothymidine for imaging of primary breast cancer: a pilot study. Eur J Nucl Med Mol Imaging. 2004; 31(5): 720–724, doi: 10.1007/s00259-004-1462-8, indexed in Pubmed: 14991243.
92. Contractor KB, Kenny LM, Stebbing J, et al. [18F]-3'Deoxy-3'-fluorothymidine positron emission tomography and breast cancer response to docetaxel. Clin Cancer Res. 2011; 17(24): 7664–7672, doi: 10.1158/1078-0432.CCR-11-0783, indexed in Pubmed: 22028493.
93. Yoon HJ, Kang KW, Chun InK, et al. Correlation of breast cancer subtypes, based on estrogen receptor, progesterone receptor, and HER2, with functional imaging parameters from Ga-RGD PET/CT and ^{1} F-FDG PET/CT. Eur J Nucl Med Mol Imaging. 2014; 41(8): 1534–1543, doi: 10.1007/s00259-014-2744-4, indexed in Pubmed: 24652232.
94. Beer AJ, Niemeyer M, Carlsen J, et al. Patterns of alphavbeta3 expression in primary and metastatic human breast cancer as shown by 18F-Galacto-RGD PET. J Nucl Med. 2008; 49(2): 255–259, doi: 10.2967/jnumed.107.045526, indexed in Pubmed: 18199623.
95. Cheng J, Lei Li, Xu J, et al. 18F-fluoromisonidazole PET/CT: a potential tool for predicting primary endocrine therapy resistance in breast cancer. J Nucl Med. 2013; 54(3): 333–340, doi: 10.2967/jnumed.112.111963, indexed in Pubmed: 23401605.
96. Tolkach Y, Gevensleben H, Bundschuh R, et al. Prostate-specific membrane antigen in breast cancer: a comprehensive evaluation of expression and a case report of radionuclide therapy. Breast Cancer Res Treat. 2018; 169(3): 447–455, doi: 10.1007/s10549-018-4717-y, indexed in Pubmed: 29455299.
97. Kumar R, Mittal BR, Bhattacharya A, et al. Synchronous Detection of Male Breast Cancer and Prostatic Cancer in a Patient With Suspected Prostatic Carcinoma on 68Ga-PSMA PET/CT Imaging. Clin Nucl Med. 2018; 43(6): 431–432, doi: 10.1097/RLU.0000000000002063, indexed in Pubmed: 29538032.
98. Sathekge M, Lengana T, Modiselle M, et al. Ga-PSMA-HBED-CC PET imaging in breast carcinoma patients. Eur J Nucl Med Mol Imaging. 2017; 44(4): 689–694, doi: 10.1007/s00259-016-3563-6, indexed in Pubmed: 27822700.

VIA MEDICA

Nuclear Medicine Review 2021, 24, 1: 27–28
DOI: 10.5603/NMR.2021.0005

ISSN 1506–9680

Clinical vignette

Findings in bone scintigraphy with [^{99m}Tc] Tc-MDP of a mandibular ameloblastic carcinoma

Liliana Patricia Torres[1], Marylin Acuña Hernandez[1], Tatiana Morales Avellaneda[1,2],
Andrés Ilich González Ramírez[1,2]
[1]Universidad AutóNoma De Bucaramanga, Santander, Colombia
[2]Spect Medicina Nuclear S.A.S, Centro medico carlos ardila Lulle, Bucaramanga, Colombia

[Received 6 V 2020; Accepted 6 X 2020]

KEY words: ameloblastic carcinoma, mandible, radionuclide imaging

Nucl Med Rev 2021; 24, 1: 27–28

Introduction

Ameloblastic carcinoma, a malignant odontogenic tumor that combines the histological characteristics of ameloblastoma with cytological atypia (OMS), is extremely rare and mainly affects men in the mandible and maxillary region (2/3 of cases) without a specific age.

Its etiology is unknown, although most cases are de novo and to a lesser extent develop from residual epithelial tissue to dental development such as ameloblastoma or odontogenic cyst.

The diagnosis is often difficult and is based on histopathological characteristics.

Clinical case

26-year-old man, in 2016 refers 3 years progressive growth in the right half of face indicating CT of the temporomandibular joint with evidence of odontogenic cyst that compromises the angle, ascending branch, mandibular condyle and right coronoid process of the mandible, drainage was performed.

By 2019 the lesion associated with pain and swallowing limitation reappears (Fig. 1). The CT sean of the temporomandibular joint where a predominantly cystic tumor mass with an over-aggregated lytic process is observed affecting the angle of the right side of the mandible as well as posterior dental structures of the lower jaw. The biopsy reported involvement of ameloblastic carcinoma with associated tumor necrosis.

Bone scintigraphy with SPECT and fusion image with CT scan as extension study is indicated, showing right mandibular lesion with peripheral increase uptake and low-uptake center, with no evidence of metastatic lesions (Figs. 2, 3 and 4).


[redacted]

Figure 1. Physical examination of the patient with evidence of a large mass in the right half of the face

Discussion

Ameloblastic carcinomas are usually aggressive entities with significant local involvement, recurrent and metastatic to cervical lymph nodes, lungs, bone, liver and brain [1, 3].

The diagnostic images allow an adequate initial staging prior to surgical treatment, allowing better planning [3, 4].

Correspondence to: Marylin Acuña Hernandez
Universidad AutóNoma De Bucaramanga, Ave. El No 23-60, Tms, CañAveral, Tv. El Bosque, 680003 Floridablanca, Santander, Colombia
e-mail: macuna766@unab.edu.co

Figure 2. Whole body bone scintigraphy shows an area of peripheral increase uptake and a low-uptake center can be seen in the right mandibular region, also to the right glenohumeral joint has an increase uptake that when interviewing the patient refers to trauma at this level being considered of inflammatory origin

CT or MRI allows to improve locoregional staging with the difficulty of evaluating disease at a distance; for this reason, in recent years have been used the 2- [^{18}F]-FDG PET/CT as a study for initial staging and monitoring, because hypermetabolism is found in the primary lesion and metastatic sites.

Bone scintigraphy with [^{99m}Tc] Tc-MDP allows the exclusion of metastatic bone lesions, especially when the primary tumor has an early spread. However, it has a limited role in lytic lesions that are reflected as photogenic areas which are associated with osteonecrosis, hypovascularity and aggressive tumor invasion.

References

1. Braimah R, Uguru C, Ndukwe K. Ameloblastic carcinoma of the jaws: Review of the literature. Journal of Dental and Allied Sciences. 2017; 6(2): 70, doi: 10.4103/jdas.jdas_4_17.
2. Pandey S, Bhutia O, Roychoudhury A, et al. Literature review of 86 cases of mandibular ameloblastic carcinoma. Natl J Maxillofac Surg. 2018; 9(1): 2–7, doi: 10.4103/njms.NJMS_33_16, indexed in Pubmed: 29937652.
3. Matsuzaki H, Katase N, Hara M, et al. Ameloblastic carcinoma: a case report with radiological features of computed tomography and magnetic resonance imaging and positron emission tomography. Oral Surg Oral Med Oral Pathol Oral Radiol Endod. 2011; 112(1): e40–e47, doi: 10.1016/j.tripleo.2011.01.023, indexed in Pubmed: 21458329.
4. Bahk YW, Bahk WJ. Malignant Tumors of Bone. Combined Scintigraphic and Radiographic Diagnosis of Bone and Joint Diseases. 2017: 407–450, doi: 10.1007/978-981-10-2759-8_17.

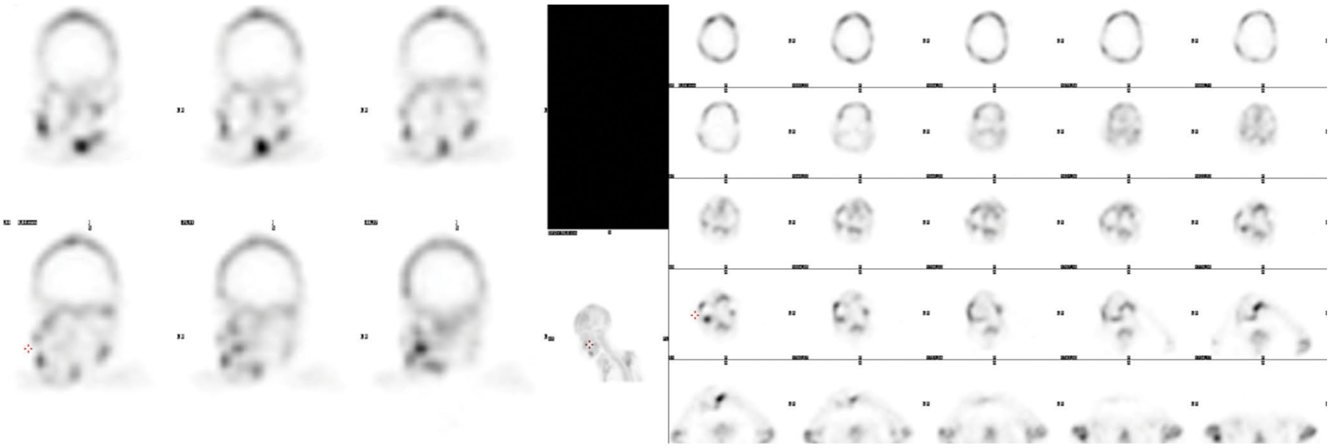

Figure 3. Single photon emission computed tomography (SPECT) image of the skull evidenced a lesion described in the right mandibular region

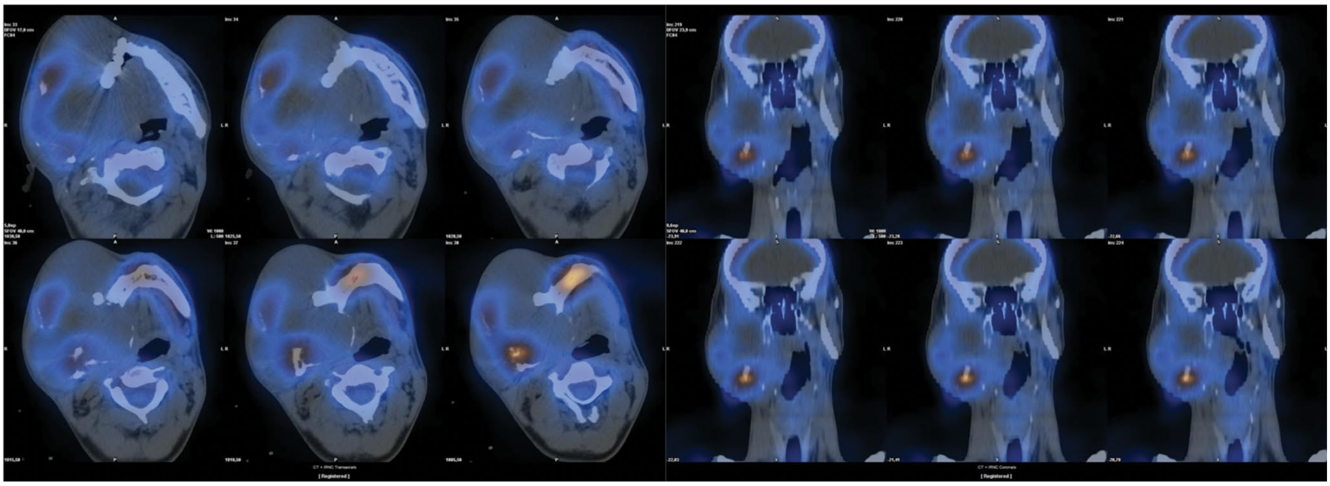

Figure 4. Single photon emission computed tomography (SPECT) image of the skull with CT fusion locating lytic lesion in the right mandible angle with extension to dental structures

VIA MEDICA

Nuclear Medicine Review 2021, 24, 1: 29–30
DOI: 10.5603/NMR.2021.0006

ISSN 1506–9680

Clinical vignette

Accumulation of ^{99m}-Tc Phytate in the pyelocalyceal system in a patient with chylous ascites — a pitfall resolved by SPECT/CT

Hadis Mohammadzadeh Kosari, Somayeh Barashki, Yasaman Fakhar, Emran Askari, Ramin Sadeghi
Nuclear Medicine Research Center, Mashhad University of Medical Sciences, Mashhad, Iran

[Received 5 VII 2020; Accepted 6 X 2020]

Abstract

We reported ^{99m}-Tc phytate accumulation in the pyelocalyceal system of the kidney in the lymphoscintigraphic images of a 3.5 months-old male infant with chylous ascites, which was mistaken with the site of lymph leakage. SPECT/CT localized activity in the para-aortic region to the renal pelvis and on delayed images, this was disappeared. Our case illustrates the added value of SPECT/CT for the differentiation of possible false-positive findings in lymphoscintigraphy.

KEY words: lymphoscintigraphy; ^{99m}-Tc phytate, chylous ascites; leakage; pyelocalyceal system; SPECT/CT

Nucl Med Rev 2021; 24, 1: 29–30

Introduction

A lymphoscintigraphy can demonstration chyloperituneum and localize the chyle leakage focus, which enables the surgeon to establish a suitable operative plan for the injured lymphatics. In all cases, it is important to recognize pitfalls to prevent misinterpretation. Herein, we representation a momentous pitfall, that has been resolved by SPECT/CT and has not been mentioned hitherto in the literature.

Case report

A 3.5 months-old male infant with a history of esophageal atresia and repaired imperforate anus, presented with slowly progressive abdominal distention. Because the ascites was chylous in nature, the patient was referred to our nuclear medicine department to identify the possible primary site of chylous leakage.

Planar and SPECT/CT images from the thoraco-abdominopelvic region were performed 20 and 120 minutes after 2mCi subcutaneous injections of ^{99m}-Tc phytate (in two divided aliquotes, 0.2 mL for each injection) in thighs. A dual-head variable angle gamma camera (GE healthcare) with LEHR (low energy high-resolution) collimator (using ^{99m}-Tc photopeak with 20% window) was used for imaging. The planar images showed a focal zone of activity on the right side of the paravertebral region (plane A in Fig. 1); which was compatible with the right pyelocalyceal system in the SPECT/CT adjacent to the 12th thoracic and 1st lumbar vertebrae (plane B in Fig. 1), while, we were wrong with the site of lymph leakage on planar images.

Delayed lymphoscintigraphic images of the thoraco-abdominopelvic region were also performed 2 hours post-injection with the same imaging protocol. The activity disappeared (Fig. 2).

Correspondence to: Ramin Sadeghi, Nuclear Medicine Research Center, School of Medicine, Mashhad University of Medical Sciences, Mashhad, Iran, e-mail: sadeghir@mums.ac.ir; raminsadeghi1355@yahoo.com

Discussion

^{99m}-Tc phytate is commonly used for liver and spleen scan and sentinel node mapping of many solid tumors [1–3]. Besides, lymphoscintigraphy with ^{99m}-Tc phytate can demonstratie chyloperituneum and can be used to evaluate the site of leakage in chylous ascites, which is very hard to localize by a conventional imaging modality like computed tomography (CT) scan [4–8]. Renal excretion of this radiotracer (most likely due to renal excretion of a ^{99m}-Tc phytate metabolite), can cause a misdiagnosis on lymphoscintigraphy images [1, 9].

Our case showed a focal area of activity on the right side of the paravertebral region that was interpreted as a possible site of chyle leakage. This focal activity was confined to the right pyelocalyceal system by SPECT/CT. Our case showed the role of SPECT/CT in resolving the diagnostic interference of normal biodistribution of the ^{99m}-Tc phytate, which can be misleading in the interpretation of the lymphoscintigraphy images.

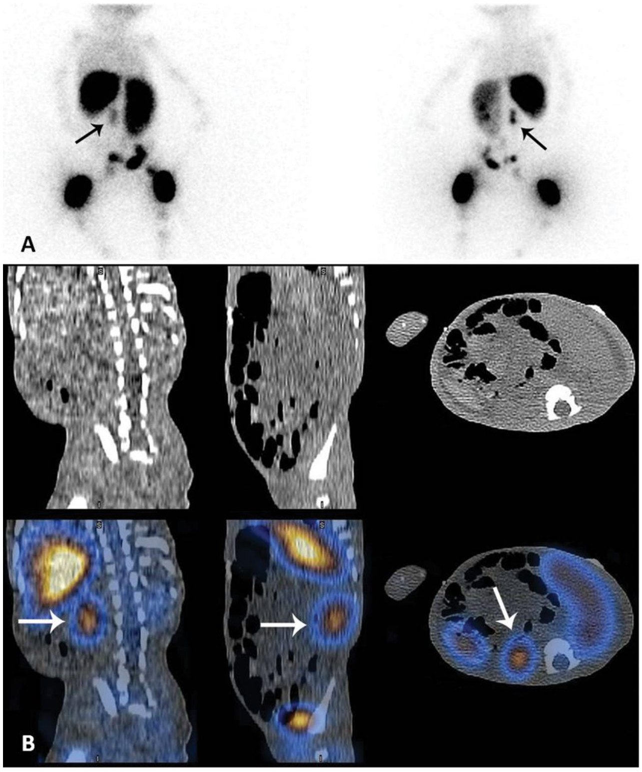

Figure 1. A. Whole-body Planar images in anterior and posterior view. The suspicious focus for the site of the leak (black arrow) was seen in the right paravertebral region. B. SPECT/CT axial, coronal, and sagittal images confirm the focal activity to the right pyelocalyceal system (white arrow)

References

1. Alivifard R, Yousefi Z, Kadkhodayan S, et al. Pelvic kidney visualization on the lymphoscintigraphy images of a patient with uterine cervix cancer: importance of the delayed imaging. Clin Nucl Med. 2014; 39(3): 286–287, doi: 10.1097/RLU.0000000000000331, indexed in Pubmed: 24368528.
2. Kao CH. Incidental detection of bilateral kidney calyces in Tc-99m phytate liver and spleen scan. Clin Nucl Med. 1999; 24(9): 720–721, doi: 10.1097/00003072-199909000-00028, indexed in Pubmed: 10478763.
3. Sadeghi R, Tabasi KT, Bazaz SMM, et al. Sentinel node mapping in the prostate cancer. Meta-analysis. Nuklearmedizin. 2011; 50(3): 107–115, doi: 10.3413/nukmed-0339-10-07, indexed in Pubmed: 21264441.
4. Gregg DC, Wells RG, Sty JR. Lymphoscintigraphy. Chylous ascites and lymphocele demonstration. Clin Nucl Med. 1988; 13(4): 300, doi: 10.1097/00003072-198804000-00019, indexed in Pubmed: 3370899.
5. Kaplan WD, Davis MA, Uren RF, et al. et al.. A model for the radionuclide measurement of ascitic fluid volumes. . J Nucl Med. 1978; 19(10): 1138–1141, indexed in Pubmed: 722324.
6. Seo Y, Shuke N, Yamamoto W, et al. Ruptured lymphocele as a cause of chylous ascites: demonstration by lymphoscintigraphy. Clin Nucl Med. 1999; 24(1): 60–61, doi: 10.1097/00003072-199901000-00014, indexed in Pubmed: 9890497.
7. Kim DW, Kim MH, Kim CG. Lymphoscintigraphy revealed chyloperitoneum after gastrectomy for gastric cancer. Clin Nucl Med. 2015; 40(1): 41–44, doi: 10.1097/RLU.0000000000000609, indexed in Pubmed: 25310405.
8. Weiss M, Schwarz F, Wallmichrath J, et al. Chylothorax and chylous ascites. Clinical utility of planar scintigraphy and tomographic imaging with SPECT/CT. Nuklearmedizin. 2015; 54(5): 231–240, doi: 10.3413/Nukmed-0723-15-02, indexed in Pubmed: 26183818.
9. Alavi A, Staum MM, Shesol BF, et al. Technetium-99m stannous phytate as an imaging agent for lymph nodes. J Nucl Med. 1978; 19(4): 422–426, indexed in Pubmed: 632933.

Figure 2. Delayed whole body Planar images in anterior and posterior view. The activity disappeared (arrow), but inguinal lymph nodes remained on both sides. Two foci of activity in the right injection site are due to patient movement during image acquisition (arrowhead)

VIA MEDICA

Nuclear Medicine Review 2021, 24, 1: 31–32
DOI: 10.5603/NMR.2021.0007
Copyright © 2021 Via Medica
ISSN 1506–9680

Clinical vignette

Fever of Unknown Origin — infected Fistula-in-Ano as the focus on ^{18}F-FDG PET-CT

Punit Sharma
Department of Nuclear Medicine and PET-CT, Apollo Gleneagles Hospitals, Kolkata, India

[Received 14 VII 2020; Accepted 22 XII 2020]

Abstract

Fever of Unknown Origin (FUO) is a vexing clinical problem. Diagnosis of aetiology is essential for definitive management. A wide array of infective, inflammatory, malignant and miscellaneous pathologies can cause FUO. Hybrid imaging with 18F-Fluorodeoxyglucose (^{18}F-FDG) positron emission tomography-computed tomography (PET-CT) is now an integral part of FUO management because of its ability to demonstrate the cause in a large proportion of cases. The authors present the case of a 42-year-old male, where an infected fistula-in-ano was detected as the cause of FUO on ^{18}F-FDG PET-CT.

KEY words: FUO; FDG; PET-CT; fistula-in-ano

Nucl Med Rev 2021; 24, 1: 31–32

A 42-year-old male presented at the hospital with complaints of multiple episodes of low to moderate grade fever for the past 6 months. The fever subsided either spontaneously or with empirical antibiotic therapy. He was hypertensive but had no other known comorbidity. The episode this time was for 7-day duration, with peak fever of 101°F. There were no localising symptoms. Clinical examination was unremarkable. Blood parameters were all normal, except for a mild neutrophilic leucocytosis (Total leucocyte count-12.000/mL; 91% Neutrophils) and raised C-reactive protein (25 mg/L). 18F-Fluorodeoxyglucose (^{18}F-FDG) positron emission tomography-computed tomography (PET-CT) (Fig. 1) was done to localise the cause of fever. Maximum intensity projection (MIP) PET images (A) showed focal increased radiotracer uptake in lower pelvis in the midline (*arrow*), apart from left renal pelviectasis (*broken arrow*). Sectional CT and PET-CT (B-G) images showed an ^{18}F-FDG avid tract (*arrow*) extending from the anal sphincter to perianal skin posteriorly in the midline in subcutaneous plane, with some fat stranding around the distal part (SUV max 9.1). Findings suggested an infected fistula-in-ano. Subsequent local examination revealed no definite cutaneous opening of fistula but a focal scar in this region and mild tenderness. On anoscopy, small internal haemorrhoids were seen. Also noted was the internal opening of the fistula. The patient was started on antibiotics and became afebrile. Magnetic resonance imaging (MRI) was performed later which confirmed infra-levator translate-sphincteric fistula and underwent surgery for the same.

Fistula-in-ano is an abnormal communication between the anal canal and the perianal skin. It originates in anal glands, which when blocked and infected form an abscess which then opens into the adjacent skin, forming a fistula. The patients usually present with discharge, pain, tenderness and at times fever. Diagnosis is made with clinical examination and anoscopy, while MRI is the best modality for mapping the fistula tract before surgery, which is the treatment of choice. ^{18}F-FDG PET-CT is now an integral part of FUO management for localising the cause. Because of the non-specific nature of ^{18}F-FDG, it is taken up by leukocytes as well as malignant cells, thereby allowing demonstration of a wide range of malignant, infective and inflammatory diseases which could present with FUO. In the present case, an infected fistula-in-ano was demonstrated as the cause of fever.

Correspondence to: Punit Sharma
Department of Nuclear Medicine and PET-CT,
Apollo Gleneagles Hospitals 58, Canal Circular Road, Kolkata-700054
e-mail: dr_punitsharma@yahoo.com

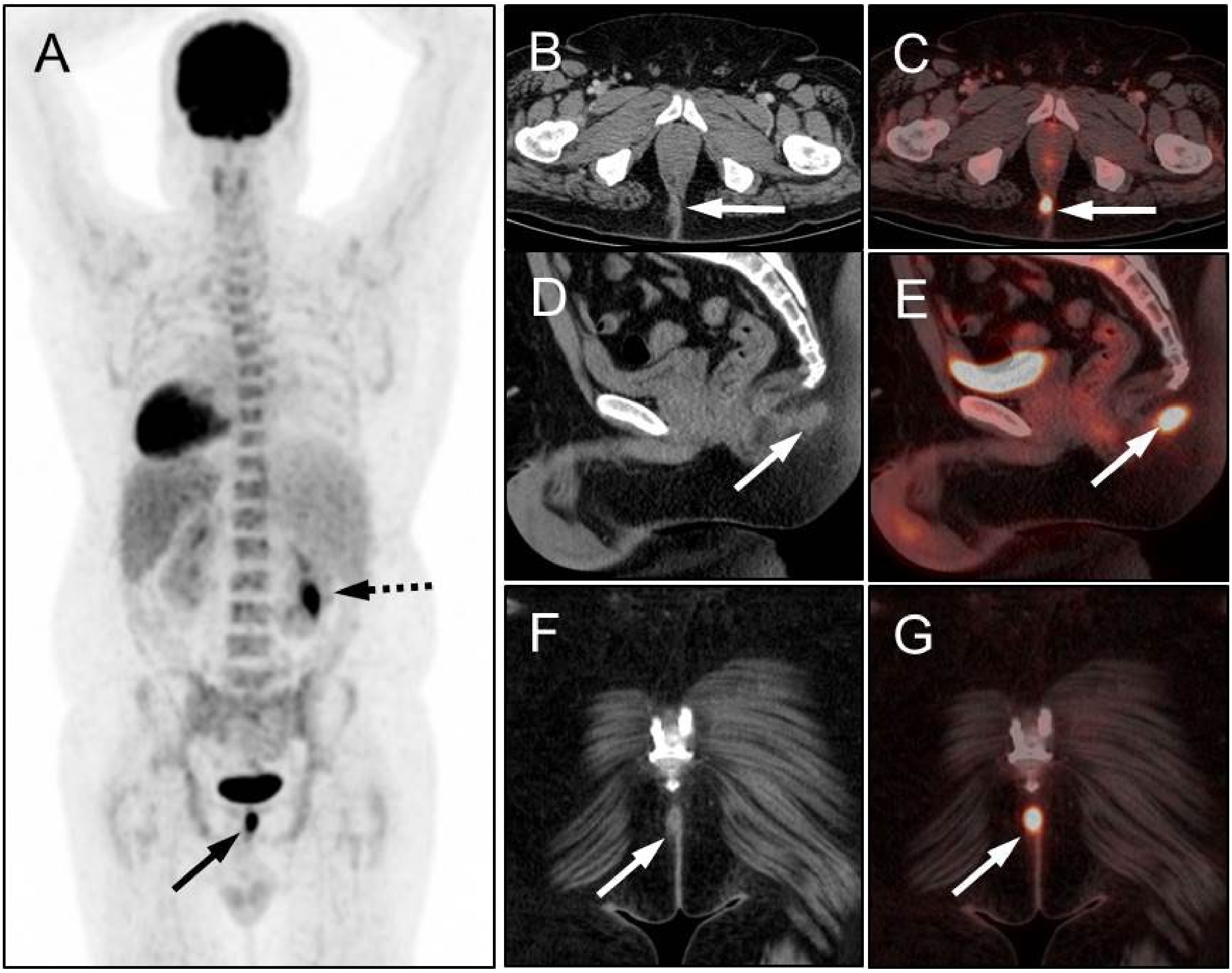

Figure 1. Images from a computer tomograph

VIA MEDICA

Nuclear Medicine Review 2021, 24, 1: 33–34
DOI: 10.5603/NMR.2021.0008

ISSN 1506–9680

Papillary thyroid carcinoma in a hyper-functional thyroid nodule

Ivan Jurić, Ana Mijatović, Damir Rozić, Joško Petričević
Sveučilišna Klinička Bolnica Mostar, Bijeli Brijeg bb, 88000 Mostar, Bosnia and Herzegovina

[Received 8 X 2020; Accepted 18 XII 2020]

Abstract

The authors reported the case of 69 years old woman presented with subclinical hyperthyroidism. ^{99m}-Tc pertechnetate scan showed the abnormal focus of hot uptake in the left lobe, suggestive of a hyperfunctioning toxic thyroid nodule. Surgical treatment was advised because of the size of the nodule as a more applicable solution. Histological findings showed papillary thyroid carcinoma.

KEY words: papillary thyroid carcinoma; hot nodule; carcinoma of the thyroid

Nucl Med Rev 2021; 24, 1: 33–34

Introduction

A toxic adenoma is a thyroid solitary node that produces and secretes increased amounts of the hormones thyroxine and triiodothyronine and causes hyperthyroidism. Clinically, the most common finding is a palpable node that appears hot on the scintigram with radioiodine or technetium pertechnetate, while the remainder of thyroid parenchyma is suppressed and faintly visible. The hot nodule is very unlikely to be malignant, and less than 1% of them are reported to harbour malignancy.

Case report

A 67-year-old women came to the clinic in 2017 and presented with heat intolerance and palpitations. She had a past medical history of arterial hypertension and atrial fibrillation. There was no previous history of neck radiation.

Physical examination revealed an enlarged left thyroid lobe with no associated lymphadenopathy. Her pulse rate was 90 BPM. She had no tremor, sweaty palms or eye signs.

Thyroid hormones were in the reference range. Thyroid ultrasonogram showed a hypoechoic, large, dominant nodule, occupying almost the entire left thyroid lobe (size 37 mm x 36 mm x 25 mm) which was sharply delineated from the rest of the parenchyma. USG also showed two 5-mm hypoechoic nodules in right thyroid lobe. There was no calcification or cervical lymphadenopathy.

^{99m}-Tc pertechnetate scan showed the abnormal focus of hot uptake in the left lobe, suggestive of a hyperfunctioning toxic thyroid nodule (Fig. 1). Considering the normal range of thyroid hormone, the follow-up hormone control in 6 months was advised. On follow-up visit she made thyroid hormones, TSH was suppressed 0.132 (normal: 0.35-4.94) while fT3 and fT4 were in the normal range.

Ultrasound showed an increase in nodal dimension and a fine needle aspiration cytology (FNAC) was made. Considering her new symptoms such as weight loss and insomnia, a therapy was introduced, thiamazole 5 mg daily.

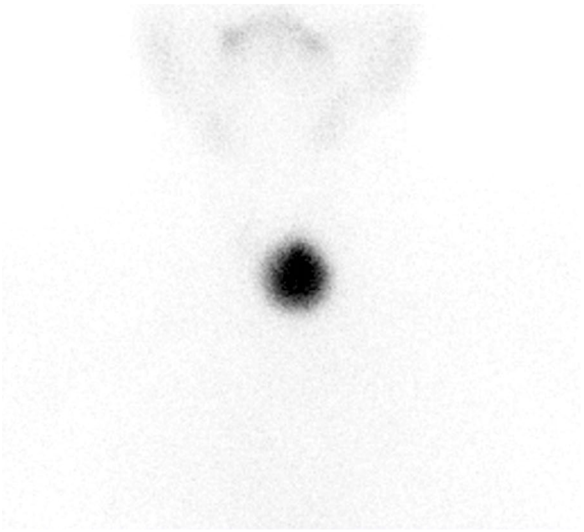

Figure 1. Abnormal focus of hot uptake in the left lobe

Correspondence to: Ivan Jurić,
Ulica Kralja Tvrtka bb, 88000 Mostar,
BiH +38736341972, vnjuric5@gmail.com

Because the node was growing and narrowing trachea, surgical treatment was advised as a more applicable solution. Subsequently, the patient brought the result of an FNAB which showed some peripheral blood and a few macro thyrocytes (Bethesda I).

With thyrostatic therapy, she became euthyroid and decided for thyroid surgery — total thyroidectomy.

A month later, she brought a histological finding. Histological examination revealed multiplicated follicles of the eosinophilic cytoplasm inside the thyroid tissue, nuclei of the appearance of ground glass with focally visible intranuclear inclusions creating an image of the papillary carcinoma-oncocytic variant. There was no clear penetration or infiltration of the surrounding parenchyma.

After seeing the histological findings, the patient prepared for therapy with 50 mCi I-131. Increased accumulation of radiopharmaceutical in the thyroid bed, suggesting thyroid remnant, was visible on the post-treatment scintigrams. No distant metastases were seen.

VIA MEDICA

Nuclear Medicine Review 2021, 24, 1: 35–36
DOI: 10.5603/NMR.2021.0009

ISSN 1506–9680

Clinical vignette

Lung perfusion SPECT/CT images associated with COVID-19 — a case series

Sara Kurkowska, Hanna Piwowarska-Bilska, Jacek Iwanowski, Bozena Birkenfeld
Department of Nuclear Medicine, Pomeranian Medical University, Szczecin, Poland

[Received 15 I 2021; Accepted 27 I 2021]

KEY words: COVID-19; SPECT/CT; lung perfusion

Nucl Med Rev 2021; 24, 1: 35–36

Coronavirus disease 2019 (COVID-19) most often presents with mild symptoms, but it can also present with viral pneumonia and acute respiratory distress syndrome, which predispose to thromboembolic disease. There is an increasing number of case studies which report the significance of ventilation/perfusion scintigraphy in the diagnosis of pulmonary embolism in COVID-19 patients [1, 2]. Since most of the patients in Poland were managed in an outpatient setting, this population has been excluded from many studies and its characteristics are not well-documented. Dhawan et al. [3] emphasize the importance of the evaluation of the prevalence and extent of perfusion abnormalities in survivors of COVID-19 through the whole spectrum of illness, from non-hospitalised patients to those in the intensive care unit (ICU).

We report a case series of three patients after recovery from COVID-19, who underwent lung perfusion SPECT/CT. Scintigraphic examinations were performed after administration of ^{99m}Tc-Makro-Albumon with an activity of about 2 MBq/kg of patient's body weight. All patients were examined using Symbia Intevo Bold with a protocol including SPECT/CT acquisition with the following parameters: LEHR collimator, 360 degrees, 120 projections, time per projection 15 sec, matrix 128x128; low-dose CT protocol. The examinations were performed to assess lung lesions in these patients. All patients were diagnosed through RT-PCR for SARS-CoV2 and were presenting mild-to-moderate symptoms. Treatment was symptomatic, including paracetamol and ibuprofen in all patients and additional azithromycin in case of Patient 1. None of them required hospitalization.

Data and perfusion SPECT/CT findings of the patients are presented in the Table 1 below. Figure 1 and 2 show SPECT/CT findings of Patients 1 and 3, respectively.

Table 1. Data, symptoms and lung perfusion SPECT/CT findings of three patients

	Age [years]	Sex	COVID-19 symptoms	Time from RT-PCR results to SPECT/CT examination	CT findings	Lung perfusion
Patient 1	65	Male	Tiredness, fever for a week with maximum 38,7°C, loss of appetite, headache, dry cough	4 weeks	Multilobar consolidative opacities with mostly subpleural distribution, reticular bronchial adhesions with traction bronchiectasis	Preserved
Patient 2	40	Male	Tiredness, fever for 5 days with maximum 38.0°C, dry cough	5 weeks	Subpleural reticulations with posterior distribution in both lungs	Preserved
Patient 3	40	Female	Tiredness, fever for 5 days with maximum 39.0°C, headache, dry cough	5 weeks	Discrete, bilateral ground-glass opacification (GGO) with a posterior distribution	Preserved

Correspondence to: Sara Kurkowska, Department of Nuclear Medicine, Pomeranian Medical University,
1 Unii Lubelskiej St, 71-344 Szczecin, Poland, e-mail: sarakurkowska95@gmail.com

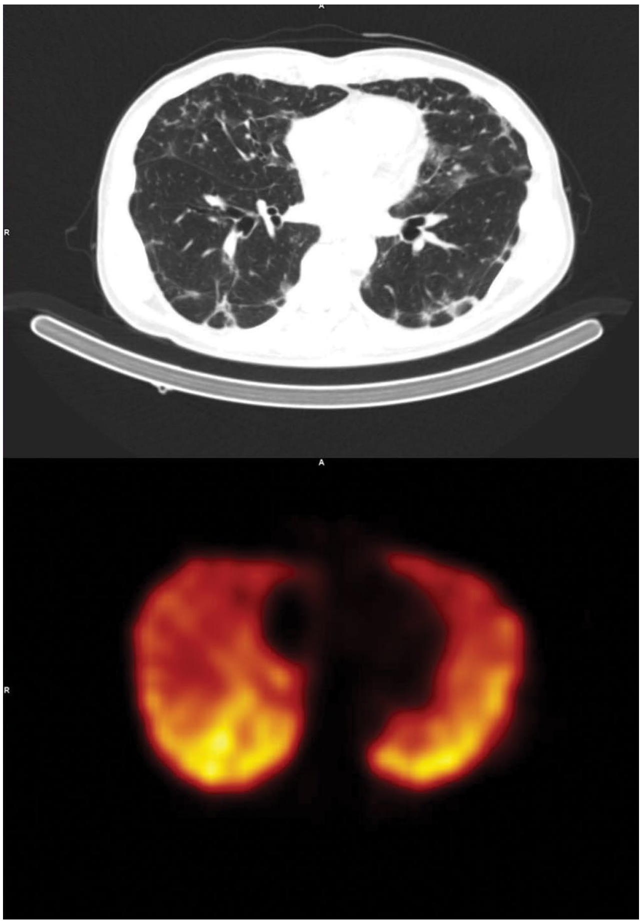

Figure 1. Lung perfusion SPECT and CT transverse slices show preserved perfusion and consolidative opacities in Patient 1

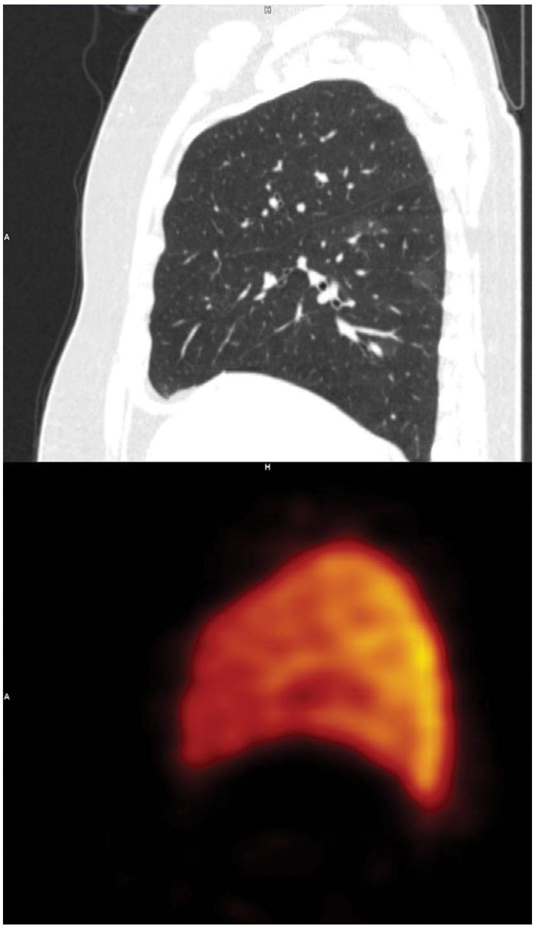

Figure 2. Lung perfusion SPECT and CT sagittal slices show preserved perfusion and GGO in Patient 3

Even though these patients present different pulmonary involvement in the unenhanced CT scans, the perfusion of all three patient was preserved, which excludes clinically significant perfusion deficit. In another series of cases, Cobes et al. [1] report that the areas affected by COVID-19 were most often responsible for ventilatory anomalies with a relatively preserved perfusion. In more serious cases of pneumonia, both perfusion and ventilation were reduced.

Reports about the prevalence of the thromboembolic disease among non-hospitalised COVID-19 patients have been published [4, 5], however, the extent to which there is a risk of hypercoagulability in the outpatient setting is still poorly-documented. Dhawan et al. [3] propose a follow-up strategy to evaluate residual clot burden, with perfusion imaging as a key triage tool, which can help to understand the different characteristics of the ventilatory and perfusion patterns related to COVID-19 pneumonia and can be important in the future to evaluate long-term outcomes of this disease.

References

1. Cobes N, Guernou M, Lussato D, et al. Ventilation/perfusion SPECT/CT findings in different lung lesions associated with COVID-19: a case series. European Journal of Nuclear Medicine and Molecular Imaging. 2020; 47(10): 2453–2460, doi: 10.1007/s00259-020-04920-w.
2. Fielding PA, Morley NCD, Bradley KM. Beware COVID-19 on VQ scans (ventilation/perfusion scintigraphy). QJM. 2020; 113(12): 892–893, doi: 10.1093/qjmed/hcaa274, indexed in Pubmed: 32976600.
3. Dhawan RT, Gopalan D, Howard L, et al. Beyond the clot: perfusion imaging of the pulmonary vasculature after COVID-19. Lancet Respir Med. 2021; 9(1): 107–116, doi: 10.1016/S2213-2600(20)30407-0, indexed in Pubmed: 33217366.
4. Gervaise A, Bouzad C, Peroux E, et al. Acute pulmonary embolism in non-hospitalized COVID-19 patients referred to CTPA by emergency department. Eur Radiol. 2020; 30(11): 6170–6177, doi: 10.1007/s00330-020-06977-5, indexed in Pubmed: 32518989.
5. Emert R, Shah P, Zampella J. COVID-19 and hypercoagulability in the outpatient setting. Thrombosis Research. 2020; 192: 122–123, doi: 10.1016/j.thromres.2020.05.031.

Nuclear Medicine Review 2021, 24, 1: 37
DOI: 10.5603/NMR.2021.0011

ISSN 1506–9680

In memoriam – Prof. Anna Celler

Dear Colleagues,

We are very sad to inform you of the recent passing on 24 December, 2020, in Vancouver, Canada of prof. Anna Celler – a friend of Polish Nuclear Medicine, and a wonderful person and beautiful woman. Anna was generous, enthusiastic about life and science, and a loving wife, mother of two children and grandmother of five grandchildren.

Anna was very much a people person and a message to colleagues from her two children Peter and Katherine (Kasia) following her passing perhaps summarises this aspect best:

“As you probably know, people were the most important thing to Anna. I almost never heard her speak about publications or experimental results, but she frequently recounted anecdotes involving her collaborators, colleagues, and students. Anyone who worked in, or closely with, the MIRG (Medical Imaging Research Group) would know about how she insisted on hosting annual Christmas parties and summer BBQs at her home, and I know she always wanted my sister and I to attend with our children as well, so that she could introduce her group to her family, and vice versa. In fact, I believe her students were her greatest source of professional pride. Their new positions, achievements, and accolades were the first thing she would point to when asked about her career”.

Anna was a professor in the Department of Radiology at the University of British Columbia (UBC) in Vancouver, Canada. She was also the founder and Head of the Medical Imaging Research Group (MIRG), associated with the Vancouver Coastal Health Research Institute, an Adjunct Professor at the Department of Mathematics, Simon Fraser University and an Associate Member at the Department of Physics and Astronomy, UBC. Her main expertise was in nuclear and medical physics, quantitative and dynamic image reconstruction and analysis, dosimetry for radionuclide therapies, cyclotron production of medical radioisotopes and use of sophisticated mathematics in different aspects of imaging. She was the author of more than 350 peer-reviewed articles, abstracts and book chapters and served on many committees and review boards. During her career, she was awarded more than 12 million dollars in research funding as principle or co-investigator. Anna served as a strong mentor for many students. She supervised or co-supervised 15 postdoctoral fellows, 16 PhD and 15 MSc students.

In 2018, Anna was recipient of the Canadian Organization of Medical Physicists (COMP) Gold Medal Award. It is the highest award given by COMP in recognition of an outstanding career and significant contributions to the field of medical physics in Canada. In particular, the Gold Medal recognizes leadership in medical physics, and is awarded for adding knowledge which alters the practice of medical physics and has an outstanding influence on the professional development and careers of medical physicists in Canada.

Anna’s academic career began in Warsaw, Poland. In 1974 she received her MSc in nuclear physics and in 1980 her PhD in nuclear physics from the University of Warsaw. She then spent several years in various research laboratories in Poland, Finland and France. In the summer of 1984, Anna, with her husband Zbigniew (also physicist) and son, immigrated to Vancouver. She start working at TRIUMF – Canada’s particle accelerator center with the Charge Exchange Group using high-energy spectroscopy to investigate spin and isospin excitations of the nucleus. In 1991 she entered the realm of medical physics and joined the nuclear medicine department at the Vancouver General Hospital. At the same time she founded the Medical Imaging Research Group (MIRG) – a team of physicists, mathematicians and computer scientists working in collaboration with medical personnel to provide scientific support for diagnostic nuclear medicine imaging and for radionuclide therapies.

Anna devoted most of her professional life to exploring diagnostics and internal radionuclide therapy from the physicist’s perspective. Curiosity and passion inseparably motivated her to deeply investigate various aspects of dosimetry. As new applications of medical isotopes appeared, Anna took up the challenge of understanding and describing the influence of the physical characteristic of the isotope decay emissions on the quality of SPECT or PET images and on therapy planning. None of the medical radionuclides, among them rhenium-188, gallium-67, indium-111,

Anna Celler and her first PhD student Glenn Wells – after the COMP Gold Medal Award ceremony on 14 September, 2018, Montreal

and, in recent years also yttrium-90 and lutetium-177, held any secrets from her. Of note is Anna's input into the development of technetium-99m production using a cyclotron. This was pioneer research initiated when shortages in nuclear reactor-produced molybdenum-99 forced scientists to search for alternative methods for obtaining technetium-99m. In a cyclotron, technetium-99m can be made by bombardment of molybdenum (enriched in molybdenum-100) with a proton beam, causing the transmutation of some of the molybdenum-100 nuclei into technetium-99m. Anna and her collaborators demonstrated that the yields of technetium-99m using this method are sufficient, so that even medical cyclotrons designed to produce PET radionuclides can produce sufficient quantities of technetium-99m to meet local needs, as she described in an interview for Physics World (https://physicsworld.com/a/cyclotrons-could-boost-technetium-supply/). This groundbreaking work paved the way to implementation of the cyclotron production method, its radiopharmaceutical validation, and, ultimately, the approval of cyclotron-produced technetium-99m for human use.

Anna's broad interests in the field of dosimetry resulted in a number of scientific papers and practical solutions for dosimetry problems. With her vast experience she became an internationally recognized expert. Within the scope of her international activity one notable contribution is MIRD Pamphlet No. 26: Joint EANM/MIRD Guidelines for Quantitative 177Lu SPECT Applied for Dosimetry of Radiopharmaceutical Therapy. This document pointed out that the accuracy of absorbed dose calculations in personalized internal radionuclide therapy is directly related to the accuracy of the activity (or activity concentration) estimates obtained at each of the imaging time points. The guidelines outline data acquisition protocols and image reconstruction techniques recommended for quantitative lutetium-177 SPECT imaging in order to reach that accuracy.

Working in close proximity and cooperation with clinical departments, she focused her efforts on making the life of nuclear medicine physicians easier. That was the stimulus and background for the development of an internal dosimetry software package which provided an assortment of tools for every step in the dose calculation process, eliminating the need for manual data transfer between various programs. The software saved time and minimized user errors, while offering a versatile method of efficiently perform patient-specific internal dose calculations in a variety of clinical situations. This software package was developed by Anna and her MIRG group at UBC, Vancouver. Not everyone knows that it

XVI Polish Society of Nuclear Medicine Symposium, Szczecin 23–26 May, 2018, Dosimetry Workshop was then licensed by UBC to the company ABX-CRO of Germany, which turned it into the commercially-offered dosimetry tool called QDOSE. Nowadays QDOSE constitutes an important support for nuclear medicine departments in their routine dosimetry assessments, for example in patients under peptide receptor radionuclide therapy.

It was Anna's dream to share her knowledge and experience with clinical teams worldwide, particularly in Poland. She gave lectures at the biannual meetings of the Polish Society of Nuclear Medicine and was involved in several projects with the Polish Nuclear Medicine departments. The last time she visited Poland was on the occasion of the Dosimetry Workshop organized during the XVI Polish Society of Nuclear Medicine Symposium in Szczecin.

During this workshop, she taught us the basics of dosimetry. In our discussions the need arose for deeper insight into the optimization of radiation doses delivered within the mixed lutetium-177 and yttrium-90 therapy of neuroendocrine tumors. Notably, for that purpose the QDOSE software package could be utilized. Both the vision and the appropriate tools for its fulfillment – that is the legacy that Anna has left for us. She would be happy to see that we make good use of it, with a sincere smile on her face – that is how we will remember her.

Bożena Birkenfeld
Renata Mikołajczak